

Study of Ethylene Glycol Dynamics Confined in Decorated SBA-15 and Novel Radicals



TECHNISCHE
UNIVERSITÄT
DARMSTADT

Vom Fachbereich Chemie

der Technischen Universität Darmstadt

zur Erlangung des akademischen Grades

Doctor rerum naturalium

(Dr. rer. nat.)

Dissertation

von

Nadia Berenice Haro Mares

Erstgutachter: Prof. Dr. Gerd Buntkowsky

Zweitgutachter: Apl. Prof. Dr. Torsten Gutmann

Darmstadt 2024

Tag der Einreichung: 15 April 2024

Tag der mündlichen Prüfung: 27 Mai 2024

Bitte zitieren Sie dieses Dokument als:

URN: [urn:nbn:de:tuda-tuprints-274748](https://nbn-resolving.org/urn:nbn:de:tuda-tuprints-274748)

URL: <http://tuprints.ulb.tu-darmstadt.de/27474>

Darmstadt, Technische Universität Darmstadt

Jahr der Veröffentlichung auf TUprints: 2024

Dieses Dokument wird bereitgestellt von tuprints,

E-Publishing-Service der TU Darmstadt

<https://tuprints.ulb.tu-darmstadt.de>

tuprints@ulb.tu-darmstadt.de

Veröffentlicht unter CC BY 4.0 International

<https://creativecommons.org/licenses/>



*“Good times become good memories,
but bad times become good lessons.”*

Iroh, Avatar

Die vorliegende Arbeit wurde am Eduard-Zintl-Institut für Anorganische und Physikalische Chemie der Technischen Universität Darmstadt unter der Leitung von Herrn Prof. Dr. Gerd Buntkowsky in der Zeit von Juni 2019 bis Mai 2024 durchgeführt.

List of Publications

Related to the results present in this thesis

- **Haro Mares, N. B.**, Döller, Sonja C., Wissel, T., Hoffmann, M. M., Vogel, M. and Buntkowsky, G. (2024). Structures and Dynamics of Complex Guest Molecules in Confinement, Revealed by Solid-State NMR, Molecular Dynamics, and Calorimetry. *Molecules* 29(7), 1669. <https://doi.org/10.3390/molecules29071669>
- **Haro Mares, N. B.**, Brodrecht, M., Wissel, T., Döller, S. C., Rösler, L., Breitzke, H., Hoffmann, M. M., Gutmann, T. and Buntkowsky, G. (2023). Influence of APTES-Decorated Mesoporous Silica on the Dynamics of Ethylene Glycol Molecules— Insights from Variable Temperature ²H Solid-State NMR. *The Journal of Physical Chemistry C*, 127 (39). <https://doi.org/10.1021/acs.jpcc.3c03671>
- Asanbaeva, N. B., Dobrynin, S. A., Morozov, D. A., **Haro-Mares, N.**, Gutmann, T., Buntkowsky, G. and Bagryanskaya, E. G. (2023). An EPR Study on Highly Stable Nitroxyl-Nitroxyl Biradicals for Dynamic Nuclear Polarization Applications at High Magnetic Fields. *Molecules*, 28(4), 1926. <https://doi.org/10.3390/molecules28041926>
- Asanbaeva, N.B., Gurskaya, L.Y., Polienko, Y.F., Rybalova, T.V., Kazantsev, M.S., Dmitriev, A.A., Gritsan, N.P., **Haro-Mares, N.**, Gutmann, T., Buntkowsky, G. and Tretyakov, E.V. (2022). Effects of Spiro-Cyclohexane Substitution of Nitroxyl Biradicals on Dynamic Nuclear Polarization. *Molecules*, 27(10), 3252. <https://doi.org/10.3390/molecules27103252>

Other collaboration during the PhD

- Buntkowsky, G., Döller, S., **Haro-Mares, N.**, Gutmann, T. and Hoffmann, M. (2022). Solid-state NMR studies of non-ionic surfactants confined in mesoporous silica. *Zeitschrift für Physikalische Chemie*, 236(6-8), 939-960. <https://doi.org/10.1515/zpch-2021-3132>
- Döller, S. C., Brodrecht, M., **Haro Mares, N. B.**, Breitzke, H., Gutmann, T., Hoffmann, M., & Buntkowsky, G. (2021). Deuterium NMR studies of the solid–liquid phase transition of octanol-d 17 confined in SBA-15. *The Journal of Physical Chemistry C*, 125(45), 25155-25164. <https://doi.org/10.1021/acs.jpcc.1c05873>
- de Oliveira, M., Herr, K., Brodrecht, M., **Haro-Mares, N. B.**, Wissel, T., Klimavicius, V., ... & Buntkowsky, G. (2021). Solvent-free dynamic nuclear polarization enhancements in organically modified mesoporous silica. *Physical Chemistry Chemical Physics*, 23(22), 12559-12568. <https://doi.org/10.1039/D1CP00985K>
- Hoffmann, M. M., Bothe, S., Brodrecht, M., Klimavicius, V., **Haro-Mares, N. B.**, Gutmann, T., & Buntkowsky, G. (2020). Direct and indirect dynamic nuclear polarization transfer observed in mesoporous materials

impregnated with nonionic surfactant solutions of polar polarizing agents. The Journal of Physical Chemistry C, 124(9), 5145-5156. <https://doi.org/10.1021/acs.jpcc.9b10504>

List of Conference Contributions

- Study of Motions in Ethylene Glycol Confinement in SBA-15 at Low Temperature via ^2H NMR. **Haro Mares, N. B.**, Brodrecht, M., Wissel, T., Döller, S. C., Rösler, L., Breitzke, H., ... & Buntkowsky, G. AMPERE NMR School, June 19th-25th, **2022**, Poland.

Determination of Motions in Ethylene Glycol Confined in Functionalized SBA-15 at low Temperature. **Haro Mares, N. B.**, Brodrecht, M., Hoffmann, M., Breitzke, H., Gutmann, T., & Buntkowsky, G. 9th IberoAmerican NMR Meeting – April 26th-29th, **2021**, Online Conference

Curriculum Vitae

Personal Details

Name	Nadia Berenice Haro Mares
Date of Birth	May 29 th , 1990
Place of Birth	Guadalajara, Mexico
Nationality	Mexican

Education

August 2008-July 2013	B.Sc. Chemical Engineering Universidad de Guadalajara, Mexico
August 2013- January 2016	M.Sc. Forest Products Universidad de Guadalajara, Mexico
Jun 2019-present	Doctoral Thesis Technical University of Darmstadt, Germany

Acknowledgments

Although this work bears my name, it is not a triumph that I achieved alone; it would not have been possible without the help and participation of several people.

First of all, I would like to thank Prof. Dr. Gerd Buntkowsky for opening the doors for me to work in his group. Thank you for always being willing to listen and resolve my concerns, for the confidence you showed in me and my work. To Prof. Dr. Markus Hoffmann for supporting my research. To Prof. Dr. Torsten Gutmann, thank you for pushing me out of my comfort zone and for reading the manuscript of my first article many times; I hope I have not caused you nightmares. I would also like to express my gratitude to Dr. Hergen Breitzke, who was always an inexhaustible source of help and willingness in the face of all the vicissitudes I faced with the equipment. Thank you for always motivating me to keep asking questions, for my training on spectrophotometers, and for always having time to answer "silly questions."

Thanks to my colleagues, especially Dr. Sonja Egert, for being a role model and for always being willing to help and share her knowledge in a fun way. She is one of the best researchers and human beings I have ever had the privilege to meet. Thanks to Monica Pinto; without her, I would not have survived the first months in Germany. Thanks for always opening a little space to teach me new things and being one of the best companions in this adventure that was the Ph.D. To my dear friend and colleague Lorenz Rösler, who always had two ears to listen to all the obstacles in my research and a privileged brain with many ideas on how to solve the different challenges that arose. To Dr. Martin Brodrecht, Dr. Laura Winands, Dr. Edina Sic, Till Wissel, and Felix Dietrich (peek-a-boo), because without them, this adventure would have been very lonely and not so much fun.

Thanks to the Deutsche Forschungsgemeinschaft for funding the project Bu-911-24-3 and to the National Science Foundation under grant no. 1953428, of which my research is a part.

So far, I have only mentioned people from this side of the ocean, but in my beloved Mexico, there were people who were a fundamental pillar. First of all, Dr. Antonio Silva, for his immense support and confidence in me and my career, which I hope to be able to reciprocate. To Dr. Ricardo Manriquez, who was the link to get the opportunity in Germany and who trained me and urged me to continue in research since I started my training as a master's student under his supervision. Thank you for never giving up on me.

Finally, but not less important, reaching the conclusion of this adventure with ups and downs would not have been possible without the most important: continuous support of my family, especially my sister, my mom and my grandpa. Also, my friends here in Germany and in Mexico, who unknowingly became my family.

Contents

Acknowledgments	viii
Contents	ix
Zusammenfassung in deutscher Sprache	xii
Abstract	xiv
1 Motivation and Scientific Questions	16
2 Introduction to Mesoporous Silica Materials and Molecules in Confinement	20
2.1 Mesoporous Silica Materials	20
2.2 Decorated Mesoporous Silica Materials.....	21
2.3 Confined Molecules in Mesoporous Materials.....	23
2.4 Ethylene Glycol	24
3 Differential Scanning Calorimetry	26
3.1 Principles of Differential Scanning Calorimetry.....	26
3.2 Heat Flux DSC.....	26
3.3 Power Compensated DSC	27
3.4 Definition of Phase Transitions -Melting and Crystallization	28
3.5 Definition of Glass Transition	29
4 Principles of Solid State Nuclear Magnetic Resonance	30
4.1 Nuclear Magnetic Resonance	30
4.2 The Zeeman Interaction	31
4.3 Chemical Shift Interaction	33
4.4 Magic Angle Spinning	34
4.5 Quadrupolar Interaction.....	35
4.6 Deuterium Solid state NMR.....	38
4.7 Spin Echo Sequence.....	40
4.8 Longitudinal and Transversal Relaxation.....	40
5 Dynamic Nuclear Polarization	43
5.1 Generalities of DNP	43
5.2 Implementation of DNP-NMR	45
5.3 Cross Polarization (CP).....	46
5.4 Solid Effect (SE)	48
5.5 Overhauser Effect (OE)	48
5.6 Cross Effect (CE).....	49
5.7 Thermal Mixing (TM)	51
5.8 Direct and Indirect Polarization.....	51

6	Experimental Methods	53
6.1	Synthesis of the confinement materials	53
6.1.1	Reagents	53
6.1.2	Synthesis of Mesoporous Silica (SBA-15).....	53
6.1.3	Synthesis of APTES Functionalized Mesoporous Silica (SBA-15 + APTES)	54
6.2	Pore characterization of the Confinement Materials by Gas Adsorption Analysis	54
6.3	Filling of the Pores of the Silica Materials	55
6.4	Sample Packing	55
6.5	Differential Scanning Calorimetry (DSC) measurements.....	55
6.6	Variable Temperature ² H solid-state NMR (² H ssNMR).....	56
6.6.1	Deuterium MAS Experiments: One Pulse Sequence	56
6.6.2	² H Static Experiments employing the Solid Echo Sequence	56
6.6.3	T ₁ and T ₂ Experiments under MAS.....	57
6.7	Radicals	57
6.7.1	Sample Preparation	57
6.7.2	Solid-state DNP Experiments	58
6.7.2.1	¹ H MAS and ¹ H MAS Saturation Recovery experiments	58
6.7.2.2	Cross Polarization	59
6.7.2.3	¹³ C MAS Direct and Indirect Polarization	59
6.7.3	Enhancement calculation (ε)	59
7	Influence of APTES Decorated SBA-15 on the Dynamics of Confined Ethylene Glycol	60
7.1	Introduction	60
7.2	Results.....	61
7.2.1	Analysis of the Phase Behavior by DSC.....	61
7.2.2	EG-d ₄ Dynamics by Variable Temperature ² H Solid-State NMR	65
7.3	Discussion	69
7.4	Conclusions and Summary.....	76
8	DNP Investigation of Novel Biradicals for Application in Polarization Transfer in Biological Systems	77
8.1	Introduction.....	77
8.2	Results.....	78
8.2.1	EPR Results	78
8.2.2	DNP Results.....	79
8.3	Discussion	81
8.3.1	Enhancements in ¹ H MAS and ¹ H→ ¹³ C CP MAS experiments.....	81
8.3.2	Direct vs. Indirect Polarization in ¹³ C MAS.....	82
8.4	Conclusions and Summary.....	86
9	Summary	87
10	Appendix	90
10.1	Adsorption-Desorption Measurements.....	90
10.2	NMR Temperature Calibration	90
10.3	Hysteresis effects in the ssNMR spectra	91
10.4	Supplementary NMR Spectroscopic Data.....	92

10.5	Supplementary EPR Data	95
10.6	Fitting Parameters for Build-up Times.....	96
10.7	TopSpin Pulse Programs	96
10.7.1	Saturation Recovery experiment (satrect1)	96
10.7.2	One Pulse experiment (onepulse)	97
10.7.3	Modified Solid Echo experiment (solidecho).....	98
10.7.4	Modified Rotor-Synchronized Solid Echo Experiment (solidecho_synch_he)	99
10.7.5	Modified Background Suppression Experiment (zgbs_torsten)	100
10.7.6	Modified Crosspolarization Experiment (cp).....	100
10.7.7	Modified ¹³ C Saturation Recovery Experiment to select Direct/Indirect Polarization Transfer Pathways (satrec_spindif_gen_torsten)	102
11	List of Symbols, Abbreviations and Units.....	103
11.1	List of Symbols and Abbreviations.....	103
11.2	List of Units	105
12	Bibliography.....	107
	Erklärungen laut Promotionsordnung.....	116

Zusammenfassung in deutscher Sprache

Die vorliegende Arbeit ist in zwei Hauptteile gegliedert:

- I. Untersuchung der Dynamik von kleinen Molekülen in „confined environment“ (mesoporöse Silicamaterialien).
- II. Bewertung der Effektivität neuartiger Radikale als Polarisationstransfer-Agentien zur Steigerung der Empfindlichkeit der Kernspinresonanz (NMR).

Im ersten Teil der Arbeit wird untersucht, wie das Vorhandensein funktioneller 3- Aminopropyltriethoxysilan (APTES)-Gruppen, die an den Porenwänden von amorphem Santa Barbara-Material (SBA- 15) angebracht sind, das Verhalten von teildeutertem Ethylenglykol (EG- d_4) als Gastmolekül in den Poren des Silicamaterials beeinflusst. Obwohl der deutliche Einfluss von funktionellen Gruppen auf das Verhalten von Molekülen, die in mesoporösen Silicaporen eingeschlossen sind, bekannt ist, sind die Details dieser Wechselwirkung an der Grenzfläche zwischen Feststoff und Flüssigkeit nicht vollständig verstanden. Die vorgestellte Arbeit umfasst die Analyse von drei verschiedenen Systemen: reines EG- d_4 , EG- d_4 eingeschlossen in unmodifiziertem SBA- 15 und EG- d_4 eingeschlossen in APTES-modifiziertem SBA- 15. Es ist wichtig zu beachten, dass beide mesoporösen Materialien ähnliche Porengrößen haben, sodass Unterschiede in der Dynamik des Gastmoleküls im Wesentlichen auf das Vorhandensein der APTES-Gruppen zurückzuführen sind.

Die Analyse der dynamischen Differenzkalorimetrie (DSC) Daten zeigt die Kristallisation von EG- d_4 innerhalb des APTES-modifizierten Materials. Der Einfluss der chemischen Umgebung auf die Kristallisation des Gastmoleküls lässt sich auf die Ausbildung von Wasserstoffbrückenbindungen zwischen verschiedenen Oberflächengruppen im Material (- OH und - NH_2) und den Hydroxylgruppen von EG- d_4 zurückzuführen. Diese bewirken eine Änderung der molekularen Ausrichtung und fördern die Kristallisation von EG- d_4 , während der gemessenen langsamen und schnellen Heiz-/Kühlzyklen im Vergleich zu EG- d_4 in unmodifiziertem SBA- 15 beziehungsweise reinem EG- d_4 .

Darüber hinaus zeigt die Analyse der 2H -Festkörper-Kernspinresonanz (2H -ssNMR)-Spektren, die bei verschiedenen Temperaturen für EG- d_4 in APTES-funktionalisiertem SBA- 15 aufgenommen wurden, dass diese Spektren im Bereich der Phasenübergangstemperaturen aus zwei unterschiedlichen Komponenten zusammengesetzt sind. Diese Komponenten bestehen aus einer Lorentz-förmigen Linie, die eine flüssigkeitsähnliche Phase repräsentiert, und einer Pake-Linie, die eine festkörperähnliche Phase repräsentiert.

Zusammenfassend führen Unterschiede in molekularen Wechselwirkungen, aufgrund unterschiedlicher Umgebungsbedingungen, zu Aktivierungsenergieverteilungen der Phasenübergänge in den drei untersuchten Systemen.

Der zweite Teil dieser Arbeit konzentriert sich darauf, die Wirksamkeit neuer Polarisationsagentien (PAs) für Dynamische Kernspinpolarisation (DNP) zu untersuchen, die für eine potenzielle Verwendung in biologischen Anwendungen entwickelt wurden. Die Stabilität einiger dieser neuen Radikale wird unter biologischen pH-Bedingungen bewertet. Dabei zeigt sich, dass sie ihre ursprüngliche Struktur beibehalten und als Polarisationsagentien unter biologischen pH-Bedingungen dienen können.

Darüber hinaus wird gefunden, dass bestimmte Substituentengruppen innerhalb der Radikalstrukturen zur Bildung von Konformeren führen. Diese Konformere wiederum reduzieren die Effizienz dieser PAs, wenn sie in DNP-Experimenten im Festkörper eingesetzt werden.

Abstract

This research project is structured into two main parts:

- i) Investigation of the dynamics of small molecules within confined pore spaces (mesoporous silica).
- ii) Evaluation of new radicals as polarization transfer agents to enhance the sensitivity of nuclear magnetic resonance (NMR).

In the first part of this study, the research focuses on understanding how the presence of 3-aminopropyl triethoxysilane (APTES) functional groups, attached to the pore walls of amorphous Santa Barbara material (SBA-15), influences the behavior of partially deuterated ethylene glycol (EG- d_4) as the guest molecule. While the significant influence of functional groups on molecules confined within mesoporous silica pores is known, the details of the interaction at the solid-liquid interface are not fully understood. This investigation involves the analysis of three distinct systems: EG- d_4 in the bulk, EG- d_4 confined within pure SBA-15, and EG- d_4 confined within APTES-modified SBA-15. Importantly, both mesoporous materials have similar pore sizes, allowing any differences in the guest molecule's dynamics to be attributed primarily to the presence of the APTES functional group.

Differential scanning calorimetry (DSC) analysis reveals the crystallization of EG- d_4 within the APTES-modified material. The influence of the surrounding on the crystallization primarily occurs due to the formation of hydrogen bonds between various surface groups in the material (-OH and -NH₂) and the hydroxyl groups of EG- d_4 . This change in the molecular alignment promotes the EG- d_4 crystallization during the recorded slow and rapid heating/cooling cycles, when compared to EG- d_4 in unmodified SBA-15 or EG- d_4 in its bulk phase.

Additionally, an analysis of the ²H solid-state Nuclear Magnetic Resonance (²H ssNMR) spectra, acquired at various temperatures for EG- d_4 confined within APTES-functionalized SBA-15, reveals two distinct components at temperatures in the region of the phase transition. These components consist of a Lorentzian-shaped line, representing a liquid-like phase, and a Pake pattern representing a solid-like phase.

In summary, variations in molecular interactions due to different environmental conditions lead to differing activation energy distributions of the phase transitions in the three systems under investigation.

The second part of this work focuses on testing the effectiveness of new polarization agents (PAs) for Dynamic Nuclear Polarization (DNP) designed for potential use in biological applications. The stability of some of these novel radicals is assessed under biological pH conditions, demonstrating that they preserve their original structure and remained capable of serving as polarization transfer agents.

Furthermore, it is determined that certain substituent groups within the radical structures led to the formation of conformers. These conformers, in turn, reduce the efficiency of these PAs when employed in solid-state DNP experiments.

1 Motivation and Scientific Questions

The increasing awareness of the need to transition to environmentally friendly processes, coupled with advances in science and technology, has resulted in the use of materials and processes at progressively smaller scales.^[1,2] Materials often used for this purpose are mesoporous silica materials.^[3] These materials have pore sizes ranging from 2 to 50 nm and exhibit favorable physical properties such as high thermal stability, a large surface area, non-toxicity, and wide accessibility. As a result, they have diverse applications in fields such as optics, catalysis, pharmaceuticals, bioengineering, energy storage, and more.^[4-9] Many of these applications entail the utilization of solvents or liquid media within the pores of these materials. It is well-established that when liquids are confined within spaces roughly equivalent to the size of their molecules,^[10,11] they undergo changes in their physicochemical properties. These alterations result from interactions between the liquid phases and the surface of the enclosing material, which, in turn, depend on the size and structure of the pore walls. These interactions significantly impact the dynamics of the confined molecules and lead to variations in first-order transitions, such as melting and freezing, which are particularly sensitive to interactions between liquids and solids.^[11-14]

The significance of this lies in the frequent modification of the walls of these materials to imbue them with properties tailored to their intended applications. This modification involves introducing functional groups that affect the movements of guest molecules within the pores.^[15-17] Besides interacting with the silanol groups (Si-OH) of the pore walls, these guest molecules also engage with the newly introduced functional groups.

The first part of the work focuses on studying the dynamics of molecules in confinement and how functional groups in the pore walls affect the dynamics of the host molecule. To study the effect of pore wall functional groups on the dynamics of molecules in confinement, Ethylene Glycol (EG) was chosen as a guest molecule, and analyzed under three different environmental conditions: (i) in the bulk, and as a guest molecule inside (ii) the pores of a Santa Barbara amorphous material (SBA- 15) and in the pores of SBA- 15 modified with 3- aminopropyl triethoxysilane (APTES)

A material modified with APTES has been selected for this study as APTES is widely used in the modification of mesoporous materials.^[18-20] Additionally, the choice of EG as the guest molecule considers its versatile application as a “green” solvent, and its ability to form hydrogen bonds at both ends of the molecule.^[21-24]

To investigate the impact of APTES on the dynamics of EG, the study utilized Differential Scanning Calorimetry (DSC) and variable temperature ²H solid-state Nuclear Magnetic Resonance (ssNMR). DSC is a thermal analysis technique measuring the heat required to change a sample's temperature, enabling the detection of endothermic and exothermic phase transitions in both solid and liquid samples.^[25-28] Solid-state nuclear

magnetic resonance spectroscopy is highly useful for identifying and characterizing local structural features, including the characteristics of neighboring atoms, bond lengths, bond angles, and the symmetry of atomic environments. Consequently, it provides valuable insights into how substituents impact their immediate surroundings.^[29–32]

Local structural information is encoded in interactions between NMR-active nuclei and their surroundings, especially in the case of nuclei with $I > \frac{1}{2}$ (quadrupolar nuclei). This study primarily focuses on evaluating the chemical shift and the quadrupolar interaction of deuterium ($I=1$). The former depends on the shielding of probed nuclei from the magnetic field of the spectrometer by the electron density in their vicinity, while the latter arises from the interaction of a non-spherical nuclear charge distribution with the electric field gradient at the nucleus site, created by neighbouring electric charges.

In resulting NMR spectra, the effects of these interactions accumulate. In the presence of multiple interactions and corresponding parameter variations, signals can become broad and featureless. These resulting line shapes are then simulated to quantify the underlying NMR parameter distributions. All the experiments were conducted at variable low temperatures in three different systems.

In addition to the dynamics study mentioned above, the second part of this work aims to explore the utilization of a new set of radicals as potential polarization transfer agents (PAs) for solid-state NMR experiments enhanced with Dynamic Nuclear Polarization (DNP).

As it was mentioned before, solid state NMR is a powerful tool, mainly used to elucidate atomic structures, but is limited by its low sensitivity. To address this limitation, various strategies can be employed, including utilizing high-field spectrometers, increasing the concentration of relevant nuclei in the sample, conducting experiments at lower temperatures (cryogenic conditions), employing specialized pulse sequences, and exploring hyperpolarization techniques.^[33–35]

One Hyperpolarization technique to enhance the ssNMR signals is Dynamic Nuclear Polarization.^[33] This technique consists in transfer the polarization of an unpaired electron (e^-) in the PA to the nuclei of interest (I) via microwave irradiation (μW). The interplay of hyperfine interactions, including isotropic and anisotropic components, affects the energy level structure and dynamics of the system.

Polarization agents can be stable unpaired electrons in metal ions (with unoccupied d - or f -orbitals)^[36–39] or radicals in tailored molecules designed for this specific purpose like nitroxide base radicals^[40–43]. Since most samples lack inherent sources of unpaired electrons, PAs are often added to the sample, usually in a solvent mixture that forms a glass when frozen.^[44,45] It is essential for the radical solution to freeze uniformly as a

glass to prevent the formation of ice crystals, ensuring an even distribution of polarizing agents and preventing their aggregation. A homogeneous glassy DNP sample maximizes boost efficiency.^[34,45]

However, when dealing with these compounds, scientists encounter challenges related to their limited solubility in water and their resistance to reductants, which is crucial in biological sample preparation.^[46] Even the reduction of a fraction of a biradical by a cell culture medium can render the PA inactive, resulting in the failure of a DNP experiment.

Improvements in solubility and relaxation times have been achieved by adjusting the molecular structure of nitroxide biradicals, showcasing promising results in biological systems.^[47–55] These enhancements have been addressed by fine-tuning the length and rigidity of the linker between the radical centers. The electron-electron (e^-e^-) coupling is influenced by both the exchange interaction and the dipolar coupling. The exchange interaction arises from the overlap of spin-bearing molecular orbitals and becomes noticeable only when the radical centers are separated by a limited number of chemical bonds, demonstrating favorable molecular geometries. Conversely, dipolar coupling is a through-space interaction, contingent on the distance between paramagnetic centers and the orientation of their connecting vector relative to the external magnetic field (B_0).^[48,51]

As the structure of the radicals is relevant for its performance during the DNP experiments, it is necessary to continue researching and developing molecules with better characteristics as PAs. In this work, the investigated molecules used spirocyclohexane or tetraethyl groups as substituents in bi-nitroxide radicals. It has been shown that this kind of structures provides additional stability to the molecule in its use as a PA for biological applications.^[42,44,56]

The efficiency of the novel polarization agents for DNP was assessed by comparing ssNMR experiments conducted with and without microwave irradiation. Additional experiments were conducted to study the polarization transfer mechanism.

In summary, this work addresses the following scientific questions:

- *Are the dynamics of EG-d₄ confined inside SBA-15 modified with APTES different from those of EG-d₄ confined in pure SBA-15, and in the bulk?*
- *What insights can be gleaned about the dynamics of EG-d₄ in various environments from deuterium ssNMR parameters?*
- *How are the dynamics of EG-d₄ evolving in different environments as a function of temperature?*

-
- *Can the new radicals be used as polarization agents?*
 - *Which polarization transfer mechanism is more favorable for the radicals (direct or indirect) in ^{13}C MAS experiments?*

In the following Chapter 2, we provide an overview of mesoporous silica materials and molecules in confinement. In Chapters 3 to 5, we describe the basic principles of DSC, Solid-state NMR spectroscopy, and DNP as the techniques applied in this study. Experimental procedures are detailed in Chapter 6. Chapter 7 presents the results and discussion of the study on dynamics of ethylene glycol confined in decorated SBA-15 at low temperatures. Meanwhile, Chapter 8 is dedicated to presenting the results and their respective discussions on the DNP study of novel radicals for applications in biocompatible environment. The primary findings are summarized in Chapter 9.

2 Introduction to Mesoporous Silica Materials and Molecules in Confinement

Due to the wide use of mesoporous silica materials and their versatile applications, numerous methodologies have been developed for their synthesis, depending on the desired characteristics of the final product. In some cases, functional groups are incorporated onto the pore walls of these materials. It is well-established that any modification of pore wall or pore diameter has an impact on molecules confined within the pores, especially in liquid phase

The purpose of this chapter is to provide a brief overview of mesopore materials, the modification of their pore walls, as well as to provide introductory information on the effects on molecules confined in them. To acquaint the reader with the research results presented in Chapter 7, information on APTES-decorated silica material and ethylene glycol are also included

2.1 Mesoporous Silica Materials

Porous materials, as implied by their name, belong to a class of materials characterized by the presence of pores (cavities, channels, or interstices). The physicochemical attributes of these materials are intricately linked to factors such as size, arrangement, and configuration of the pores, along with the material's porosity (the ratio of the total pore volume to the apparent volume of the material) and its composition. The structural component of the material is referred to as the 'matrix' or 'frame.' This matrix can be organic (including fibers, biopolymers, carbon etc.), hybrid (comprising metal-organic frameworks (MOFs), biogenic materials like nacre, phenyltrialkoxysilanes), or inorganic (encompassing silicates, metal oxides, minerals, clays).^[57-60] For the scope of this study, our focus will be on materials featuring a matrix composed of ordered mesoporous silica.

Mesoporous silica materials are characterized by their solid structures containing pores with sizes ranging between 2 and 50 nm.^[4,61] The pores are cavities or channels with tunable sizes and defined geometries, as illustrated in Figure 2.1, that contribute to the material's large specific surface area.^[5,62,63] The characteristic properties of these materials, including high thermal stability, large surface area, non-toxicity, and widespread availability, make them suitable for various applications. They find use in ion exchange, molecular sieves, adsorption media, optics, catalysis, bioengineering, energy storage, and drug delivery systems.^[4-9,64]

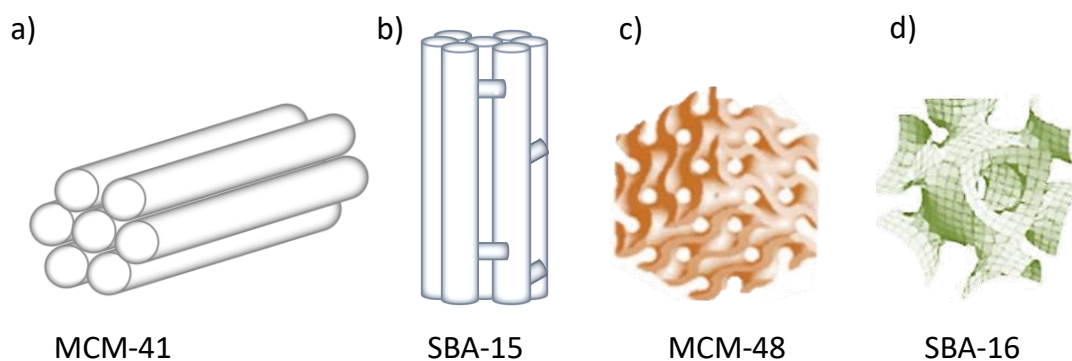


Figure 2.1. Common structures found in mesoporous materials: a) and b) hexagonal structure (space group $p6mm$) c) body-centered cubic structure (space group $Im3d$), (d) body-centered cubic structure (space group $Im3m$). Figure adapted from reference.^[65]

Since its first report in 1990 by Kuroda and co-workers,^[66] outlining the synthesis of a silica-based material with a uniform pore size and geometry named FSM-16 (Folded Sheet Material), several methodologies for the production of well-defined silica materials have been documented. Two of the methodologies developed in the 1990s gave rise to two extensively studied families of mesoporous materials: Mobil Composition of Matter (MCM) and Santa Barbara Amorphous (SBA) materials. MCM was introduced by scientists at Mobil Oil Company in 1994,^[67] while SBA was disclosed four years later in 1998 by Zhao Dongyuan et al.^[68,69] The methodologies employed for synthesizing both materials are based on utilizing self-organized surfactants as scaffolds to create channels within the materials. Once the pore walls are established, the surfactants can be eliminated through calcination or extraction.

These materials consist of a series of hexagonally arranged parallel cylindrical channels (see Figure 2.1a), with mesopores or pores also arranged in a random order. The primary distinction between the two materials is that MCM-41 has a smaller pore size compared to SBA-15, the latter additionally featuring micropores that interconnect its primary mesopores. Another notable difference is that the pore wall in Santa Barbara materials is thicker (3-6 nm), rendering it more thermally stable than MCM-41.^[69,70]

2.2 Decorated Mesoporous Silica Materials.

Several specifics of the above-mentioned applications of mesoporous silica materials, such as heterogeneous catalysis, drug delivery, and ion conduction, necessitate the presence of organic molecules within the pore of the mesoporous materials. In many instances, these organic molecules are covalently attached to the silanol groups on the silica pore walls.^[15-17] This functionalization alters the surface hydrophilicity and, consequently, the chemical interactions with molecules inside the pores.^[71-76] The motions of guest molecules near the pore walls are influenced by the geometry and chemical nature of the walls. These perturbations manifest as changes in the mobility of the guest molecules,^[77] which subsequently impact thermodynamic processes such as melting, freezing, adsorption, or desorption.^[78]

In general, for materials synthesized from self-organized molecules, there are two approaches to incorporate these molecules into the silica matrix, schematically illustrated in Figure 2.2, grafting and co-condensation.^[79] Grafting involves attaching new molecules to the silanol (Si-OH) groups exposed within the material's pores through covalent bonding after the matrix has been synthesized (post-synthesis). The second method (co-condensation) takes place during the synthesis of the matrix, specifically during the sol-gel process. Functional groups become bound to the tetraalkoxysilanes (like grafting), while condensation concurrently occurs. The advantage of the second method lies in the more uniform distribution of functional groups throughout the inner surface of the pore, compared to the first approach where functionalization is concentrated at the pore entrance and outer surface.^[74]

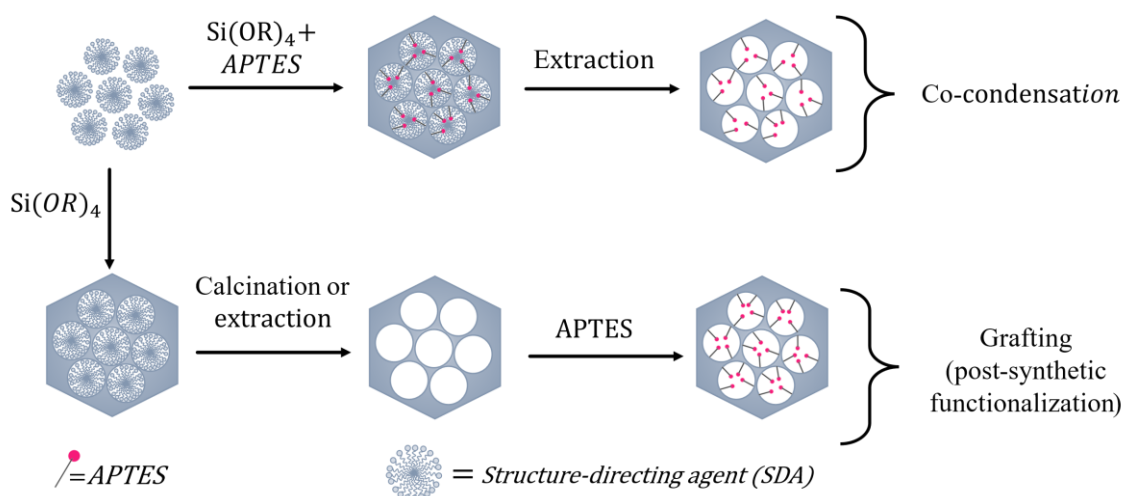


Figure 2.2. Schematic diagram of the two approaches used to functionalize silica materials: co-condensation and grafting. Depiction based on Brühwiler.^[80]

3-Aminopropyl triethoxysilane (APTES) (Figure 2.3a) stands out as one of the most extensively used functionalization agent for modifying silica surfaces. The presence of the terminal amino group ($-\text{NH}_2$) enables the attachment or 'linking' of molecules of interest, such as drugs, biomolecules (enzymes, DNA, proteins, etc.), and homogeneous transition metal catalysts. These moieties, which would normally exhibit little or no affinity for silica materials, can be effectively attached due to the presence of the amino group.^[18–20]

Studies have demonstrated that grafting APTES onto Santa Barbara Amorphous materials induces changes in the electrostatic equilibrium and hydrophilicity of the matrix. This is attributed to interactions, including hydrogen bonding and hydrophobicity resulting from the aliphatic chain.^[81–83] The impact of APTES's polarity and hydrophobicity was quantified by Wang and colleagues^[84] through contact angle measurements between unmodified and APTES-modified borosilicate glass surfaces and a water droplet. The measurements showed that while water forms an angle of approximately 5.4° on unmodified glass, it forms an angle of $\approx 55.8^\circ$ on the APTES-modified surface, indicating a rise in hydrophobicity due to the modification. A similar behavior was reported by Kowalczyk et al.^[85], who modified the surface of quartz with APTES. They observed the contact angle

of the unmodified quartz, which was 43 ± 3 , change to 52 ± 1 to 56 ± 3 according to the amount of APTES on their surface. Therefore, a modification on the contact angle of the pristine SBA-15 ($\theta\approx 18.9$) to higher values is expected.^[86]

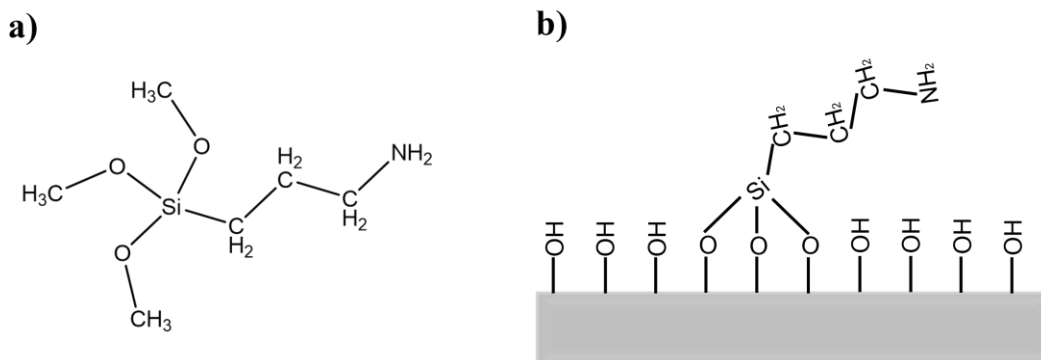


Figure 2.3. a) chemical structure of the 3-aminopropyl triethoxysilane (APTES), b) APTES attached to silica surface.

Aside from pore wall functionalization, it is imperative to highlight that these materials elicit a unique behavior of molecules by the confinement in pores in contrast to their behavior in bulk environment.

The pore diameter of these materials introduces capillary forces that give rise to confinement effects on molecules within them. This phenomenon leads to a range of changes in structural and physical properties, including shifts in melting points when compared to the bulk phase. The impact of these confinement effects has been extensively investigated for substances like water and small organic molecules within porous silica in the past.^[87–91]

2.3 Confined Molecules in Mesoporous Materials

Confined molecules within constrained geometries hold significant importance across a broad range of applications. The confinement material can take on one-dimensional (pore), two-dimensional (slit), or three-dimensional (cavity) forms.^[92,93]

Certain thermodynamic properties of molecules in confinement deviate from bulk behavior due to strong solid-liquid interactions. Within a confinement, molecules in the liquid phase in proximity to the confinement material adopt a configuration influenced by the chemical composition of the pore walls (intermolecular forces) and the spacing of the confinement material. As the pore size approaches the size of the confined molecule, discrepancies in physicochemical properties between the bulk phase and molecules in constrained geometries become more pronounced.^[10,11] Accordingly, the size, shape, and topology of the confined material significantly influence the dynamics of the guest molecule.^[12] First-order phase transitions, like melting or freezing, are particularly sensitive to solid-liquid interactions. These surface forces also induce novel phase changes in confined molecules.^[11–14]

Despite the considerable interest and significance of this subject, and the extensive body of research dedicated to it, a complete understanding of the thermal, structural, and dynamical properties of confined molecules is still lacking. Here, solid-state NMR can provide distinctive insights into the dynamics of confined molecules. By employing deuterated compounds as guest molecules within the materials, it becomes feasible to track the rotational dynamics of the compound within constrained geometries.^[94,95] In this study, partially deuterated ethylene glycol was chosen as the guest molecule.

2.4 Ethylene Glycol

Ethylene glycol (EG), an organic compound, with formula $(\text{CH}_2\text{OH})_2$ and structure shown in Figure 2.4, was first synthesized in 1859 by the French chemist Charles Adolphe Wurtz by saponification of glycol diacetate with potassium hydroxide. Nowadays, ethylene glycol is produced from a range of feedstock materials and processes, including naphtha, coal-based methanol, natural gas, and biomass, among others.^[21,96] As for its applications, EG and its derivatives find widespread use in the production of various goods such as textiles, packaging materials, fuel cells, solvents, heat transfer fluids, polyester, pharmaceuticals, and more.^[21,97,98] In the realm of biotechnology, it serves as a cryoprotective agent (CPA) and contributes to glass formation in vitrification solutions.^[99] Thus, the production all around the world is projected to reach 71.83 million tons by 2025.^[100]

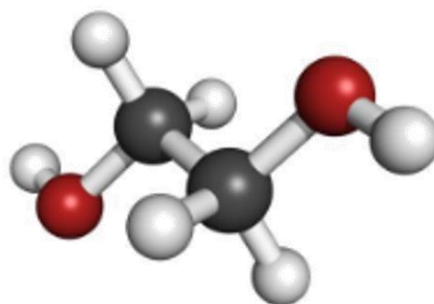


Figure 2.4 Structure of Ethylene Glycol.

The substantial demand for this compound, also arising from the growing interest and the necessity to adopt environmentally sustainable materials and processes, renders this molecule an intriguing subject of study. Its low toxicity, non-volatility, high abundance, and availability from biomass grant it the significant advantage of being considered as "green" solvent.^[21–24] Several physical properties of ethylene glycol relevant to this study are presented in Table 2.1.

Table 2.1. Physical properties of ethylene glycol.^[21,101]

Boiling point at 101.3 kPa	197.6 °C
Density at 20 °C	1113.5x10 ⁻⁹ g m ⁻³
Molecular weight	62.1 g mol ⁻¹
Normal freezing point	-130 °C
Melting point	-11.5 °C
Solubility in water at 20 °C	100 wt%
Surface tension at 25 °C	48.0x10 ⁻³ N m ⁻¹
Vapor pressure at 20 °C	7.5 Pa
Viscosity at 20 °C	19.8x10 ⁻³ Pa s

From a structural perspective, ethylene glycol is a molecule capable of executing large-amplitude motions. It possesses three sites that enable rotational movements: around the C-C bond and the two C-O bonds.^[102] These rotational degrees of freedom enable the molecules to crystallize under maximization of hydrogen bonds. According to the results obtained by Fortes & Suard,^[103] monoclinic unit cell of ethylene glycol (EG) of fully deuterated EG has the follow dimensions: $a = 5.0553 \text{ \AA}$, $b = 6.9627 \text{ \AA}$, $c = 9.2709 \text{ \AA}$ resulting in a Volume of $V = 326.319 \text{ \AA}^3$.

To comprehensively explore the influence of confinement effects and assess the impact of APTES modification of the pore surface on the dynamics of ethylene glycol, a synergistic approach employing differential scanning calorimetry (DSC) and variable temperature ²H solid-state NMR (²H ssNMR) can be used. DSC provided insights into physical processes like melting, crystallization, or glass transitions of ethylene glycol in a confined environment.^[25–28] On the other hand, solid-state NMR furnishes valuable thermodynamic and kinetic data.^[29]

3 Differential Scanning Calorimetry

This section introduces the fundamentals of differential scanning calorimetry, and is built upon the works of Pooria,^[25] Clas,^[26] and other works explicitly referenced in the main body of the text.

Differential scanning calorimetry (DSC) is a thermo-analytical technique that relies on measuring the difference in heat needed to increase the temperature of a sample in comparison to a reference, as a function of temperature. This technique is capable of identifying endothermic and exothermic transitions in both solid and liquid samples.

This chapter commences with a comprehensive overview of the principles governing DSC. It subsequently delves into the two primary types of DSC techniques, namely heat flux and power compensation. The chapter concludes by exploring the diverse range of phase transitions that can be studied using this technique.

3.1 Principles of Differential Scanning Calorimetry

DSC is a versatile technique employed for the characterization of various properties, including glass transitions, thermodynamic behaviors, and kinetics of a broad range of substances, even when only small sample amounts (typically in the milligram range) are available.^[104] The DSC setup consists of a measuring cell and a computer. Within the measuring cell, two crucibles are positioned. By applying a heat flow, the temperature of these crucibles can either increase or decrease. One of these crucibles contains the sample, while the other remains empty and serves as a reference. Throughout the experiment, the instrument is designed to ensure that both the sample and the reference experience temperature changes at the exact same rate ($\Delta T/\Delta t$), as predetermined by the user. This heating or cooling rate remains constant at every point during the experiment.

To maintain uniform and constant temperature changes for both crucibles, the apparatus must deliver a different heat flow to the crucible containing the sample, accounting for differences in heat capacity and physical changes occurring within the sample.^[61]

The two types of DSC instruments widely used are based on the source of the heat flow: heat flux and power compensation DSC.

3.2 Heat Flux DSC

In this system, both the sample and the reference receive their heat flow from the same heating source (thermoelectric disc), as illustrated in Figure 3.1. The difference in the heat flow (measured in J/s) between the

sample and the reference is recorded. This difference is then correlated to the enthalpy change within the sample by calibration experiments.^[28]

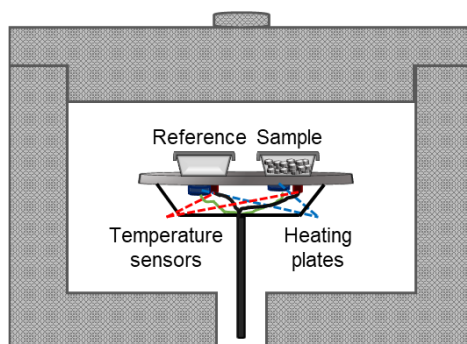


Figure 3.1 Schematic diagram of a heat flux DSC system. The sample and the reference are heated with the same heating source.

3.3 Power Compensated DSC

In this DSC arrangement, the sample and the reference are heated independently. Thermocouples, employed for temperature monitoring, are fixed to the sample holder, as depicted in Figure 3.2. Using an equivalent of the Ohm's Law (Eq 3.1) one can calculate the heat flow rate, enabling subsequent determination of enthalpy, much like the process undertaken in Heat Flux DSC.

$$\frac{dq}{dt} = \frac{\Delta T}{R_D} \quad (3.1)$$

where $\frac{dq}{dt}$ is the change on the heat with the time (heat flow), ΔT is the temperature difference between the sample and the reference and R_D is the thermal resistance of the disk platform.

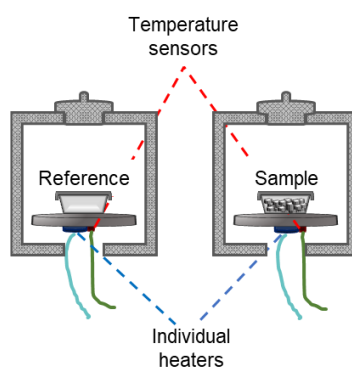


Figure 3.2 Schematic diagram of the power compensated DSC system. The sample and the reference are heated separately.

Regardless of the specific type of DSC instrument employed for the experiments, all parameters involved in the measurements, including the initial temperature and heating rate for both the sample and the reference, are meticulously monitored, recorded, and subsequently subjected to analysis.

Through the analysis of DSC curves, valuable information can be extracted, such as enthalpies of transitions, oxidative stability, freezing and melting temperatures.

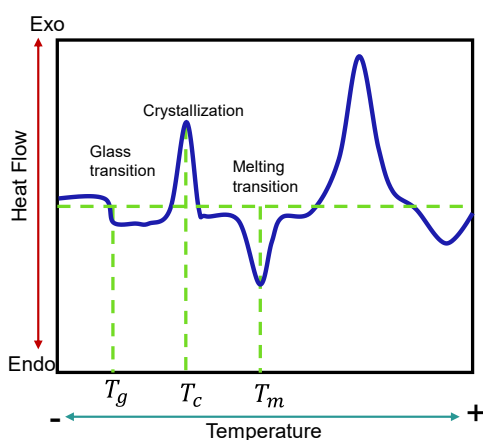


Figure 3.3 Schematic diagram of a DSC curve, based on reference. [105]

3.4 Definition of Phase Transitions -Melting and Crystallization

The term phase transition pertains to the physical process wherein a thermodynamic system undergoes a transition between two states of matter aggregation, characterized by distinct physical properties. For instance, the transition from a solid to a liquid phase is an endothermic phenomenon, as depicted in Figure 3.4b. During this process, energy, supplied in the form of heat, is absorbed by the molecules comprising the solid material. As these molecules accumulate sufficient energy, the vibrational high modes of the molecules are excited as well as rotational and translational modes, necessitating greater intermolecular spacing. Consequently, the once rigid solid structure begins to lose its rigidity.

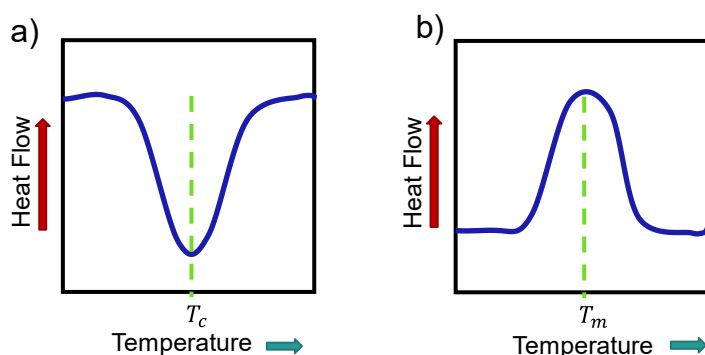


Figure 3.4: Schematic DSC diagram of a solid-liquid (melting) phase transition. Adapted from reference. [106]

Despite the continuous influx of heat, the temperature of the solid material does not rise until the phase transition is complete. The energy required for this transition is known as latent heat. Should thermal energy be insufficient to overcome the intermolecular forces that hold the molecules together, they remain trapped in a bound state, engaged in random, restricted movements. Typically, when latent heat is involved, the process

follows a first-order transition. Second-order transitions, on the other hand, do not entail latent heat, but their occurrence can be identified by abrupt changes in other parameters such as compressibility, heat capacity (C_p), thermal expansion coefficients, and more.

When it comes to the crystallization, during this first-order exothermic process, molecules possess sufficient energy to arrange themselves in ordered structures. The temperature at the lowest point of the exothermic peak is commonly regarded as the crystallization temperature (T_c), as is show in figure 3.4a.

3.5 Definition of Glass Transition

A glass transition characterizes a transformation within a system, wherein it shifts from a state of equilibrium fluidity to a non-equilibrium disordered solid state. In this state, the molecules retain the same level of disorder as in a liquid, albeit their dynamics slow down. In accordance with thermodynamics, this phenomenon isn't deemed a transition but rather a kinetic process. In an amorphous solid, the molecules lack adequate time to relax within the time frame of the experiment.^[107] This phenomenon is exclusive to glassy materials. The heat capacity and viscosity experience a sudden increase, and latent heat is absent as seen in Figure 3.5, hence adhering to a second-order transition.^[108]

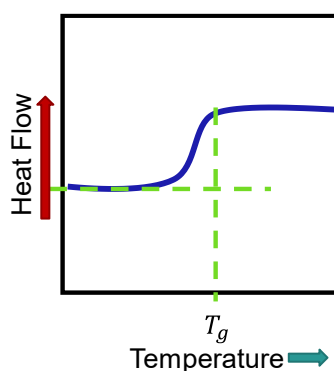


Figure 3.5: Schematic DSC diagram of a glass transition. Adapted from reference.^[106]

4 Principles of Solid State Nuclear Magnetic Resonance

The content of this chapter is built upon the works of Keeler,^[109] Levitt,^[110] Slichter,^[111] and Fyfe,^[112] as well as other sources explicitly referenced in the text.

Solid-state nuclear magnetic resonance (NMR) spectroscopy is a versatile technique primarily employed to unveil the three-dimensional structure of solid or semi-solid materials and dynamic processes within these materials. Its exceptional sensitivity to the local environment of observed nuclei empowers this technique to provide insights into molecular structure and conformational dynamics. Changes in molecular orientation affect parameters like chemical shielding, dipole-dipole coupling, or, in the case of nuclei with $I > \frac{1}{2}$, variations in quadrupolar parameters.^[113]

Deuterium, an NMR-active quadrupolar nucleus with a spin $I=1$, and a relatively small quadrupolar moment ($Q = 2.875 \times 10^{-31} \text{ m}^2$),^[114] has found widespread application in studying dynamics across diverse regimes. Through line shape analysis, ^2H spectra offer valuable insights into the system under study.

This chapter gives a comprehensive overview of solid-state NMR fundamentals, covering aspects such as Zeeman and chemical shift interactions. Subsequently, it delves into magic angle spinning and the quadrupolar interaction, concluding with information about deuterium solid-state NMR spectroscopy and common pulse sequences used for these nuclei, including spin echo and single pulse sequences.

4.1 Nuclear Magnetic Resonance

Atomic and subatomic particles possess a fundamental property known as spin angular momentum or nuclear spin. Protons, neutrons, and electrons all exhibit spin. For the entire atomic nucleus, this property is quantified by the quantum number I . The magnitude of I can only have discrete integer or half-integer values ($0, \frac{1}{2}, 1, \frac{3}{2}, \dots, \frac{9}{2}$), based on the ground state of the total angular momentum specific to each nucleus in the periodic table. To be NMR active, a nucleus must possess a non-zero value of I .

Associated with each nuclear spin is a nuclear magnetic moment ($\vec{\mu}$), which interacts with its surroundings. Nuclear magnetic resonance spectroscopy is founded on the interaction between the magnetic moment with an external static magnetic field (\vec{B}_0) the Zeeman interaction (\hat{H}_z). Next to the interaction with \vec{B}_0 , the spin can experience several interactions, including the chemical shift interaction (\hat{H}_{CS}), the dipole-dipole interaction (\hat{H}_D), the quadrupolar interaction (\hat{H}_Q), and the J-coupling (\hat{H}_J). The overall interaction can be then described by a Hamiltonian including the contributions of the interactions.

$$\hat{H} = \hat{H}_z + \hat{H}_{CS} + \hat{H}_D + \hat{H}_Q + \hat{H}_J \quad (4.1)$$

As illustrated in Table 4.1, in most cases the Zeeman interaction is the dominating interaction. However, this interaction is the only one that does not contain structural and dynamic insights regarding the spin system, and only allows to distinguish different nuclei/isotopes, i.e. ^1H , ^2H or ^{13}C , by their nucleus specific property, the gyromagnetic ratio γ .^[115–117]

Table 4.1 Approximate ranges for the different spin interactions.

<i>Interaction</i>	<i>Range of the spin interaction (Hz)</i>
Zeeman	10^6 - 10^9
Chemical shift	0 - 10^5
Dipolar	0 - 10^5
Quadrupolar	0 - 10^9
Scalar Coupling	0 - 10^4

Due to the purposes of this research work, this chapter only describes the Zeeman, chemical shift and the quadrupolar interaction.

4.2 The Zeeman Interaction

The nuclear magnetic moment is proportional to the spin angular momentum:

$$\vec{\mu} = \gamma \hbar \vec{I} \quad (4.2)$$

where \hbar is the Plank's constant divided by 2π , γ is the gyromagnetic ratio ($\text{rad s}^{-1} \text{T}^{-1}$). The gyromagnetic ratio is specific for each NMR nuclei and is a measure of its sensitivity towards the interaction with \vec{B}_0 .

In the absence of any magnetic field, the spin angular momentum of active NMR nuclei is randomly oriented (degenerated state). However, under the influence of an external magnetic field (\vec{B}_0), the degeneration is lifted, leading the I_z component of the spin vector $\vec{I} = (I_x, I_y, I_z)$ to adopt specific orientations that are connected to energy states. This phenomenon, known as Zeeman interaction or Zeeman splitting, is described by the Hamiltonian:

$$\hat{H}_z = -\gamma \hbar \vec{B}_0 I_z \quad (4.3)$$

Under influence of the external field, the nuclear spins precess about an axis parallel to B_0 . The rate of precession is termed as Larmor frequency (ω_0), measured in units of rad s^{-1} , and follows a conical path around the precession axis. ω_0 can be calculated as:^[118]

$$\omega_0 = -\gamma B_0 \quad (4.4)$$

The number of energy levels on which spins can be distributed based on their energy is denoted by the magnetic quantum number $m = 2I + 1$. These energy levels are equally spaced. Assuming \vec{B}_0 is along the z-axis of the laboratory frame $\vec{B}_0 = (0, 0, B_0)$, the energy difference between levels for a two-spin system ($I = \frac{1}{2}$) is given by:

$$\Delta E = \hbar\gamma B_0 \quad (4.5)$$

Each energy level is populated by spins sharing the same direction (energy). The number of nuclei in each spin state follows the Boltzmann distribution, which expresses the temperature-energy relationship:

$$\frac{N_\alpha}{N_\beta} = e^{-\frac{\Delta E}{kT}} = e^{-\frac{\hbar\gamma B_0}{kT}} = e^{-\frac{h\nu}{kT}} \quad (4.6)$$

where N_α and N_β represent the population of nuclei in lower and upper energy states, k is the Boltzmann constant ($1.3805 \times 10^{-23} \text{ J/K}$), and T is the temperature in K. At room temperature and above, only slightly more spins are in the lower energy level.^[119]

To obtain an NMR spectrum involves promoting spin transitions between energy levels through an oscillating magnetic field (\vec{B}_1) possessing the Larmor Frequency of the particular nuclear spin. The amplitude \vec{B}_1 is smaller than \vec{B}_0 , thereby not altering the energy levels. Instead, it induces spin transitions between them. Under these conditions only the components of the \vec{B}_1 field perpendicular to \vec{B}_0 can induce changes. From the quantum mechanical selection rules, spins are allowed to switch only one level at a time ($\Delta m = \pm 1$). This condition is met when the \vec{B}_1 field has with a frequency matching the energy difference between levels (resonance condition):

$$\Delta E = \omega_0 = \gamma B_0 \quad (4.7)$$

The Larmor Frequency corresponds to the precession of the magnetic moment about an external magnetic field, and typically (\vec{B}_1) has to match the Larmor frequency. The coil utilized to produce the \vec{B}_1 field in NMR spectrometers often serves also as detector, that converts the precession of the observable transverse magnetization into an electrical signal.

To describe the effect of rf fields or rf pulses on the $I = \frac{1}{2}$ spin system, a semiclassical approach is employed, considering the net magnetic moment of the spin population as a vector (magnetization vector). Under the influence of \vec{B}_0 , the magnetic moments of the nuclear spins align so that the total magnetic moment is parallel

to \vec{B}_0 , along the z-axis; this state is termed thermal equilibrium (figure 4.1a). Applying an oscillating magnetic field, matching the energy difference between energy levels, causes the net magnetization to precess around the B_1 , altering the direction of the net magnetization and, consequently, the magnetization vector (\vec{M}_z) (figure 4.1b). After a 90° pulse, for example, the magnetization is then rotating in the xy-Plane.

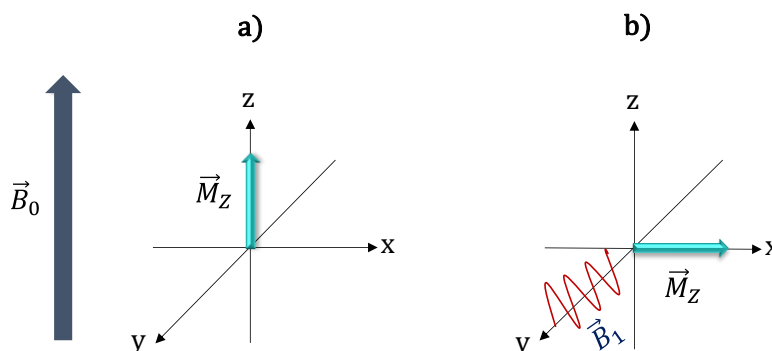


Figure 4.1. Effect of a radio frequency pulse on the energy levels of a spin with $I=1/2$ under a static magnetic field (\vec{B}_0), according to the vector and the population model, respectively, under thermal equilibrium a), and when a radio frequency pulse is applied b).

In modern NMR experiments, the response of nuclear spins to a radiofrequency pulse is measured through the time-domain signal, called free induction decay (FID). The FID is the sum of many exponentially decaying cosine signals (oscillating signal components). The signals' domain is transformed from the time domain to the frequency domain by applying Fourier transformation.^[120]

4.3 Chemical Shift Interaction

The electrons surrounding the nuclei generate a magnetic field (B_i), when brought into a magnetic field, which can oppose or align with the B_0 field, causing a contribution to the effective magnetic field experienced by the nuclei. This results in a change in the Larmor frequency, known as the chemical shielding (σ) or chemical shift (δ). The local magnetic field (B_{loc}) experienced by a nucleus is given by:

$$B_{loc} = \sigma B_0 \quad (4.8)$$

here, σ represents the chemical shielding, influenced by the electronic density.^[121] For non-spherical electron density distributions, σ depends on analyte orientation relative to B_0 , this averages out for solutions, but for ssNMR it means that it depends on crystallite orientation. The orientation dependence of the chemical shift is best described by a tensor, a real 3×3 matrix. Each component of the chemical shift tensor (δ_{ij}) is determined by cross-referencing it with the corresponding component (σ_{ij}) of the chemical shielding tensor from a well-established reference substance (σ^{ref}):^[113]

$$\delta_{ij} = \frac{\sigma_{ij}^{ref} - \sigma_{ij}}{1 - \sigma_{ij}} \quad (4.9)$$

In NMR, the chemical shift interaction significantly affects the shape and width of spectral lines. The chemical shift interaction tensor is typically described in its Principal Axis System (PAS), which pertains to the molecular frame of reference where the tensor is diagonalized. The principal values of this tensor are denoted as δ_{11} , δ_{22} , and δ_{33} .^[113] For a comprehensive understanding of the chemical shift interaction, it is essential to describe its orientation in the laboratory frame, which is the fixed coordinate system in the laboratory where NMR experiments take place. This necessitates establishing a connection between the PAS and the laboratory frame. This connection is achieved through the use of Euler angles, which represent the rotations required to transform the PAS to the laboratory frame.^[122]

Discussions often focus primarily on the principal values of the tensor. These values are commonly expressed using several parameters: the isotropic chemical shift (δ_{iso}), which remains unaffected by orientation; the chemical shift anisotropy (CSA), responsible for line broadening; and the asymmetry parameter (η), instrumental in defining the spectral shape

Principal parameters of the tensor using the Haebleren convention,^[123] assuming $|\delta_{11} - \delta_{iso}| \geq |\delta_{22} - \delta_{iso}| \geq |\delta_{33} - \delta_{iso}|$ are:

$$\delta_{iso} = \frac{1}{3}(\delta_{11} + \delta_{22} + \delta_{33}) \quad (4.10)$$

$$CSA = \delta_{11} - \delta_{iso} \quad (4.11)$$

$$\eta = \frac{\delta_{33} - \delta_{22}}{\delta_{11} - \delta_{iso}} \quad (4.12)$$

In solution, fast molecular tumbling averages out most components of the chemical shift tensor, so that only δ_{iso} is observable in liquid state NMR.

4.4 Magic Angle Spinning

In solid-state NMR spectra, signals are broadened due to orientation-dependent interactions like chemical shift anisotropy and dipolar coupling. To eliminate this dependency, polycrystalline samples are rapidly rotated around an axis at 54.74° (magic angle) to the static magnetic field (B_0). The magic angle is the angle the space diagonal of a cube forms with the z-axis (figure 4.2). When a polycrystalline sample spins around the magic angle, the orientation of crystallite components changes, rendering the anisotropic interaction values of all crystallites time dependent. Only the isotropic component (δ_{iso}) of the chemical shift remains unaffected the spinning.^[122,124]

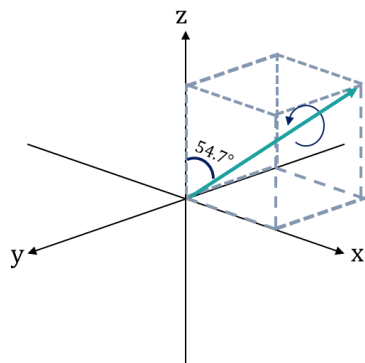


Figure 4.2 Graphical representation of the Magic Angle (54.7°). The x, y and z axes appear symmetric when looking down the space in the diagonal.

The anisotropic interactions follow the second Legendre Polynomial ($3\cos^2\theta - 1$), which captures all the first-order orientation dependencies. The averaging of the anisotropic interactions is calculated according to the formula:

$$\langle 3\cos^2\theta - 1 \rangle = \frac{1}{2}(3\cos^2\theta_R - 1)(3\cos^2\beta - 1) \quad (4.13)$$

where θ_R is the angle between the rotational axis and B_0 , and β is the angle between the rotation axis and the z-axis of the chemical shift tensor. If $\theta_R = 54.7^\circ$, then $3\cos^2\theta_R = 0$.

Depending on the spinning speed, a particular anisotropic interaction can be partially or completely averaged out.^[124] When the rotation frequency is smaller than a particular broadening interaction strength in Hz, the anisotropic interactions are incompletely averaged, leading to artificial peaks within the spectrum, so called spinning sidebands. The rotation of the samples causes the crystallites and their associated chemical shift tensor to rotate as well. The strength and direction of the interaction change with spinning, resulting in a modified evolution frequency. The evolution frequency resets to its starting value after a complete rotation. The continuous repetition of this spin state evolution spaced one rotor period apart from one another is called a rotational echo sequence. The resulting solid-state NMR spectra from a rotational echo consist of sharp signals spaced by integer multiples of the spinning speed rate. One of these signals corresponds to the Fourier transform of δ_{iso} , which, as mentioned earlier, is unaffected by the spinning rate. The additional signals are commonly referred to as spinning sidebands (SSB).^[122]

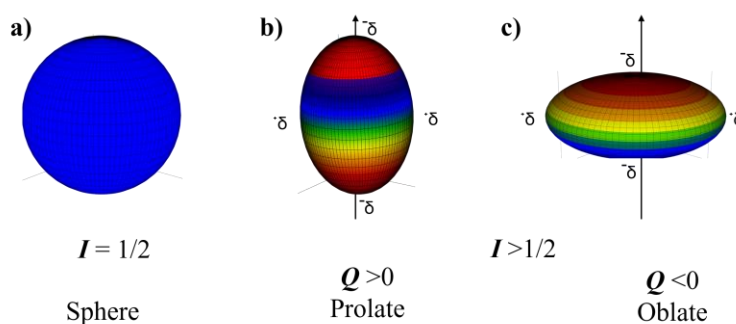
4.5 Quadrupolar Interaction

Spins with a spin quantum number larger than $\frac{1}{2}$ are known as quadrupolar nuclei, constituting approximately 74% of the nuclei active for NMR.^[125] Table 4.2 presents some examples of such nuclei.

Table 4.2. Properties of some nuclei.^[119]

Nuclei	Spin (I)	Natural abundance (%)	Magnetogyric ratio	NMR frequency
			$\gamma/10^7 \text{ rad T s}^{-1}$	ν/MHz
^1H	1/2	99.985	26.7520	400.0000
^2H	1	0.015	4.1066	61.402
^7Li	3/2	92.58	10.3975	155.454
^{13}C	1/2	1.108	6.7283	100.577
^{15}N	1/2	0.37	-2.712	40.531
^{17}O	5/2	0.037	-3.6279	54.227
^{19}F	1/2	100	25.181	376.308
^{23}Na	3/2	100	7.08013	105.805
^{27}Al	5/2	100	6.9760	104.229

Nuclei with $I = \frac{1}{2}$ exhibit a symmetrical charge distribution (Figure 4.3a). In contrast, for values of I larger than $\frac{1}{2}$, the charge distribution is no longer symmetrical (Figure 4.3b). This charge distribution is characterized by the nuclear quadrupolar moment (Q), which can be described as a second-rank tensor.

**Figure 4.3.** Geometry and charge distribution in the nuclei according to the value of a) $I = \frac{1}{2}$, b, c) $I > \frac{1}{2}$.

The nuclear quadrupolar moment interacts with the electric-field gradient (EFG) generated by electrons or any charged particle close to the nuclei. The EFG can also be represented as a second-rank Cartesian tensor (V). This tensor possesses the characteristic of being traceless ($V_{xx} + V_{yy} + V_{zz} = 0$), a consequence of the Laplace equation. Consequently, V can be diagonalized in the PAS as shown in Equation 4.14:

$$V = \begin{pmatrix} V_{xx} & V_{xy} & V_{xz} \\ V_{yx} & V_{yy} & V_{yz} \\ V_{zx} & V_{zy} & V_{zz} \end{pmatrix} \rightarrow \begin{pmatrix} V_{xx} & 0 & 0 \\ 0 & V_{yy} & 0 \\ 0 & 0 & V_{zz} \end{pmatrix} \quad (4.14)$$

$$\text{with } |V_{zz}| \geq |V_{yy}| \geq |V_{xx}| = 0$$

The shape of the EFG is characterized by the asymmetry parameter (η_Q), which indicates the deviation of the EFG from axial symmetry. η_Q can be calculated with the eq. 4.15.^[126]

$$\eta_Q = \frac{V_{xx} - V_{yy}}{V_{zz}} \quad (4.15)$$

Using our definition from 4.16 η_Q can take values from 0 to 1.

The magnitude of the interaction between the nuclear electric quadrupole moment and the electric field gradient is represented by the quadrupolar coupling constant (C_Q):

$$C_Q = \frac{e^2 V_{zz} Q}{h} \quad (4.16)$$

where e is the elementary charge, V_{zz} is the largest component of the EFG, and Q is the scalar nuclear electric quadrupole moment (for deuterium $2.875 \times 10^{-31} \text{ m}^2$).^[117,127]

Despite the quadrupolar interaction potentially being large, in most cases it is still smaller than the Zeeman interaction. However, the quadrupolar interaction modifies the eigenvalues of the Zeeman Hamiltonian, causing a shift in the Zeeman energy levels (Figure 4.4). Mathematically, these disturbances are included as corrections to the energy between the levels, following perturbation theory. Usually, the first order (H_Q^1) and second order (H_Q^2) terms are considered.^[126,128]

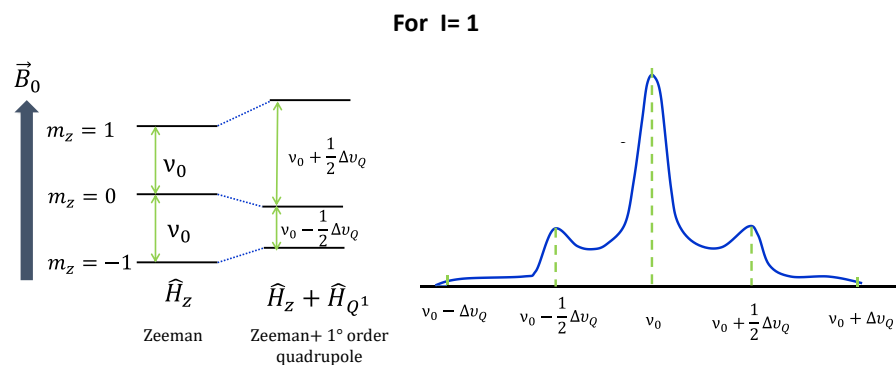


Figure 4.4 Left: Energy levels and the corresponding quadrupole splits for spin $I=1$. The \hat{H}_Z is the Hamiltonian for the Zeeman interaction, \hat{H}_{Q^1} the Hamiltonian for quadrupolar interaction of first order, $\Delta\nu_Q$ represents the quadrupolar splitting. Right: schematic ^2H solid state NMR spectrum of a powder sample resulting from a superposition of nuclei without (central Lorentzian) and with quadrupolar splitting (broad Pake pattern).

As depicted in Figure 4.4, the first-order term results in a shifting of the energy levels. For half-integer quadrupolar nuclei, the energy difference between $m_z = +\frac{1}{2}$ and $m_z = -\frac{1}{2}$, known as the central transition (CT), remains unaffected. Additional transitions, adhering to the selection rule $\Delta m_z = \pm 1$, are termed satellite transitions (ST). The energies of these transitions are influenced by the magnitude of the quadrupolar interaction and the orientation of the EFG concerning the external magnetic field. In polycrystalline samples, they give rise to a Pake pattern, often too broad to be fully observed via single-pulse excitation.^[110,129,130]

The term used to denote the energy correction is "quadrupolar splitting" ($\Delta\omega_Q$ or $\Delta\nu_Q$), and for first-order corrections, it follows equation

$$\Delta\nu_Q(\theta, \phi) = \frac{3C_Q}{4I(2I-1)} [3\cos^2(\theta) - 1] - \eta\sin^2(\theta)\cos(2\phi) \quad (4.17)$$

Where θ and ϕ are defined as the angles between the PAS of the EFG and the laboratory frame, as showed in the Figure 4.5

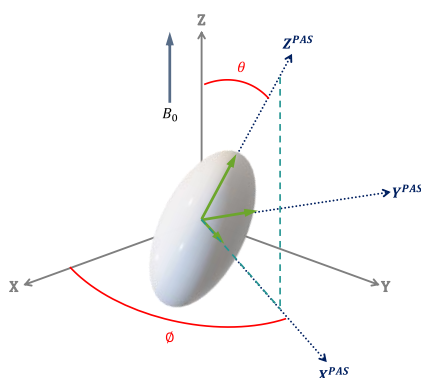


Figure 4.5. Position of the EFG with respect to the laboratory frame

The second-order perturbation term affects the energy differences of all transitions. In polycrystalline samples, its angular dependence even causes the CT to exhibit an anisotropically broadened line shape. This term also contains an isotropic component, the quadrupolar-induced shift, which determines the signal positions in the resulting NMR spectra in addition to the isotropic chemical shift. The impact of the second-order perturbation term can be mitigated by increasing the strength of the external magnetic field, as it depends inversely on this field's magnitude.

4.6 Deuterium Solid state NMR

Deuterium (^2H) solid-state NMR spectroscopy presents a robust approach for investigating molecular dynamics across a broad range of time scales, spanning from 10^{-3} to 10^{12} s^{-1} .^[114,130,131] The utilization of deuterated compounds offers a unique avenue to explore reorientation dynamics at specific sites. Notably, the EFG aligns

parallel to the chemical bond in deuterium-bearing molecules, facilitating the observation of bond reorientation phenomena under diverse conditions.

In NMR, the quadrupolar splitting frequency is intricately tied to the angle θ of the bond between the D and the nucleus to which it is bonded (X), concerning the external magnetic field. This relationship is governed by the equation

$$\omega = \omega_0 \pm \frac{3}{8} \left(\frac{e^2 Q V_{zz}}{\hbar} \right) (3 \cos^2 \theta - 1) \quad (4.18)$$

In polycrystalline samples, when subjected to Magic Angle Spinning (MAS) conditions, each orientation of the X-D bond becomes discernible by observing the characteristic doublet splitting as a function of the angle θ (Figure 4.6 a). Conversely, under static conditions, the cumulative effect of the diverse orientations of the X-D bond relative to the external magnetic field gives rise to a distinct pattern known as the "Pake pattern" (illustrated in Figure 4.6 b).^[118]

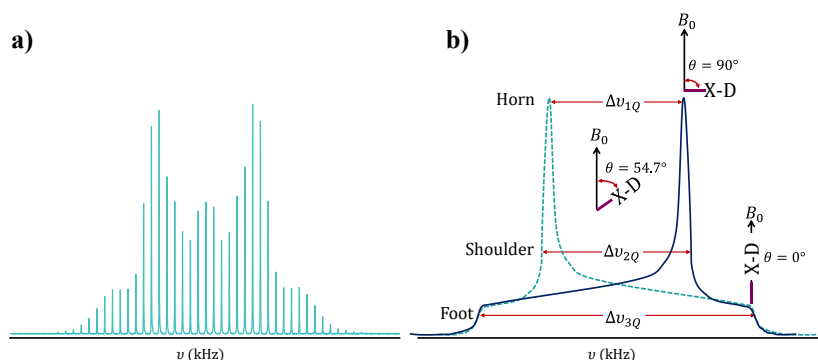


Figure 4.6. Spectra of polycrystalline sample under: a) MAS conditions, b) Static conditions sample. The Figure shows the orientation dependency of the X-D respect to B_0 .

This Pake pattern, marked by its appearance in the NMR spectrum, emerges as a superposition of two axially symmetric distributions intersecting at the magic angle (54.7°). The pattern is characterized by three distinct features: "horns," "shoulders," and "feet," each defined by frequencies denoted as $\Delta\omega_{1Q}$, $\Delta\omega_{2Q}$ and $\Delta\omega_{3Q}$, respectively. The calculation of these frequencies involves the following expressions:^[118]

$$\Delta\nu_{1Q} = \Delta\nu_{2Q} = \frac{3}{4} C_Q (1 - \eta_Q) \quad (4.19)$$

$$\Delta\nu_{3Q} = \frac{3}{2} C_Q \quad (4.20)$$

As deuterium within the C-D bond undergoes a gradual motional process on the NMR timescale, the distinctive Pake pattern shape becomes highly prominent. However, as ^2H enters the fast exchange regime, the frequencies

associated with the two horns, shoulders, or feet of the pattern progressively decrease, eventually leading to their merging.^[131]

From an experimental standpoint, due to deuterium's relatively small quadrupolar moment, spectra can be acquired using spin-echo techniques.^[130] Subsequently, various software tools can be employed to extract concealed parameters from the spectral line shapes. Additionally, other experiments aimed at elucidating dynamics within the systems are those focusing on relaxation processes.

4.7 Spin Echo Sequence

For this pulse sequence under static conditions, the magnetization vector (\vec{M}_z) is flipped into the xy plane by a 90° pulse. Followed by an evolution time, during which the influence of the surroundings will be reflected in the precession rates of the spins. When the magnetization vector reaches its minimal value, a 180° pulse is applied to rotate all components (as illustrated in Figure 4.7a). The echo will appear after a waiting period.

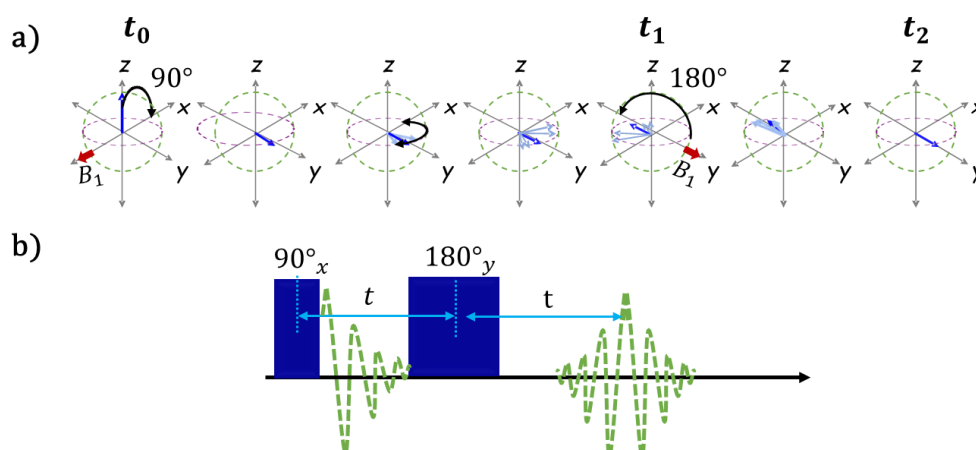


Figure 4.7 Schematic representation of a) The evolution of the magnetization vector (\vec{M}_z) during the Spin echo sequence b) Spin echo pulse sequence.

4.8 Longitudinal and Transversal Relaxation

In an NMR experiment, when a spin system is perturbed (usually by a radio-frequency pulse), the process by which it returns to its equilibrium state is referred to as relaxation. There are two main relaxation processes in NMR: (i) spin-lattice relaxation, characterized by the time constant T_1 , and (ii) spin-spin relaxation characterized by T_2 .

Longitudinal relaxation (T_1) is a non-energy conserving process that describes how the magnetization vector returns to the thermal equilibrium state along the direction of the external B_0 field. In liquids, this process occurs

typically within the range of milliseconds (ms) to seconds (s), while in solids, it can range from milliseconds to days.

Transverse relaxation describes the loss of phase coherence, or in other words, the decay of the individual components of the magnetization vector in the transverse plane. The time scale for this energy conserving process in liquids is typically the same as for T_1 , i.e., within the range of milliseconds (ms) to seconds (s). However, in solids, the T_2 relaxation can have an order of microseconds. Both relaxation processes exhibit in general exponential behavior and offer insights into dynamic processes.

To determine the longitudinal relaxation time, a saturation recovery experiment can be employed (Figure 4.8a). This experiment entails irradiating the sample with a 90° pulse train, followed by an evolution time, and finally applying a 90° probe pulse and acquiring data. This procedure is repeated multiple times with varying the evolution time. To calculate T_1 , the relative areas of the signals in the spectra are plotted against the evolution times. In simple cases, the evolution of magnetization can be described by the equation:

$$A_z(t) = A_z(0) \left[1 - e^{-t/T_1} \right] \quad (4.21)$$

where A_z is the relative area of the signal and t is the time (s).

For transverse magnetization, a standard Hahn echo or spin-echo experiment, as described earlier, can be employed. During a spin-echo under MAS conditions, the experiment must be performed with rotor synchronization under MAS (Figure 4.8b). Synchronization is crucial to retain information about the CSA. An inconvenience of performing this sequence under MAS is that if the T_2 relaxation time of the nuclei is shorter than the time required for one rotor period, no signal will be acquired. A solution to overcome this, is the use of fast spinning rates, where the rotor periods become shorter.

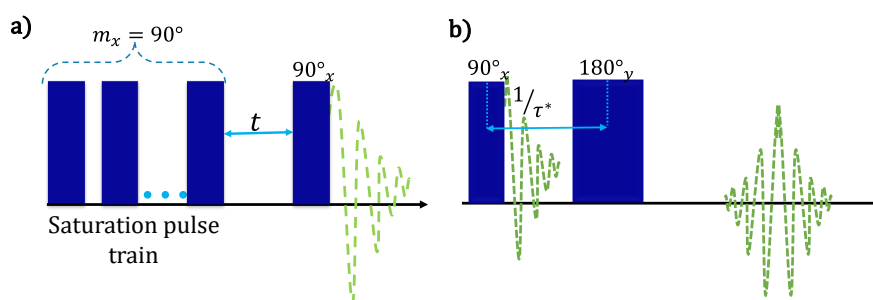


Figure 4.8 a) Pulse sequence of a saturation recovery experiment b) pulse sequence of a spin echo with rotor synchronization. τ^* is the spinning frequency.

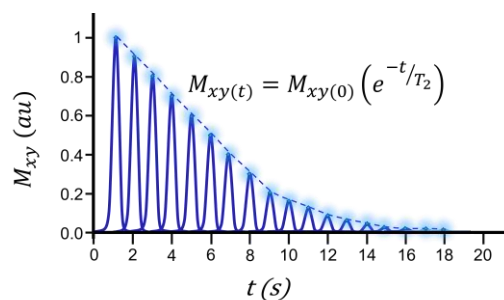


Figure 4.9. Schematic plot of the transversal magnetization (M_{xy}) versus time (t) that can be used to determine T_2 .

As for T_1 , to calculate T_2 , the relative area of the echo signals in the spectra is plotted against the time (t) at which they were obtained during the experiment (Figure 4.9). T_2 is then obtained by fitting the points using equation 4.22.

$$A_{xy}(t) = A_{xy(0)} \left(e^{-t/T_2} \right) \quad (4.22)$$

where A_{xy} is the relative area of the signal and t is the time (s).

The experiments described above are not the only ones used to study molecular dynamics through relaxation; spin-lattice relaxometry (SLR) and simulated-echo (STE) studies can also be employed.^[132–135] However, since the latter two methods were not utilized in this work, they won't be explained here

5 Dynamic Nuclear Polarization

NMR Spectroscopy is a versatile technique employed across various fields. It offers several advantages, including the ability to analyse crystalline or amorphous analytes, non-destructive sample measurement, and the potential to obtain reliable structural, quantitative, and dynamic information. However, it grapples with a significant limitation: its inherent sensitivity issue.^[33–35]

To address this sensitivity challenge, several strategies can be implemented. These include utilizing spectrometers with high magnetic fields, increasing the concentration of relevant nuclei within the sample, conducting experiments at lower temperatures (cryogenic conditions), employing specialized pulse sequences, and exploring hyperpolarization techniques.

Hyperpolarization techniques alter the magnetic properties of the analyte, driving the spin system away from equilibrium and resulting in signal enhancement during NMR experiments.^[33] Numerous hyperpolarization techniques have been developed, including Dynamic Nuclear Polarization (DNP), para-Hydrogen-Induced Polarization (PHIP), Dissolution DNP (d-DNP), Signal Amplification By Reversible Exchange (SABRE), Chemically Induced Dynamic Nuclear Polarization (CIDNP), and Spin Exchange Optical Pumping (SEOP), among others.^[33–35,136]

For the purposes of this research, this chapter will focus solely on outlining the fundamental principles of Dynamic Nuclear Polarization (DNP). It will commence with a general introduction to DNP and its requirements for its implementation, followed by an exploration of its underlying mechanisms. This foundation will pave the way for a deeper understanding of DNP's role in enhancing NMR sensitivity and its application in various research areas.

5.1 Generalities of DNP

The intensity of a NMR signal is directly related to the population difference between nuclear spin energy levels, as given by the Boltzmann distribution, expressed in equation (4.6).^[109]

In conventional NMR experiments, without introducing any modifications to the apparatus, the signal-to-noise ratio (S/N) can be improved through the repetition of the experiment sequence, referred to as “scans” or “signal averages,” denoted as “n” times. This process can be continued until the signal-to-noise (S/N) ratio reaches an acceptable level. Unfortunately, due to the considerable time the spin system needs to return to its initial state (thermal equilibrium) between scans, the overall experiment duration can become impractical. This concern becomes even more pronounced when dealing with nuclei of low abundance and/or possessing a low

gyromagnetic ratio (low- γ). Such nuclei already demand significant experimental durations, even with minimal time intervals between scans.^[34]

In contrast, the Dynamic Nuclear Polarization (DNP) technique offers a solution by causing a perturbation of the Boltzmann distribution (as illustrated in figure 5.1), rather than solely relying on increased scan repetitions. This approach results in significant signal enhancements that surpass the quality achievable with standard solid-state NMR.

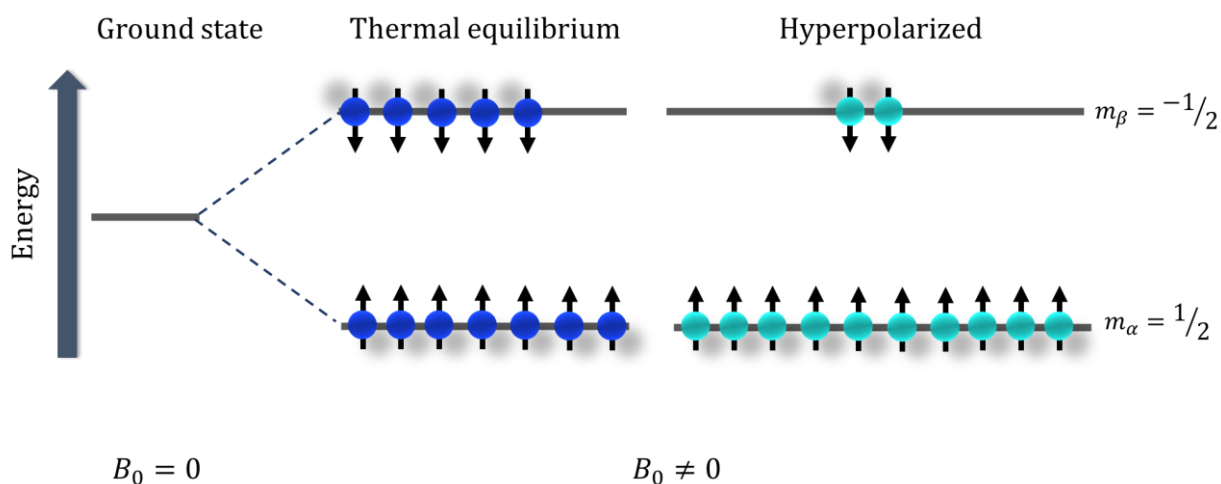


Figure 5.1. Schematic of Spin population distribution for a spin with $I = \frac{1}{2}$ in the presence of the magnetic field (royal blue) under hyperpolarized effects (cyan).

During a DNP experiment, the polarization of an unpaired electron (S) is transferred to the nuclei of interest (I) through microwave radiation (μw). To facilitate this transfer, the unpaired electron must be near the nucleus of interest, allowing for a hyperfine interaction to occur, leading to the transfer of electron polarization. The electron-nuclear system is governed by the Hamiltonian:

$$\begin{aligned}
 H &= H_S + H_I + H_{SI} = \omega_{0S} - \omega_{0I}I_z + H_{SI}^{iso} + H_{SI}^{dip} \\
 &= \omega_{0S}S_z - \omega_{0I}I_z + A(S_zI_z + S_yI_y + S_xI_x) + BS_xI_z
 \end{aligned} \tag{5.1}$$

where ω_{0e} and ω_{0I} represent the Larmor frequencies for the electron spin and the nuclear spin, respectively. S_i and I_i denote the electron and nuclear spin operators, while H_{SI}^{iso} signifies the isotropic (Fermi contact) hyperfine interaction between the electron and the nucleus. Additionally, H_{SI}^{dip} accounts for the anisotropic hyperfine coupling between electron and nuclear spin via space. Parameters A and B correspond to the secular and pseudo-secular hyperfine interactions. All these hyperfine interactions result in minor energy level shifts and splittings, contributing to the overall complexity of the system.

In summary, DNP exploits the interaction between an unpaired electron and the nuclei of interest, facilitated by microwave radiation, to enhance nuclear polarization. The resulting interplay of hyperfine interactions, including isotropic and anisotropic components, impacts the energy level structure and dynamics of the system.

To implement this technology, supplementary equipment is required, including a microwave source, a suitable probe, and the utilization of polarizing agents, among others.

5.2 Implementation of DNP-NMR

For the purpose of conducting ssNMR experiments enhanced by DNP, in addition to the ssNMR spectrometer, specific components are necessary, as depicted in Figure 5.2. These additional components consist of: (i) a cryogenically cooled probe capable of reaching temperatures around 100 K, and connected to a (ii) microwave source, often a gyrotron. The probe and gyrotron are linked by means of a (iii) transmission line, facilitating the transmission of microwaves generated by the gyrotron to the sample. Supplementary accessories for temperature and microwave control are also integrated into the setup.^[137]

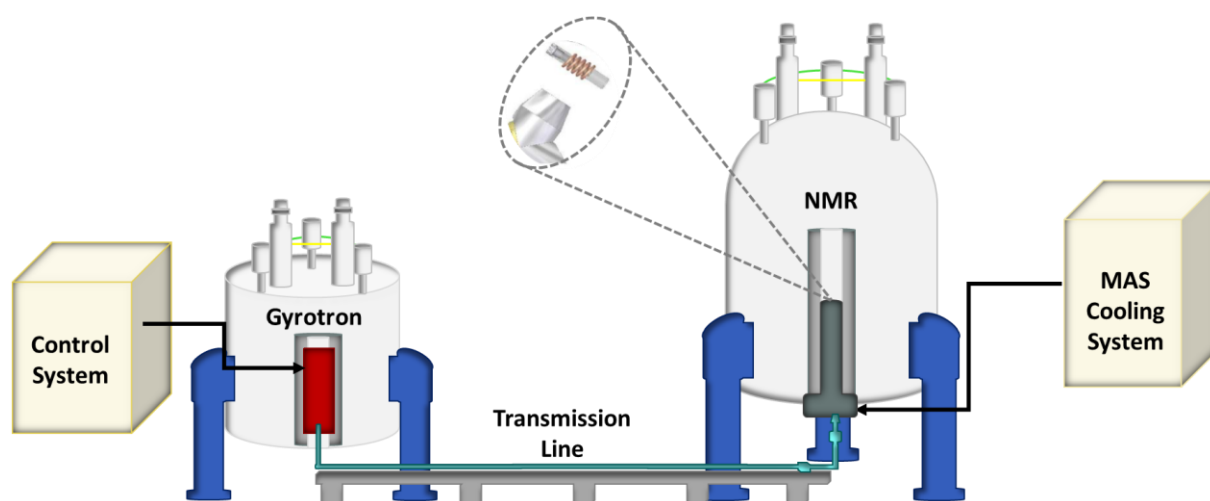


Figure 5.2 Schematic diagram of the commercial MAS DNP NMR employed with Gyrotron (red), a waveguide (cyan) and low temperature NMR probe (green). Adapted from the reference.^[138]

Alongside these extra components, the DNP technique requires the presence of a source of unpaired electrons, known as polarization agents (Pas), which can be introduced into the sample or arise from endogenous sources.^[45,138,139] Polarization agents typically encompass stable free radicals or metal ions with unoccupied *d* or *f* orbitals.^[36] Given that most samples lack inherent sources of unpaired electrons, Pas are frequently added to the sample, often in a solvent mixture that forms a glass upon freezing. It is crucial that the radical solution freezes uniformly as a glass, preventing the formation of ice crystals, thereby ensuring an even distribution of polarizing agents and preventing their aggregation. A homogeneous glassy DNP sample maximizes the DNP efficiency.^[34,45] Frequently used Pas are typically dissolved in a D₂O/H₂O aqueous matrix with a cryoprotectant

such as DMSO- d_6 or glycerol- d_8 ; organic solvents like tetrachloroethane can also be utilized. Typically, concentrations of the radical in the matrix range from 5 to 50 mM. The presence of H₂O provides the necessary protons that enable proton spin diffusion, aiding in the spread of polarization throughout the sample.^[34]

The commonly employed radicals for high-field DNP are TOTAPOL, AMUPol, TEKPol, BDPA, Trityl, and bTbk.^[47,48,50–54,139–145] Their molecular structures are displayed in Figure 5.3.^[33,40]

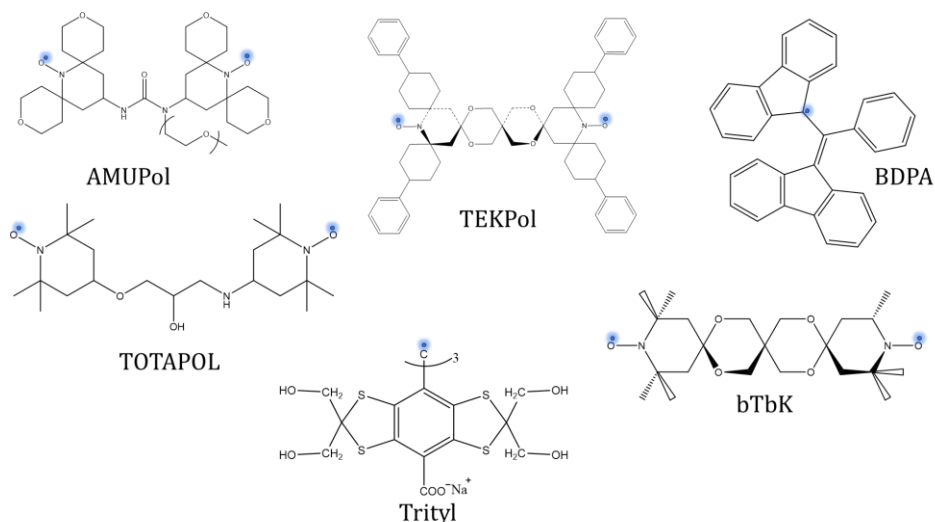


Figure 5.3. Molecular structures of polarization agents (Pas) commonly used for high field DNP experiments. Blue dots denote the unpaired electrons.

The analytes can either be dissolved in the radical solution or impregnated with a radical solution, depending on their nature. For many biomolecular investigations, the dissolved approach has proven effective, often involving precipitation or sedimentation. Impregnation, on the other hand, is commonly employed for organic, inorganic, and hybrid materials, as well as powdered molecular solids. Unlike the dissolved approach, impregnation involves depositing a small amount of the radical-containing solution onto the dry sample.^[34]

5.3 Cross Polarization (CP)

This technique aims to enhance the signal intensity of nuclei in solid-state NMR spectrum of nuclei with low natural abundance and low gyromagnetic ratio (γ), such as ¹⁵N, ¹³C, and ²⁹Si. During these experiments, polarization is transferred from a spin system with high abundance and high gyromagnetic ratio (I-spin), usually ¹H or ¹⁹F, to a less favored spin system (X-spin). The Cross Polarization (CP) mechanism is based on the simultaneous change of spin states in a coupled spin system ($\alpha_x\beta_I \rightarrow \beta_x\alpha_I$). This flip-flop process conserves energy, which means that the energy needed to switch the X-spin from α to β must be equal to the energy needed to switch I from β to α . This condition cannot be satisfied in the laboratory frame, only in the rotating frame. Therefore, to induce this phenomenon, simultaneous application of RF fields is essential (Figure 5.4). The applied RF fields must satisfy the Hartmann-Hahn condition (eq 5.2)^[109]

$$\gamma_I B_{I1} = \gamma_X B_{X1} \quad (5.2)$$

where γ_I is the gyromagnetic ratio for I, γ_X is the gyromagnetic ratio for X, B_{I1} and B_{X1} are the corresponding RF field strengths.

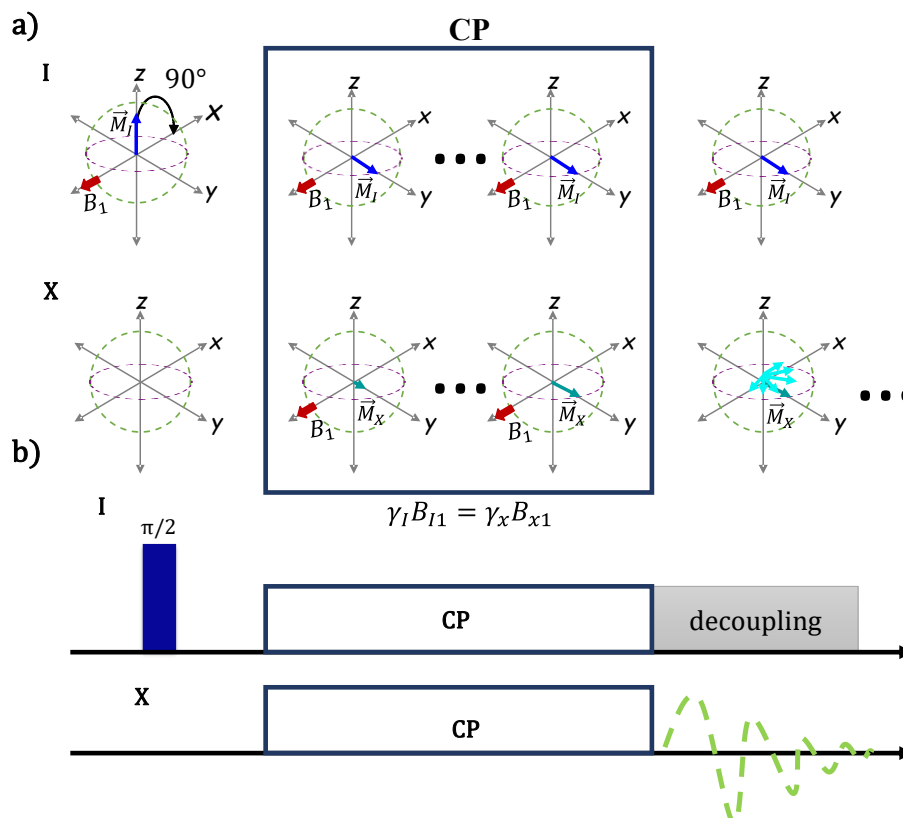


Figure 5.4. Typical CP pulse sequence, I denote the high abundant and high gyromagnetic ratio spin and X is the low abundant and moderate gyromagnetic ratio spin. A) The evolution of both magnetization vectors (\vec{M}_I and \vec{M}_X) during the CP sequence b) Spin echo pulse sequence.^[112]

The RF fields that satisfy the Hartmann-Hahn conditions are often referred to as spin-lock pulses. When applied, these spin-lock pulses lead both spins to precess in the same plane, yielding an efficient polarization transfer from I to X.

When CP is performed under Magic Angle Spinning (MAS) conditions, a ramped spin-lock pulse is often used instead of a constant one. This ramp is mostly increased linearly over time, covering the Hartmann-Hahn matching conditions under MAS that are given by:

$$\omega_I \pm \omega_X = n\omega_r \quad (5.3)$$

where ω_I is the Larmor frequency of the I-spin, ω_X is the Larmor frequency of the X spin, ω_r is the spinning rate, and n is a multiple of the magic angle spinning rate. A more detailed description of CP under MAS can be found in the literature.^[109,110,113,146,147]

5.4 Solid Effect (SE)

This mechanism requires an unpaired electron (S) and a nucleus (I) that are hyperfine coupled. To elucidate this polarization pathway, an energy diagram is presented in Figure 5.5, illustrating the various transitions between energy levels. The transitions $|1\rangle \leftrightarrow |3\rangle$ and $|2\rangle \leftrightarrow |4\rangle$ correspond to allowed transitions in Electron Paramagnetic Resonance (EPR). In NMR, following selection rules, transitions $|3\rangle \leftrightarrow |4\rangle$ and $|1\rangle \leftrightarrow |2\rangle$ are allowed, while $|2\rangle \leftrightarrow |3\rangle$ and $|1\rangle \leftrightarrow |4\rangle$ are forbidden. However, these seemingly forbidden transitions contribute to the polarization transfer mechanisms. Pseudo-hyperfine interactions between $|2\rangle \leftrightarrow |3\rangle$ and $|1\rangle \leftrightarrow |4\rangle$ induce mixing of adjacent states. Consequently, the states are no longer $|\beta_S\beta_I\rangle$ and $|\alpha_S\alpha_I\rangle$, but rather $p_i|\beta_S\beta_I\rangle - q_i|\beta_S\alpha_I\rangle$ and $p_i|\alpha_S\alpha_I\rangle + q_i|\alpha_S\beta_I\rangle$, where p_i and q_i are mixing coefficients. As a result, the forbidden Zero Quantum (ZQ) and Double Quantum (DQ) transitions become partially allowed.^[139,148]

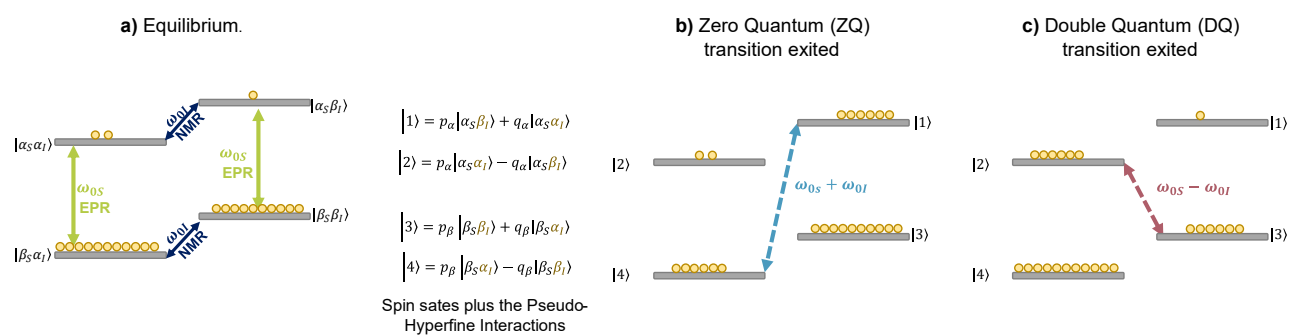


Figure 5.5. Energy level diagram describing the Solid Effect mechanism for of a coupled electron-nuclear spin system ($S=I=1/2$). ZQ and DQ are the Zero Quantum and Double Quantum transitions, ω_{0S} and ω_{0I} are the Larmor frequencies for the electron and nuclear spins. The dashed arrows indicate the ZQ and DQ transitions, the population of the different energy levels (grey bars) are illustrated by the yellow circles, a) Energy diagram distributions and the allow transition before the polarization transfer, b) Energy diagram distribution after the Zero Quantum transition is exited c) Energy diagram distribution after the Double Quantum transition is exited.

For an efficient polarization transfer by SE, the Larmor frequency of the nuclear spin (ω_{0I}) must exceed both the homogeneous (δ) and inhomogeneous (Δ) EPR line widths. These conditions facilitate the mixing of adjacent states, enabling the partial allowance of the forbidden transitions. To induce the SE mechanism, the sample has to be irradiated with microwaves at a frequency of $\omega_{0S} \pm \omega_{0I}$, corresponding to the excitation frequency of the forbidden transitions (ZQ and DQ).

This mechanism is highly efficient when using a narrow-line radical (e.g., BDPA, trityl, etc.) as the polarizing agent.

5.5 Overhauser Effect (OE)

The Overhauser Effect (OE) operates through the hyperfine coupling between an electron spin and a nuclear spin. To initiate this mechanism, both electron transitions must be simultaneously excited, causing a disruption

in the equilibrium population of the Zeeman levels of the electron spins (S). This disturbance facilitates the occurrence of simultaneous flips involving one nuclear spin (I) and one electron spin (S) via cross relaxation, making otherwise forbidden transitions viable.^[149] For instance, the Zero Quantum transition (ZQ) transitions, such as $\alpha_S\beta_I \leftrightarrow \beta_S\alpha_I$, and the Double Quantum transition (DQ), like $\alpha_S\alpha_I \leftrightarrow \beta_S\beta_I$, which are usually forbidden, become allowed with this effect.

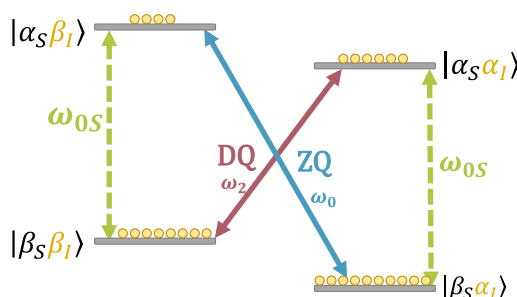


Figure 5.6 Energy level diagram describing the Overhauser mechanism for a coupled electron-nuclear spin system. ZQ and DQ are the Zero Quantum and Double Quantum transitions, ω_{0S} is the Larmor frequency for the electro spin, ω_0 and ω_2 , are the relaxation times for ZQ and DQ respectively. The dash arrows show the transition that are irradiated. The solid arrow transitions induced by relaxation. The population of the different energy levels (grey bars) are illustrated by the size of the yellow circles. Adapted from reference^[35]

To induce the Overhauser effect (OE) as illustrated in Figure 5.6, the transitions $|1\rangle \leftrightarrow |3\rangle$ and $|2\rangle \leftrightarrow |4\rangle$ are irradiated with a frequency of ω_{0S} , disturbing the thermal equilibrium of the electron spin system. If the electron spin is coupled to a nuclear spin through hyperfine interactions, the relaxation mechanism that returns the electron spins to thermal equilibrium, cause them to flip back to their initial positions, will also induce a flip of the nuclear spin (cross relaxation). The positive or negative enhancement obtained depends on the ratio of relaxation rates ω_0 and ω_2 for the ZQ and DQ transitions, respectively.^[139]

5.6 Cross Effect (CE)

The mechanism of the Cross Effect (CE) involves the interaction of three spins: two dipolar-coupled electron spins (S_1 and S_2), situated in close proximity, and a nuclear spin (I) that has a hyperfine coupling with one of the electron spins.^[45] To execute the CE, a crucial condition is that the difference between the Larmor frequencies of the electron spins (ω_{0S1} for electron spin 1 and ω_{0S2} for electro spin 2) match the Larmor frequency of the nucleus:

$$|\omega_{0S1} - \omega_{0S2}| = \omega_{0I} \quad (5.4)$$

This matching condition is commonly fulfilled by radicals with high g-tensor anisotropy (analog to CSA in NMR), like radicals based on nitroxides. The Cross Effect is typically observed in samples with high radical concentrations or in samples containing bi-radicals, which are molecules consisting of two mono-radicals linked

by a molecular connector. Additionally, it is imperative that the dipolar interaction between the two electron spins is sufficiently strong.^[150]

The CE can be described with an energy level diagram containing eight-spin states depicted in Figure 5.7. for the three-spin system $\{|S_1, S_2, I\rangle\}$.

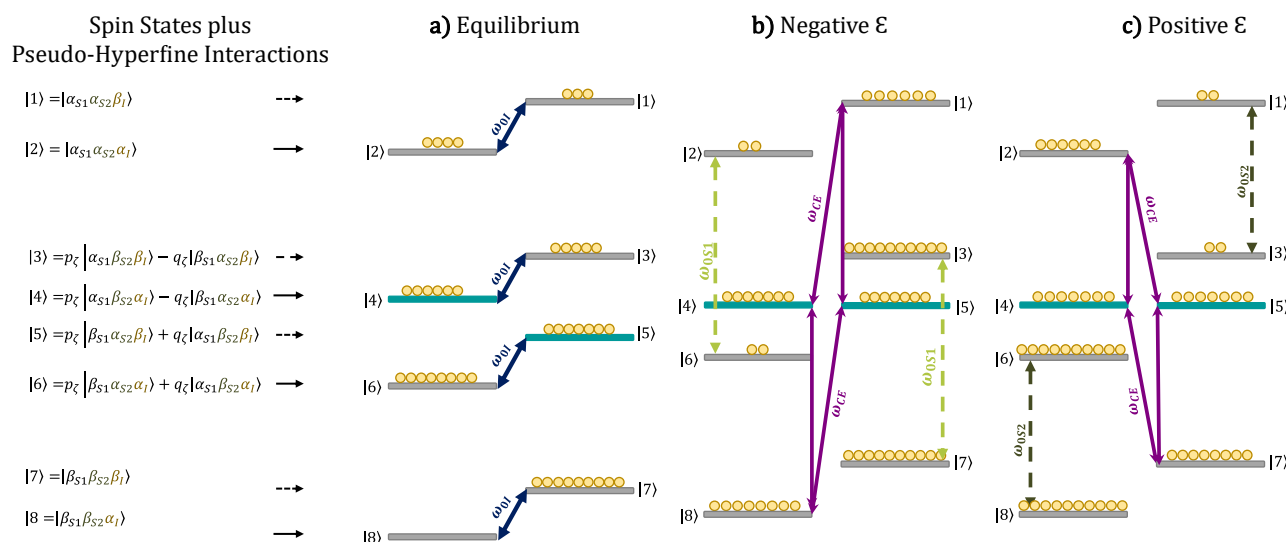


Figure 5.7. Energy level diagram describing the CE mechanism for a three spins system involving electrons (S_1) and (S_2), and a nucleus (I), levels $|4\rangle$ and $|5\rangle$ (turquoise bars), a) General population of spin states in thermal equilibrium, b) Saturation of single quantum electron transitions of electron spin 1 (S_1) leads to negative enhancement, c) Saturation of single quantum electron transitions of electron spin 2 (S_2) leads to positive enhancement. The solid deep blue arrows show the allowed single quantum transition for the nuclear spins in NMR, the purple the responsible for the CE effect. The dash arrows show the irradiated frequencies, the population of the different energy levels (grey bars) are shown by the amount of the yellow circles. Adapted from ref^[40]

Upon satisfying the matching condition, the energy levels $|4\rangle$ and $|5\rangle$ or $|6\rangle$ and $|3\rangle$ undergo a shift, resulting in each energy level acquiring an equivalent population as its counterpart. This degeneracy induces state mixing, allowing previously forbidden transitions to become permissible. The Cross Effect occurs when the system is irradiated with microwaves of frequencies matching one of the two electron Larmor frequencies (ω_{0S_1} or ω_{0S_2}). A negative enhancement (Figure 5.7b) arises from the saturation of the electron with the higher EPR frequency^[33]. For instance, if the matching condition is met, and energy levels $|4\rangle$ and $|5\rangle$ are degenerated, and the system is irradiated at the frequency ω_{0S_1} ; the transitions $|1\rangle \leftrightarrow |4\rangle$ and $|5\rangle \leftrightarrow |8\rangle$ become saturated. This disrupts thermal equilibrium, equalizing the spin population of the electron spin system. Consequently, the population of energy levels $|3\rangle \leftrightarrow |7\rangle$ and $|2\rangle \leftrightarrow |6\rangle$ is also equalized. This redistribution of population causes the negative enhancement^[45].

Conversely, the positive enhancement results from the saturation of the electron levels with the lower energy (Figure 5.7c). As it was described above, when the specified matching condition is met and there is degeneracy between energy levels $|4\rangle$ and $|5\rangle$, and the system is exposed to radiation at the frequency ω_{0S_2} ; the transitions

$|2\rangle \leftrightarrow |5\rangle$ and $|4\rangle \leftrightarrow |7\rangle$ become saturated. This disrupts thermal equilibrium, equalizing the spin population within the electron spin system. Consequently, the population of energy levels $|1\rangle \leftrightarrow |3\rangle$ and $|6\rangle \leftrightarrow |8\rangle$ is also equalized leading to an enhancement^[45]

5.7 Thermal Mixing (TM)

This mechanism is closely related to the Cross Effect. However, unlike other mechanisms, it involves the participation of multiple electron spins and a single nuclear spin. The participating electron spins must be strongly dipolar-coupled, while the nuclear spin must be hyperfine-coupled^[45].

The process of polarization transfer in the Thermal Mix (TM) consists of two steps: (i) the polarization of the electron spins is transferred to the directly hyperfine-coupled nuclear spin through the irradiation of microwaves, and subsequently, (ii) the polarization propagates to the target nuclei via homonuclear spin diffusion. Due to the involvement of numerous spins, describing this mechanism in detail is more complex, but it can be accomplished using either the concept of spin temperature or a diagram with multiple energy levels.^[151]

The polarization agent used to facilitate the polarization transfer in the TM requires a homogeneous EPR linewidth greater than the Larmor frequency of the nuclei being polarized. Typically, high radical concentrations and low temperatures ($T \sim 10$ K) help to achieve this condition.^[36,45]

5.8 Direct and Indirect Polarization

The most common mechanisms for hyperpolarization transfer have been described above. Nevertheless, in ^{13}C experiments, it has been observed that polarization can follow two distinct pathways, known as the direct channel and the indirect channel^[36,152]. In the direct channel, polarization from the electrons is transferred directly to the ^{13}C nuclei ($e^- \rightarrow ^{13}\text{C}$). In the indirect channel, polarization is first transferred to the protons and then to the ^{13}C ($e^- \rightarrow ^1\text{H} \rightarrow ^{13}\text{C}$) (Figure 5.8b) by cross-relaxation.

To identify the direct pathway (direct channel)^[101], the thermal magnetization of ^{13}C must be suppressed at the start of the experiment using a saturation pulse train. Subsequently, during the build-up time of the ^{13}C magnetization, rotor-synchronized 180° pulses are applied on the proton channel. Then, a 90° detection pulse is applied on ^{13}C . During the acquisition, a decoupling routine is applied on the proton channel. (Figure 5.8a). The π pulses in this rotor-synchronized routine suppress the polarization transfer from the protons to the carbons. Therefore, direct polarization transfer from the electron spins to ^{13}C is solely responsible for boosting the signal intensity.

The determination of the indirect pathway (indirect channel) is not as straightforward. During microwave radiation, parts of the polarization from the electron spins is transferred to both protons and carbons. If the

rotor-synchronized routine is not utilized, the polarization on the protons will subsequently be transferred to the carbons via cross relaxation.^[36,152]

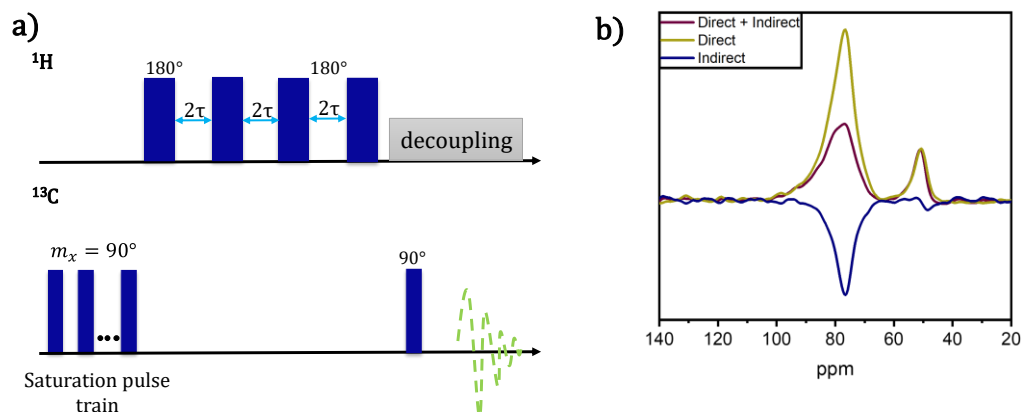


Figure 5.8. a) Pulse sequence to obtain the Direct pathway of the polarization, b) ^{13}C spectra with the 3 polarization pathways: blue line direct, pink one direct plus indirect, yellow line direct polarization.

6 Experimental Methods

This chapter outlines the experimental techniques and procedures employed for synthesis, characterization, as well as DSC and NMR analysis. The sections are organized in alignment with the structure of the results and discussions presented in Chapters 7 and 8.

6.1 Synthesis of the confinement materials

The synthesis of the porous materials and their initial characterization were conducted by Dr. Martin Brodrecht and Till Wissel in a parallel project at our laboratory in Darmstadt. The synthesis process for both materials was adapted from optimized protocols originally developed by Wang et al.^[153] and Zeidan et al.^[154] A brief description of the synthesis process and the pore characterization relevant to the present investigations will be provided, while more detailed information about the materials can be found in the original work.^[73]

6.1.1 Reagents

Pluronic® P123 ($M_n \sim 5800 \text{ g mol}^{-1}$) was acquired from Sigma-Aldrich, hydrochloric acid (37 wt %, HCl) and ethanol ($\geq 99.8 \%$, EtOH) were procured from Carl Roth, 3-aminopropyl triethoxysilane (98 %, APTES), was obtained from ABCR, tetraethyl ortho silicate (98 %, TEOS), was sourced from Acros. Ethylene glycol- d_4 (EG- d_4) with a deuteration degree of 98 % from Sigma Aldrich

It's noteworthy that all chemicals employed for material synthesis and experimentation were utilized without any prior purification steps.

6.1.2 Synthesis of Mesoporous Silica (SBA-15)

To a stirred solution of 44.5 g Pluronic® (0.008 mol, 1 equiv.), 44.5 g (0.214 mol, 1 equiv.) of TEOS were gradually added, whereby a white solid precipitated. The suspension was stirred for additional 24h, before it was transferred to a PTFE bottle. After aging at 90°C for 48 h under static conditions, the precipitate was separated from the supernatant solution by centrifugation and resuspended in deionized Water. The centrifugation and resuspension were repeated 5 times with water and 1 time with ethanol. After drying at 90°C, the residual template was eliminated by calcination at 650°C for 1 h. (heating rate 5 K/min). The resulting substance was freeze-dried, yielding 6.5 g of the desired product SBA- 15.

6.1.3 Synthesis of APTES Functionalized Mesoporous Silica (SBA-15 + APTES)

To a stirred solution of 44.5 g of Pluronic® (0.008 mol, 1 equiv.), 36.0 g of TEOS (0.173 mol, 0.8 equiv.) were gradually added. Once the addition was complete, the solution was stirred for 4 h. After this period, 9.6 g of APTES (0.043 mol, 0.2 equiv.) were added, and the mixture was stirred for additional 24 h. Following the agitation period, the suspension was transferred to a PTFE bottle and aged at 90°C for 48 h under static conditions. The precipitate was separated from the supernatant solution by centrifugation and resuspended in deionized water. This centrifugation and resuspension process was repeated 5 times with water and 1 time with ethanol. The template removal process involved a Soxhlet extraction with ethanol for 48 h immediately after the centrifugation procedure. The resulting product was freeze-dried, yielding 9.9 g of APTES-functionalized SBA-15.

6.2 Pore characterization of the Confinement Materials by Gas Adsorption Analysis

To determine pore size and specific surface area, gas adsorption analysis was conducted by Dr. Martin Brodrecht and Till Wissel, at 77 K using a Thermo Fisher Scientific Surfer Brunauer-Emmett-Teller (BET) analyzer, utilizing nitrogen as the adsorbent. The resulting adsorption-desorption isotherms are depicted in Figures 10.1 and 10.2 in the appendix. The specific surface area was calculated using the BET model within the relative pressure (p/p_0) range of 0.02 to 0.35. The pore volume was determined using the Gurvich method at $p/p_0 = 0.95$. The pore size distribution was assessed within the p/p_0 range of 0.01 to 0.95 using both the Barrett-Joyner-Halenda (BJH) method (Figure 10.2a) and for comparison with the non-local density functional theory (NLDFT) method with cylindrical silica pores as a calculation model (Figure 10.2b).^[155]

Table 6.1 highlights that the average pore diameter is similar for both pure SBA- 15 and APTES-functionalized SBA- 15, suggesting the suitability of pure SBA- 15 as a reference for confinement studies.

Table 6.1. Specific surface area (BET), pore volume (determined using Gurvich at p/p_0 0.95), and pore diameter (BJH) for each synthesized material. The average pore diameter is computed from the pore diameters acquired through the BJH and NLDFT approaches.^[156]

Sample	Specific surface area (S) [m ² g ⁻¹]	Pore volume (V) [cm ³ g ⁻¹]	Pore Diameter (d) [nm]		
			BJH	NLDFT	Average
SBA-15	714	0.89	5.7	7.0	6.4
SBA+APTES	537	0.72	5.5	7.9	6.7

The density of approximately 2.2 nm⁻² for the APTES linker in the functionalized SBA-15 was calculated according to Equation 6.1 using the results presented in Table 6.1 and additional elemental analysis data.

$$\text{Linker density [nm}^{-2}] = \frac{\text{Nitrogen content [mol}\cdot\text{g}^{-1}]}{\text{Specific surface area [m}^2\cdot\text{g}^{-1}]} \cdot N_A \quad (6.1)$$

where N_A is the Avogadro constant. As per the findings reported by Brodrecht et al.^[73] this density of linkers indicates that nearly half of the accessible silanol groups have been coated with APTES.

6.3 Filling of the Pores of the Silica Materials

Both silica materials were pre-treated under fine vacuum conditions (10⁻⁶ bar) at room temperature for 48 hours. Subsequently, they were transferred to an argon-filled glovebox to prevent atmospheric water adsorption. Under this inert environment, samples of APTES-functionalized SBA-15 and pure SBA-15 were mixed with EG-*d*₄ in proportions corresponding to their respective pore volumes. The pore volumes were determined using equations 6.2 and 6.3, based on data from table 6.1 for each material.

$$\text{SBA-15+APTES: } 20 \text{ mg} \cdot \frac{1 \text{ g}}{1000 \text{ mg}} \cdot \frac{0.72 \text{ mL}}{1 \text{ g}} \cdot \frac{1000 \mu\text{L}}{1 \text{ mL}} = 14.4 \mu\text{L of EG} - d_4 \quad (6.2)$$

$$\text{SBA-15: } 20 \text{ mg} \cdot \frac{1 \text{ g}}{1000 \text{ mg}} \cdot \frac{0.89 \text{ mL}}{1 \text{ g}} \cdot \frac{1000 \mu\text{L}}{1 \text{ mL}} = 17.8 \mu\text{L of EG} - d_4 \quad (6.3)$$

The samples containing EG-*d*₄ were left to absorb the guest molecules into the pores overnight. Both prepared samples were stored in the glovebox prior to their use in experiments.

6.4 Sample Packing

For DSC analysis, approximately 5 mg of each sample were packed into aluminum crucibles and hermetically sealed under inert conditions within the glovebox. For ²H ssNMR measurements, around 20 mg of the as-prepared solid samples were loaded into 3.2 mm sapphire rotors, sealed using a Teflon plug, and capped with a ZrO₂ drive cap. In the case of EG-*d*₄ in the bulk phase, 25 μL were added to the rotor, and a silicon plug was inserted to prevent sample leakage before sealing the rotor with a ZrO₂ drive cap.

6.5 Differential Scanning Calorimetry (DSC) measurements

Differential scanning calorimetry experiments were carried out using a NETZSCH 214 Polyma Heat Flux DSC instrument. The samples used in these measurements were prepared as described above and were tested within a temperature range of 100 to 300 K. Cooling and heating cycles were repeated three times. Various heating/cooling rates of 5 K/min, 7.5 K/min, 10 K/min, 15 K/min, 20 K/min, and 40 K/min were employed for the

experiments. DSC standards (zinc, indium, adamantane, caesium chloride, tin, and bismuth) were used for calibration for each heating/cooling rate. Nitrogen served as the purge and protective gas throughout the trials, and an empty sealed crucible was employed as a reference for baseline adjustment.

For further investigation, only the second cooling and heating cycles were utilized to eliminate potential impacts from the 'samples' thermal histories. It is noteworthy that data from the third cycle is in line with that from the second cycle, while variations are possible between the data from the first cycle.

6.6 Variable Temperature ^2H solid-state NMR (^2H ssNMR)

All variable temperature ^2H ssNMR experiments were conducted using a Bruker Avance III 400 MHz DNP NMR spectrometer equipped with a 9.4 T Ascend sweepable magnet system, corresponding to a ^2H frequency of 61.65 MHz. A 3.2 mm triple resonance $^1\text{H}/\text{X}/\text{Y}$ low-temperature MAS probe was utilized. The sample temperature was controlled using a Bruker BioSpin low-temperature MAS cooling system. Spectra were collected within the temperature range of 120 to 260 K. A waiting period of 20 minutes was used to allow the sample to reach thermal equilibrium at each temperature before conducting the experiment.

To ensure that the experiments were conducted at the specified temperature, we calibrated this parameter using the methodology outlined by Thurber & Tycko.^[157] The temperature readings were obtained from a thermocouple positioned in proximity to the sample for both the calibration data and the subsequent experiments. More detailed information can be found in Section 10.2 of the appendix

6.6.1 Deuterium MAS Experiments: One Pulse Sequence

^2H MAS NMR spectra were collected using a single pulse sequence at a spinning rate of 8 kHz. All experiments utilized a 2 μs excitation pulse, which corresponds to an approximate flip angle of 30° at 120 K. The recycle delay was set to 15 s, and each spectrum was acquired with 128 s'ans. It's worth noting that pulse optimization was conducted using bulk EG- d_4 at 120 K.

Fitting of the ^2H MAS spectra was executed using the dmfit 2015 software package.^[158] For spectrum shaping, a hybrid approach combining the Quad 1st model and the Gaussian/Lorentzian model was employed.

6.6.2 ^2H Static Experiments employing the Solid Echo Sequence

In this pulse sequence described in the section 4.7, a pulse spacing of 40 μs and 2 μs pulse length were used. The recycle delay was set again to 15 s, and each spectrum was captured with 1024 scans. For spectral fitting, a custom Matlab program described in reference^[159] was utilized.

6.6.3 T_1 and T_2 Experiments under MAS

In order to determine the relaxation times (T_1 and T_2) for sample **2**, the pulse sequences described in detail in section 4.8 were used.

To determine T_1 times of the ^2H under MAS at varying temperatures, a saturation-recovery pulse sequence was employed. This sequence involved a saturation pulse train with twenty pulses of 2 μs length and 200 μs spacing, followed by a 2 μs detection pulse. For each data point, 12 accumulations were conducted.

For T_2 experiments on ^2H under MAS, a rotor-synchronized echo sequence described more in detail in chapter 4., was used. Pulse lengths of 2 μs and 4 μs were employed in this sequence, where the 2 μs pulse corresponded to a flip angle of around 30° at 120 K. Spectra were recorded with 8 kHz spinning, and the echo spacing was adjusted between 1 and 8 rotor periods. A repetition delay of 15 seconds was maintained for each spectrum.

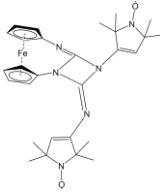
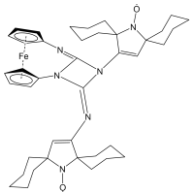
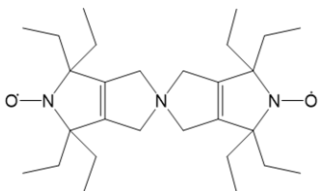
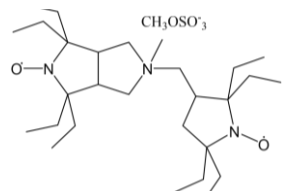
6.7 Radicals

The radicals, the results of which are reported in Chapter 8, were synthesized and characterized by the research group led by Professor Bagryanskaya in Novosibirsk, Russia. The EPR analysis, as well as the simulation and optimization of the structure of the radicals, were also carried out by the same group. For more detail information the reader can look the references. ^{[73,73][144,160]}

6.7.1 Sample Preparation

Each of the radicals' solutions was prepared at a concentration of 15 mM. The specific solvent utilized for each radical is indicated in table 6.2. Around 25 μL of each solution was carefully introduced into 3.2 mm sapphire rotors. These rotors were securely sealed using a silicon plug to prevent leakage and were then closed with a ZrO_2 drive cap.

Table 6.2. Solvents used as matrices for the specific radicals.

Code	Radical Structure	Solvent (matrix)
1		Tetrachloroethane (TCE)
2		Tetrachloroethane (TCE)
3		60 %v/v of glycerol-d ₈ , 30 %v/v D ₂ O and 10 %v/v H ₂ O
4		60 %v/v of glycerol-d ₈ , 30 %v/v D ₂ O and 10 %v/v H ₂ O

6.7.2 Solid-state DNP Experiments

All experiments involving solid-state dynamic nuclear polarization (DNP) were conducted on a Bruker Avance III 400 MHz NMR spectrometer equipped with an Ascend 400 sweepable DNP magnet and a special 3.2 mm triple resonance ¹H/X/Y low-temperature magic angle spinning (MAS) probe. Microwave irradiation (μW) at 263 GHz was provided by a 9.7 T Bruker gyrotron system. The spectra, including ¹H MAS, ¹H→¹³C cross polarization MAS (CPMAS), and ¹³C MAS, were acquired with spinning at a rate of 8 kHz.

6.7.2.1 ¹H MAS and ¹H MAS Saturation Recovery experiments

For ¹H MAS NMR spectra, a pulse sequence with background suppression^[161] was employed, accumulating 16 scans with a relaxation delay of 4 s.

A saturation-recovery pulse sequence was used to acquire build-up curves for ^1H signals with microwave irradiation (μW_{ON}) and to calculate the built-up time $T_{\text{B}} \text{ } ^1\text{H}$. A pulse train of twenty 90° pulses, each lasting $2.3 \mu\text{s}$ with $200 \mu\text{s}$ spacing, was applied, followed by a 90° detection pulse. For each data point, 16 accumulations were conducted.

6.7.2.2 Cross Polarization

In the case of $^1\text{H} \rightarrow ^{13}\text{C}$ CPMAS measurements, 128 scans were performed with a recycle delay of 1.3 times the built-up time of protons ($T_{\text{B}} \text{ } ^1\text{H}$). A contact time of 2 ms was chosen for these experiments, and high-power proton decoupling was applied during data acquisition using the spinal 64 sequence.^[162]

6.7.2.3 ^{13}C MAS Direct and Indirect Polarization

^{13}C MAS spectra were acquired using the pulse sequence described in detail in section 5.8. Spectra for all radicals were obtained using this sequence with both microwave irradiation (μW_{ON}) and without (μW_{OFF}) as well as with and without π pulses. High-power proton decoupling was implemented using the spinal 64 sequence during data collection.^[163]

6.7.3 Enhancement calculation (ϵ)

To evaluate the enhancement of NMR signals due to the effect of DNP, the areas of the signal peaks on the spectra obtained after recording different experiments under microwave radiation are divided by the corresponding signal peak areas obtained without microwave radiation

The calculation of the enhancement of the indirect pathway requires an additional step before the areas can be subtracted. Since the indirect pathway cannot be directly obtained, it is calculated by subtracting the intensity of the spectra obtained from the experiment with π pulses from the intensity of the experiment without pulses. The remaining intensity can now be plotted against the frequency. This previous step has to be done for the experiments with and without microwaves. Afterwards the areas of the signal peaks obtained during the μW_{ON} experiments can be divided by the corresponding signal peak areas of the experiments with μW_{OFF} .

7 Influence of APTES Decorated SBA-15 on the Dynamics of Confined Ethylene Glycol

The results of this chapter have extensibly published in^[164]

7.1 Introduction

Mesoporous silica materials have gained significant attention in recent decades due to their distinct properties, including high thermal stability, substantial surface area, lack of toxicity, and widespread availability. These characteristics render them suitable for a wide range of applications, such as ion exchange, molecular sieving, adsorption, optics, catalysis, bioengineering, energy storage, and drug delivery systems.^[4–9,64] One notable feature of mesoporous silica materials is their tuneable pore size, usually between 2 and 50 nm, resulting in a considerable specific inner surface area.^[9,62,63]

For its applications, it is often essential to modify the pore surfaces of the silica materials. This is done for example by covalently attaching organic molecules to the silanol groups on the silica pore walls.^[15–17] Such modifications alter surface hydrophilicity and consequently the chemical interactions with molecules within the pores.^[71–76] The arrangement and behavior of molecules close to the pore walls are influenced by the wall's geometry and chemistry, leading to changes in the mobility of these molecules. This mobility variation in turn impacts thermodynamic processes like melting, freezing, adsorption, and desorption.^[7,77,78] This phenomenon, known as confinement effect, has been extensively explored, particularly for water and small organic molecules within porous silica.^[87–91]

In this context, 3-aminopropyl triethoxysilane (APTES) is a commonly utilized agent to modify silica surfaces. The presence of a terminal amino group ($-NH_2$) enables the attachment or “linking” of molecules of interest to the pore walls. APTES can be incorporated into silica materials through two main methods: grafting after the mesoporous material synthesis or co-condensation during the material's synthesis.^[79]

Recently, the study of molecular dynamics under confinement has gained prominence, with ethylene glycol (EG) and its derivatives being relevant subjects for such investigations.^[165–167] This solvent, commonly used in industry, possesses favourable attributes such as low toxicity, non-volatility, high abundance, and renewable sourcing from biomass.^[21–24] Studying EG's structural arrangement within confined spaces, like modified porous silica, is challenging due to its complex behaviour including glassy and crystalline phases.^[99]

To explore the influence of the confinement in general and the APTES modification of the confining material on the structure and dynamics of ethylene glycol, DSC and solid-state NMR is employed. DSC offers valuable insights into physico-chemical processes,^[25–28] while solid-state NMR can provide insights into the general dynamics of the molecules.^[77,168] Understanding these dynamics is facilitated by extracting NMR parameters encoded in the

line shape of spectra acquired at various temperatures. For instance, utilizing quadrupolar nuclei like deuterium enables the analysis of intramolecular motions by exploring the alterations of the ^2H ssNMR line shapes created by the quadrupolar interactions.^[31,32,169]

As deuterium containing guest molecule, partially deuterated ethylene glycol (EG- d_4) has been chosen, leaving the hydroxyl groups protonated to prevent a deuterium-hydrogen exchange with silanol groups of the surface or the APTES linker, since such exchange could complicate the analysis. The study focuses on three scenarios: EG- d_4 in its bulk form (sample **1**), EG- d_4 confined within pure SBA- 15 (sample **2**), and EG- d_4 confined within APTES-modified SBA- 15 (sample **3**).

7.2 Results

7.2.1 Analysis of the Phase Behavior by DSC

The DSC curves at different scan rates (5, 7.5, 10, 15, 20, and 40 K/min) are depicted in Figures 7.1-7.3 for each individual sample. Figure 7.1 illustrates the results for bulk ethylene glycol (sample **1**), where all cooling graphs exhibit an exothermic characteristic ("loop") near 230 K. This phenomenon arises as an instrumental artifact when the latent heat of the phase transition is released faster than the instrument can compensate, leading to an artificially higher temperature than the intended value based on the selected cooling rate.^[170] As a consequence, a loop shape appears instead of a conventional negative peak on the cooling curve. In the heating plots for sample **1**, a solitary endothermic peak is observable. The starting temperature is roughly ~ 264 K, closely resembling the established melting temperature of bulk ethylene glycol (261.6 K).^[101] Due to the broader nature of the DSC peaks compared to the anticipated sharp freezing point minimum^[171], no endeavours were made to execute a Gibbs-Thomson analysis.

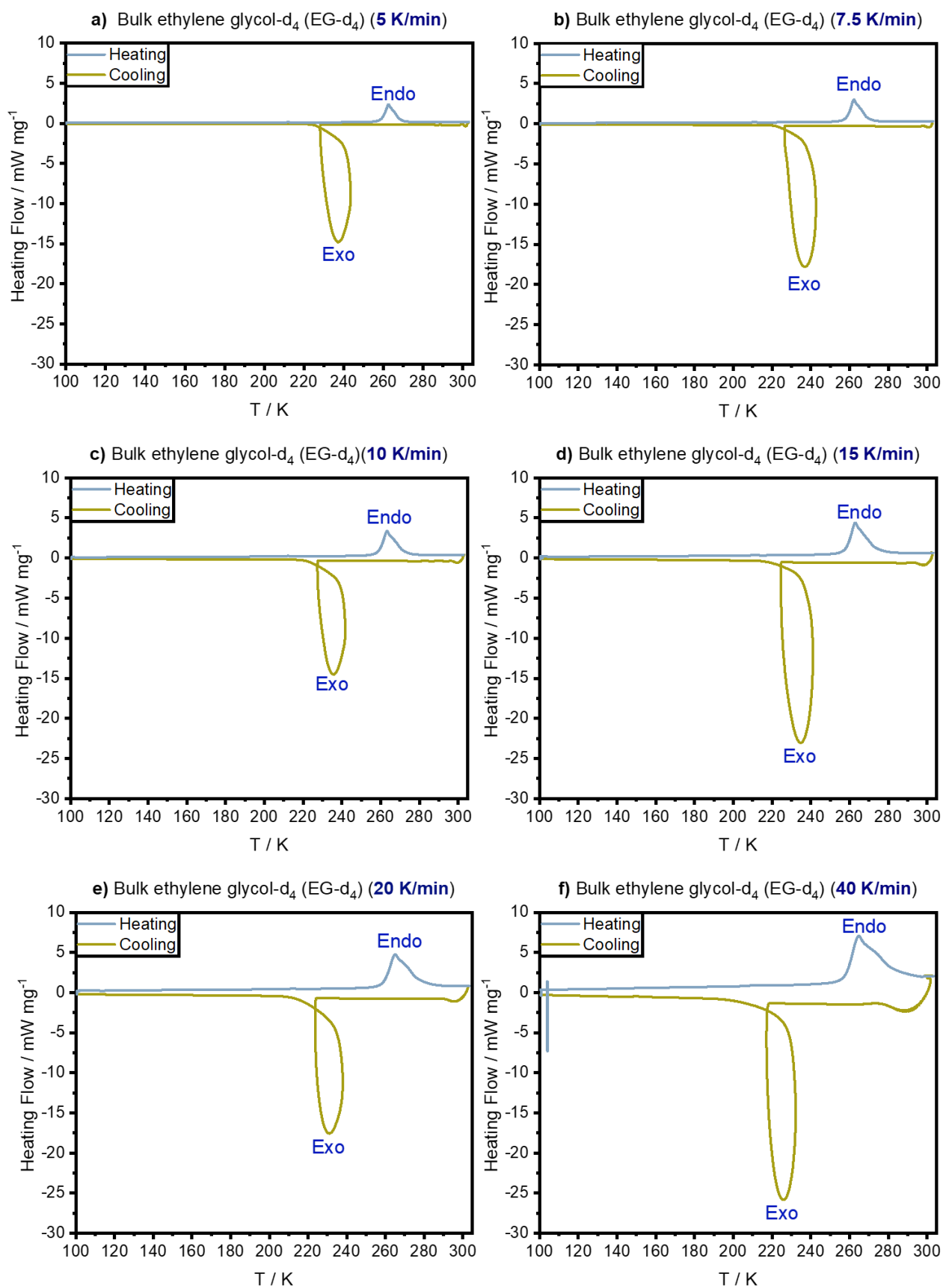


Figure 7.1. Experimental DSC curves of bulk EG- d₄ (sample 1) at six different heating/cooling rates: 5 K/min, 7.5 K/min, 10 K/min, 15 K/min, 20 K/min, and 40 K/min. Exo labels the exothermic crystallization peak and Endo indicates the endothermic melting peak. Picture adapted from^[164].

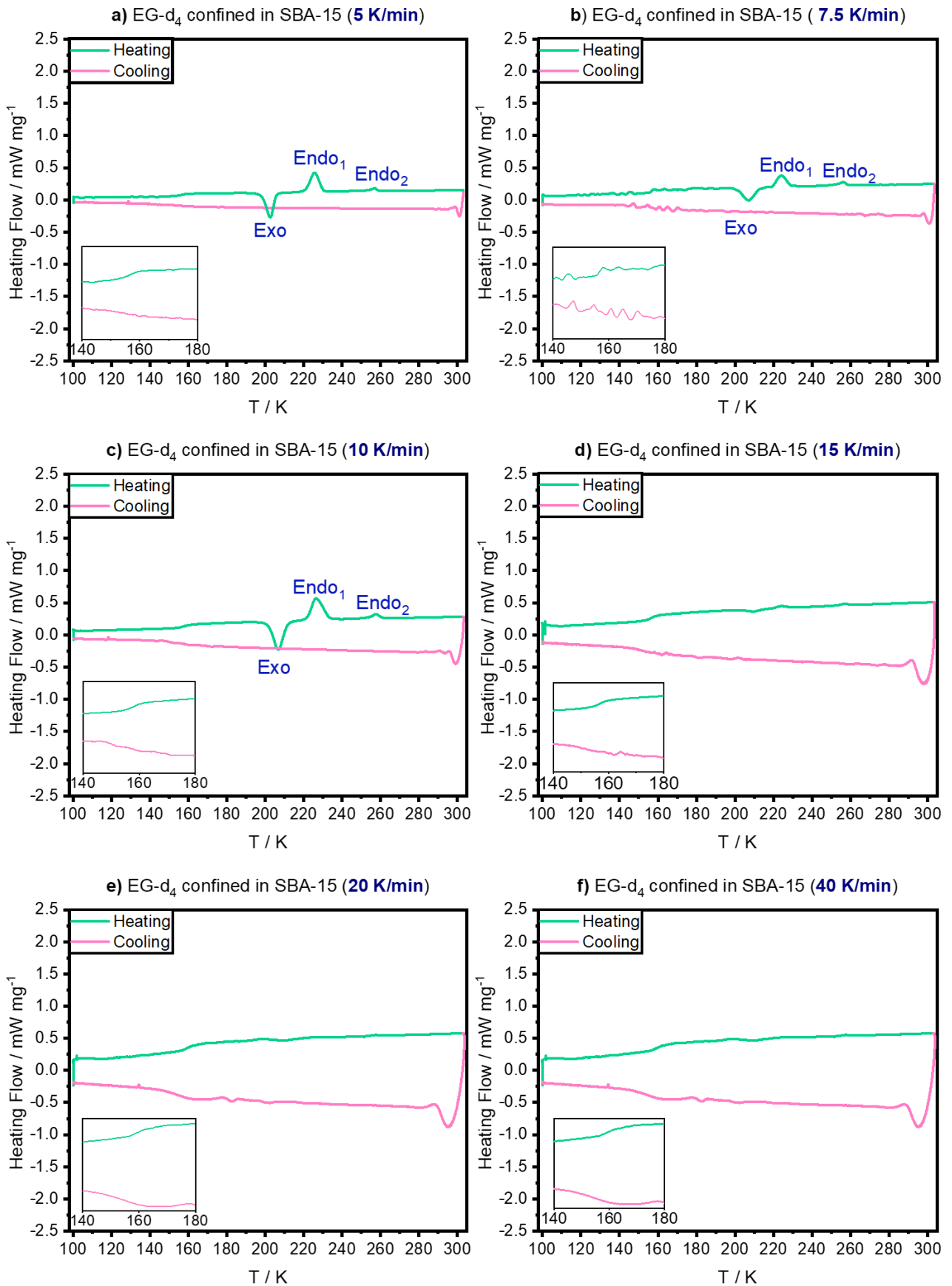


Figure 7.2. Experimental DSC curves of EG- d₄ confined in SBA- 15 (sample 2) at six different heating/cooling rates: 5 K/min, 7.5 K/min, 10 K/min, 15 K/min, 20 K/min, and 40 K/min. Exo labels the exothermic crystallization peak and Endo₁ and Endo₂ indicate endothermic melting peaks. The inserts display expanded temperature regions where a glass transition is indicated. Picture adapted from^[164].

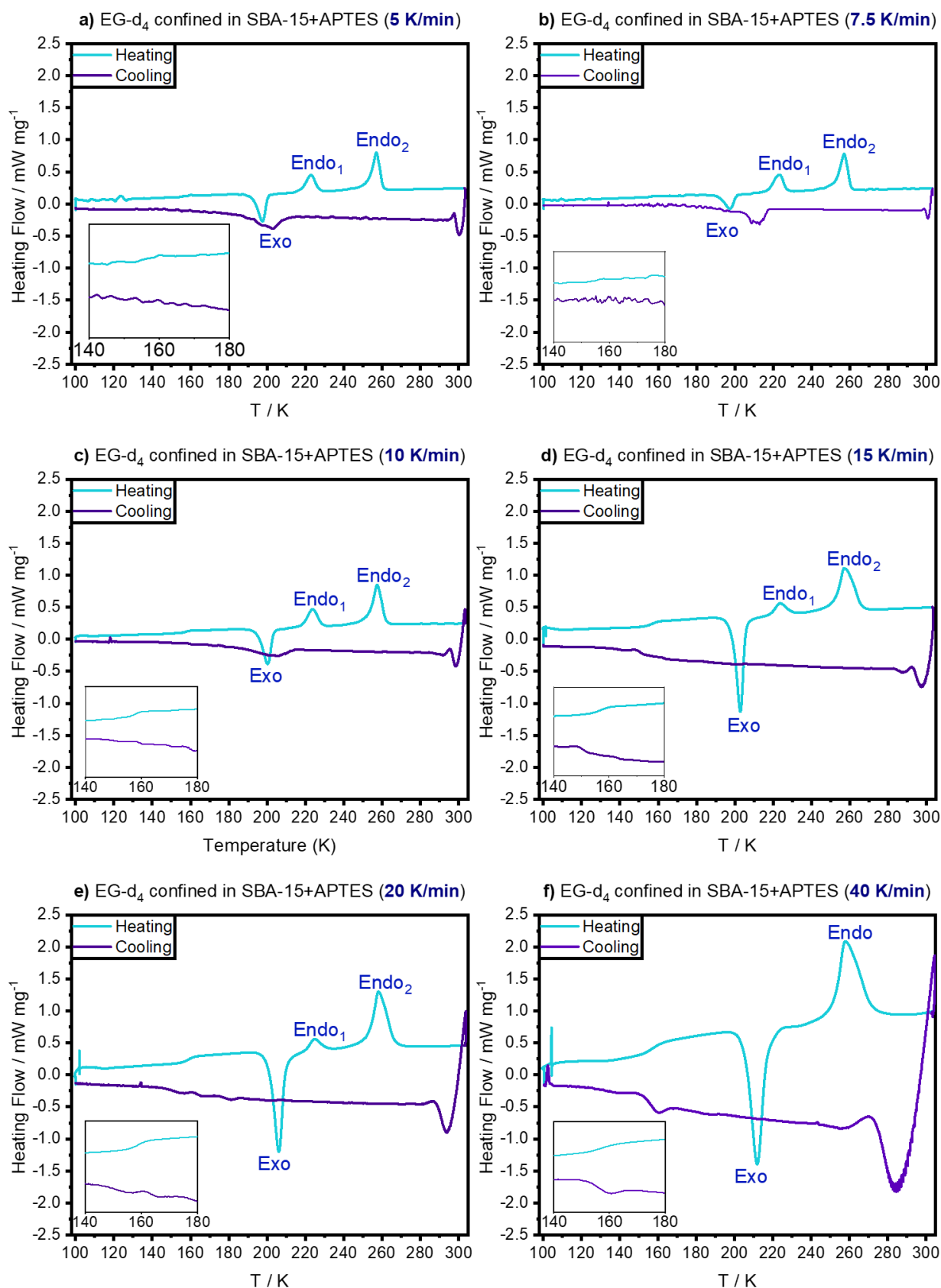


Figure 7.3. Experimental DSC curves of EG- d₄ confined in SBA- 15+ APTES (sample 3) at six different heating/cooling rates: 5 K/min, 7.5 K/min, 10 K/min, 15 K/min, 20 K/min, and 40 K/min. Exo labels the exothermic crystallization peak and Endo₁ and Endo₂ indicate endothermic melting peaks. The inserts display expanded temperature regions where a glass transition is indicated. Picture adapted from^[164].

Figures 7.2 and 7.3 present the DSC findings regarding the confinement of EG- d₄ within the porous silica materials. When considering EG- d₄ confined within pure SBA- 15 (Figure 7.2), the cooling curves do not show crystallization events anymore. Instead, crystallization appears during heating, at 200 K, for heating rates between 5 K/min and 10 K/min. This crystallization is followed by two melting events, around 220 K and 260 K.

For larger heating rates, crystallization events are completely absent. Instead, both cooling and heating curves exhibit a subtle step-like characteristic near 155 K, which becomes more apparent within the inserted sections corresponding to each heating/cooling rate. This feature signifies the formation of a glass phase below 155 K.

A crystallization event during heating is a typical fingerprint for a supercooled state. In this state, the molecules exhibit slowed reorientation motions, adopting configurations where the latent heat is not released. Furthermore, due to the dependency on the cooling rate, it is reasonable to assume a kinetic hindering of the phase formation. The interaction of EG- d₄ with the neat silica pore walls enlarges the time constants of the EG- d₄ but does not prevent crystallization as a whole.

Provided the basic pathway of the above interpretation is correct, weakening the interaction forces between EG- d₄ and the pore walls, for example, by modifying the pore wall surfaces with APTES, crystallization events at high cooling rates are expected. The DSC curves for EG- d₄ confined in SBA 15 + APTES, depicted in Fig. 7.3, do show crystallization events even at high cooling and heating rates indeed. Furthermore, crystallization events during cooling are seen for lower cooling rates in the cooling curve. However, crystallization seems to be only partial, as indicated by crystallization events during heating. Increasing the cooling rate above 10 K/min prevents crystallization during cooling; however, it preserves crystallization during heating.

This observed behavior of EG- d₄ is therefore consistent with the assumption of kinetic hindering of phase transitions by an interaction between EG-d₄ and the pore walls

7.2.2 EG-d₄ Dynamics by Variable Temperature ²H Solid-State NMR

Figures 7.4-7.6 present a selection of ²H solid-state NMR spectra measured at different temperatures within a range where detectable shifts in the spectral line shape can be observed. These measurements were performed under both static and MAS conditions. Additionally, the corresponding simulated spectra for the three investigated systems are provided. It is crucial to note that OH groups of EG- d₄ are non-deuterated, and consequently not contributing to the ²H NMR signals.

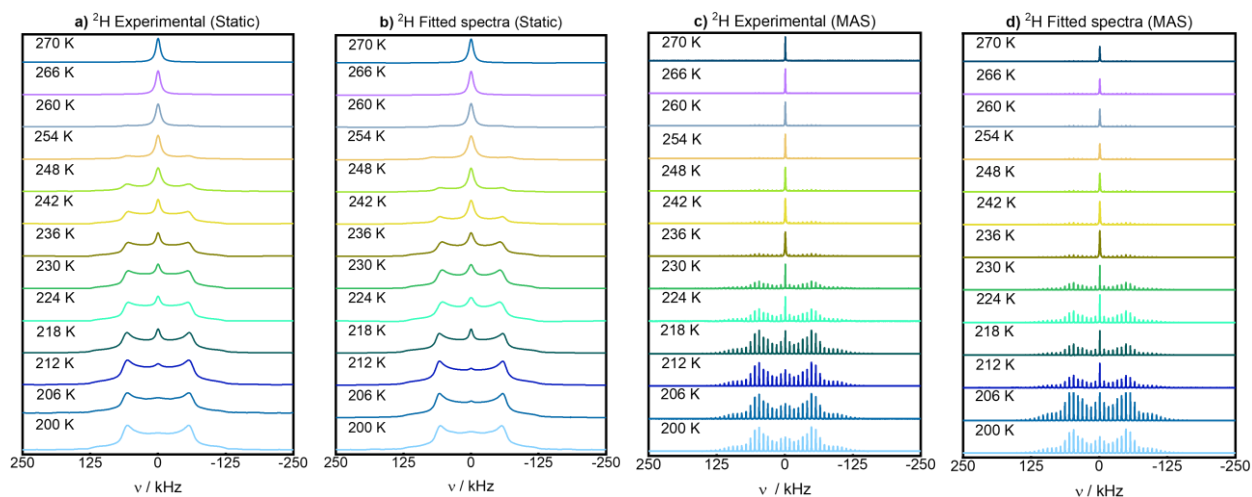


Figure 7.4. ^2H ssNMR spectra obtained in the temperature range between 200 and 270 K for EG- d_4 in the bulk phase (sample 1). a) ^2H static experimental data, b) fitted ^2H static NMR spectra c) ^2H MAS experimental data, and d) fitted ^2H MAS spectra. Picture adapted from^[164].

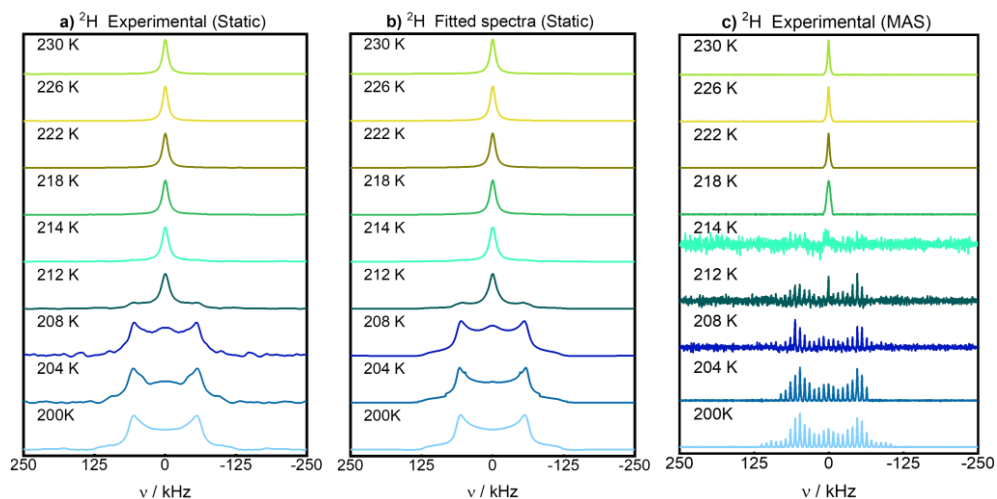


Figure 7.5. ^2H ssNMR spectra obtained in the temperature range between 200 and 230 K for EG- d_4 in SBA- 15 (sample 2). a) ^2H static NMR experimental data, b) fitted ^2H static NMR spectra, c) ^2H MAS experimental data. Picture adapted from^[164].

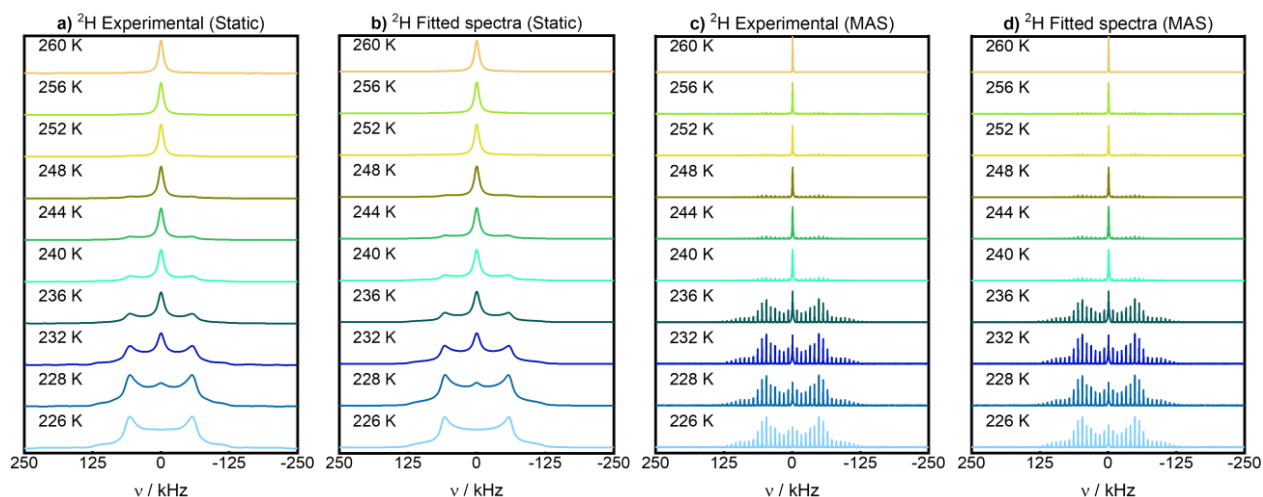


Figure 7.6. ^2H ssNMR spectra obtained in the temperature range between 226 and 260 K for EG- d_4 in SBA- 15 + APTES (sample **3**). a) ^2H static experimental data, b) fitted ^2H static NMR spectra c) ^2H MAS experimental data, and d) fitted ^2H MAS spectra. Picture adapted from^[164].

The spectra of the static experiments presented in Figs. 7.4-7.6 exhibit two primary features: a dominant Pake pattern at lower temperatures and a prevailing Lorentzian line at higher temperatures. The temperature range within which the spectra transition from being Pake-pattern dominated to Lorentzian-line dominated varies across the different samples. Specifically, for sample **1** (Fig. 7.4), the transition occurs between 200 and 270 K; for sample **2** (Fig. 7.5), it happens within 200 to 230 K; and for sample **3** (Fig. 7.6), the transition range lies between 226 and 260 K. Notably, the shape of the Pake pattern and the Lorentzian line remains largely unchanged in these spectra, with only their intensities showing variation.

However, in the MAS spectra of sample **2**, a distorted line shape or even a complete loss of signal is observed in the temperature range between 214 K and 216 K. This behavior is attributed to the stronger influence of relaxation on the MAS spectra compared to spectra acquired under static conditions. The reason for this lies in the timing of signal detection: static experiments detect the echo at a time of 104 μs , whereas the first rotational echo appears after one rotor period of 125 μs in MAS spectra. Additionally, achieving resolved spinning sidebands in the case of MAS requires the presence of multiple rotational echoes, which is limited by fast relaxation. Consequently, only the static spectra were fitted and presented for sample **2**, as shown in Figure 7.5. A thorough analysis of the spectral changes depicted in Figures 7.4-7.6 is provided in the discussion in chapter 7.3.

Given the distinct signal loss observed in sample **2** at specific temperatures, relaxation experiments under MAS conditions were exclusively carried out for this particular sample. The outcomes of these experiments are presented in Figure 7.7. The correlation times deduced from these experiments imply rapid dynamics within the system. In the realm of ^2H NMR, rapid dynamics typically correspond to correlation times less than 10^{-7} s, whereas correlation times surpassing 10^{-5} s indicate sluggish dynamics. It is only within the intermediate range

of correlation times, spanning from 10^{-5} to 10^{-7} s, that the determination of the motional process type through line shape analysis becomes feasible.^[172]

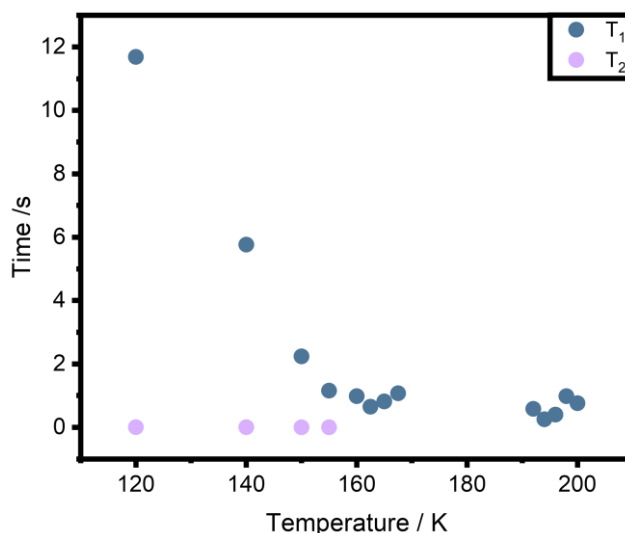


Figure 7.7. Relaxation times for EG- d_4 confined in SBA- 15 (sample 2) obtained at different temperatures in the range between 120 and 226 K. T_2 values are in the range of ms.

T_1 and T_2 experiments were conducted under MAS, as depicted in Figure 7.7, revealing a complete signal loss within the temperature range of 204 to 214 K (see Figure 7.7). This observation suggests that, during these temperatures, dynamics occur on a timescale shorter than 10^{-7} s, which falls beyond the detectable scope of solid-state NMR under the employed MAS conditions.

Continuing with the analysis of the three systems, a detailed examination of the changes in the spectral patterns shown in Figures 7.4-7.6 is displayed in Figure 7.8. This diagram presents the ratios of the solid-like (Pake pattern) and the liquid-like (Lorentzian line) constituents for the three systems under investigation, plotted as function of the temperature. In case of EG- d_4 in the bulk phase (depicted in Figure 7.8a), a gradual shift is evident across temperatures ranging from 208 to 240 K, followed by a more rapid transition from 240 K to 266 K. When EG- d_4 is confined within SBA- 15 (as illustrated in Figure 7.8b), a clear and abrupt shift arises at 210 K, encompassing a mere 10 K range. In contrast, for EG- d_4 confined within SBA- 15 + APTES (as shown in Figure 7.8c), a smoother transition becomes observable, initiated around 220 K and completed near 256 K. The variations noticed among the three analyzed systems are assigned to interactions of EG- d_4 molecules with their surroundings. Further elucidation of our discoveries is given in the discussion in the following chapter.

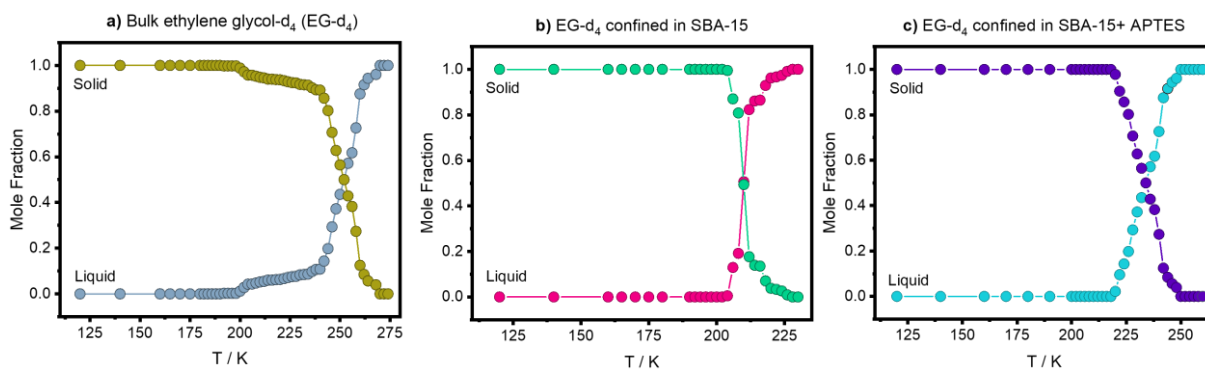


Figure 7.8. Change of fractions of the liquid-like and solid-like components during the phase transition, plot as a function of temperature. The data points correspond to the relative areas of the liquid-like Lorentzian signal and the solid-like Pake pattern from the ^2H NMR spectra measured under static conditions. a) EG- d_4 in the bulk phase (sample **1**), b) EG- d_4 confined in SBA- 15 (sample **2**), and c) EG- d_4 confined in SBA- 15+APTES (sample **3**). Figure adapted from reference^[164]

7.3 Discussion

When comparing DSC and ssNMR results, one must bear in mind that each technique follows a) different temperature profiles and b) probes different scales. The DSC runs closed temperature circles at constant speeds. The ssNMR settles at one particular temperature for the time that is needed for one Spectrum with adequate signal to noise ratio, that is for hours in case of static conditions. Provided the supercooled state is established due to interactions with the pore walls, the molecules may arrange into a crystallite state on the timescale of the NMR experiment. Such a relaxation into a crystallite state maybe driven by the “interaction gradient” from the pore center to the pore wall. In particular, the molecules nearest the pore wall are hindered to arrange them self into crystal order, due interaction with the pore walls. The layer next to this layer is likewise hindered, however, the potential wall is lower, compared to the pore layer, and so on. So, we may have a rearrangement from a supercooled, glassy state into a crystallite state during the time necessary to record the NMR spectrum. Now, the question arises whether such a rearrangement must be seen in the NMR spectrum. Here, b) must be considered. NMR probes the mobility of a molecule on a local scale, that is the averaging out of the EFG of a C- D bond. The Pake pattern seen in the spectra are the result of a randomly oriented symmetry axis of the corresponding EFG tensor, with respect to the laboratory frame. Reorientation into randomly orientated multi crystallites can hardly be done when the probed interaction is on a local scale. The ssNMR is therefore able to probe the dynamics of the molecules within the pore walls, but not to probe a slow rearrangement from glassy into multi crystallite powders.

In conclusion, the ssNMR versus temperature dynamics may not show crystallization events at temperatures seen in the DSC heating curves, namely the pronounced crystallization peaks. However, melting events should be seen in a temperature regime where melting events appear in the DSC curves.

The lack of a distinct step-like pattern in the DSC cooling and heating curves, as depicted in Figure 7.1 for sample **1**, indicates the absence of glass formation in the sample. Instead, the observed exothermic and endothermic

signals imply a process of freezing into a crystalline solid, succeeded by subsequent melting. It is important to highlight that neat ethylene glycol has been recognized as an organic glass-former undergoing structural relaxation processes below its glass transition temperature.^[99] This results in a complex coexistence of glassy and crystalline phases, which might explain the broader temperature range across which the ssNMR spectral changes manifest in Figure 7.4 for sample **1**. This range contrasts with the temperature span of exo- and endothermic characteristics observed in Figure 7.1.

In addition, it should be noted that ssNMR is sensitive to motional disturbances, which may occur at temperatures much lower than the phase transition temperature^[95] Notably, the reproducibility of ssNMR spectra in Figures 7.4-7.6 is consistent, whether acquired during sample cooling or heating (refer to Appendix 10.2).

Concerning sample **3** illustrated in Figure 7.6, the temperature range where ssNMR spectral changes occur aligns well with the range during which the two endothermic peaks are obtained in the heating curves of sample **3** as shown in Figure 7.3. However, it is important to mention that the ssNMR spectral changes depict a gradual transition, in contrast to the distinct step-like alterations observed in the separate endothermic peaks in Fig 7.3.

Moving on to sample **2**, the ssNMR spectral changes (depicted in Figure 7.5), appear to be complete at 230 K, covering a narrower temperature range compared to samples **1** and **3** (Figures 7.4 and 7.6). Nonetheless, the endothermic peak referred to as "Endo₂" is only faintly evident in Figs 7.2a-c. It is plausible that the proportion of molecules associated with this specific phase transition might have been insufficient to detect substantial motion changes within the ssNMR spectrum. Remarkably, the temperature of 230 K aligns well with the culmination of the phase transition linked to the endothermic peak labelled with "Endo₁" in Fig 7.2.

To shed light on the molecular dynamics within the three studied systems, the quadrupolar coupling constants (C_Q) obtained from simulations of line shapes in both static and MAS spectra were graphed against temperature in Figure 7.9. It's important to note that C_Q functions as a sensitive indicator, making it easier to observe alterations in nuclear positions and their immediate environments.

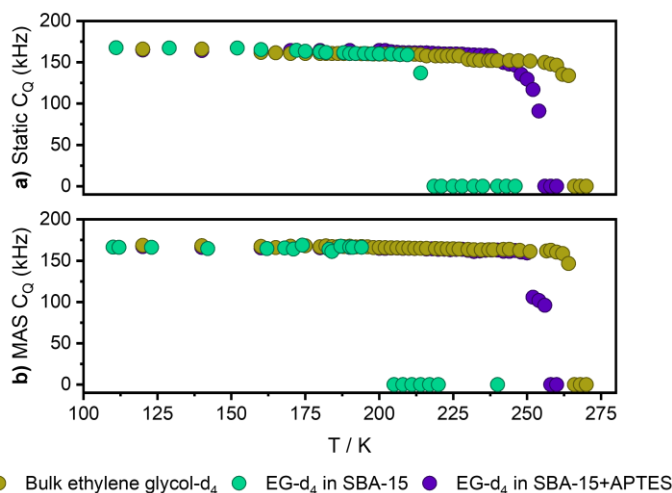


Figure 7.9. Values of the quadrupolar coupling constants (C_Q) extracted from the simulated spectra as function of the temperature: a) ^2H static NMR spectra, and b) ^2H MAS spectra. Picture adapted from^[164].

In Figure 7.9, it is observed that at low temperatures, both in MAS and static spectra, all three samples exhibit a maximum value of C_Q around 168 kHz, which is characteristic of rigid or slow-moving C-D bonds. At these low temperatures, EG- d_4 experiences very slow motions, keeping the spectral line shape similar across all three samples. However, as the molecules become more mobile, leading to motional averaging, there is a decrease in the time-averaged quadrupolar interaction, resulting in a reduction in C_Q .

The uniform and temperature-independent Pake pattern observed in all three samples strongly indicates that the deuterium nuclei experience a consistent electric field gradient, whether ethylene glycol is in a solid state, confined within pores, or not. Based solely on the ssNMR data, two possibilities cannot be distinguished: (a) all three samples exist exclusively in a crystalline solid state, or (b) the electric field gradient experienced by $-\text{CD}_2-$ deuterium atoms remain constant, irrespective of whether the solid phase is crystalline or amorphous (glassy). The absence of hysteresis effects in the ssNMR data (cooling vs. heating, shown in the section 10.3) implies that the samples were in thermodynamic equilibrium, likely in the crystalline phase, supporting scenario (a). Nevertheless, even at the slowest scan rate of 5 K/min, the DSC data for sample **2** in Figure 7.2 suggest the formation of a glassy phase, indicating scenario (b). This interpretation is further substantiated by T_2 relaxation data for sample **2** shown in Figure 7.7b, which also explains the exothermic peak in the heating curve of sample **2** in Figure 7.2. This suggests that sample **2** underwent a transition from a glassy to a crystalline solid, which was not reflected in the ssNMR spectra in Figure 7.4, as they consistently displayed the same Pake pattern at temperatures below 200 K.

The heating curves for confined ethylene glycol in Figures 7.2 and 7.3 exhibit two endothermic peaks, aligning with the findings reported by Reuhl et al.^[167] for ethylene glycol confined in silica pores of varying sizes. In their study, DSC samples comprised silica pore material saturated with an excess of ethylene glycol. They attributed the Endo_2 peak to the melting of surplus ethylene glycol outside the pores, and its temperature aligns well with

the endothermic peak in sample **1** at around 265 K. The Endo₁ peak is associated with the presence of a liquid phase within the pores, a conclusion supported by T₁ relaxation and NMR self-diffusion measurements conducted by them. These observations correlate with the ssNMR spectra in Figures 7.5 and 7.6, where a spectral component with a Lorentzian shape indicates that certain segments of the ethylene glycol molecule can move freely. While it is possible that not all ethylene glycol is inside the pores in samples **2** and **3**, this alone cannot explain the substantial Endo₂ peak in Figure 7.3 for sample **3**, where it surpasses the Endo₁ peak. Therefore, considering the coexistence of solid and liquid ethylene glycol inside the pores, it is likely that a portion of confined ethylene glycol at the pore center remains in a solid state at low temperatures. Though this location does not completely eliminate the influence of the pore walls on the confined molecules, it prevents EG-d₄ in that position from adopting a glassy structure at low temperatures. Under these assumptions, it is more plausible that the Endo₁ peak results from the melting of a fraction of confined ethylene glycol within the pore near to the pore walls, while the Endo₂ peak is largely or entirely due to the melting of the remaining solid ethylene glycol in the core of the pore.

Comparing sample **2** to sample **3**, the APTES (3-aminopropyltriethoxysilane) surface modification in sample **3** results in a significantly larger portion of ethylene glycol remaining solid within the pore after the initial melting event when heated, as depicted in Figure 7.10. This effect of APTES can be explained by the intermolecular interactions between ethylene glycol and the pore surface. The silanol surface is expected to have stronger interactions with ethylene glycol compared to the APTES-decorated surface due to differences in polarity and hydrogen bonding capabilities.^[173] These strong interactions with the pore surface slow down ethylene glycol dynamics^[167] weakening intermolecular forces between ethylene glycol molecules. Consequently, the tendency of EG- d₄ to form a crystalline solid is reduced. Conversely, stronger interactions with the pore surface relative to neighboring molecules allow for the breakdown of the crystalline structure at lower temperatures compared to the bulk. Therefore, ethylene glycol molecules near the pore surface melt first upon heating, while those farther away behave similarly to bulk ethylene glycol and remain solid until reaching the bulk melting temperature. In sample **2**, without APTES surface modification, the fraction of ethylene glycol molecules remaining solid is relatively small (Figure 7.10a), whereas in sample **3**, with the APTES modification and a similar average pore size, this fraction is much larger because the weaker interactions of ethylene glycol with APTES affect fewer layers of ethylene glycol molecules adjacent to the pore surface (Figure 7.10b). This interpretation is supported by the absence of the Endo₁ peak for silica materials with very small average pore sizes, as reported by Reuhl et al.^[167]

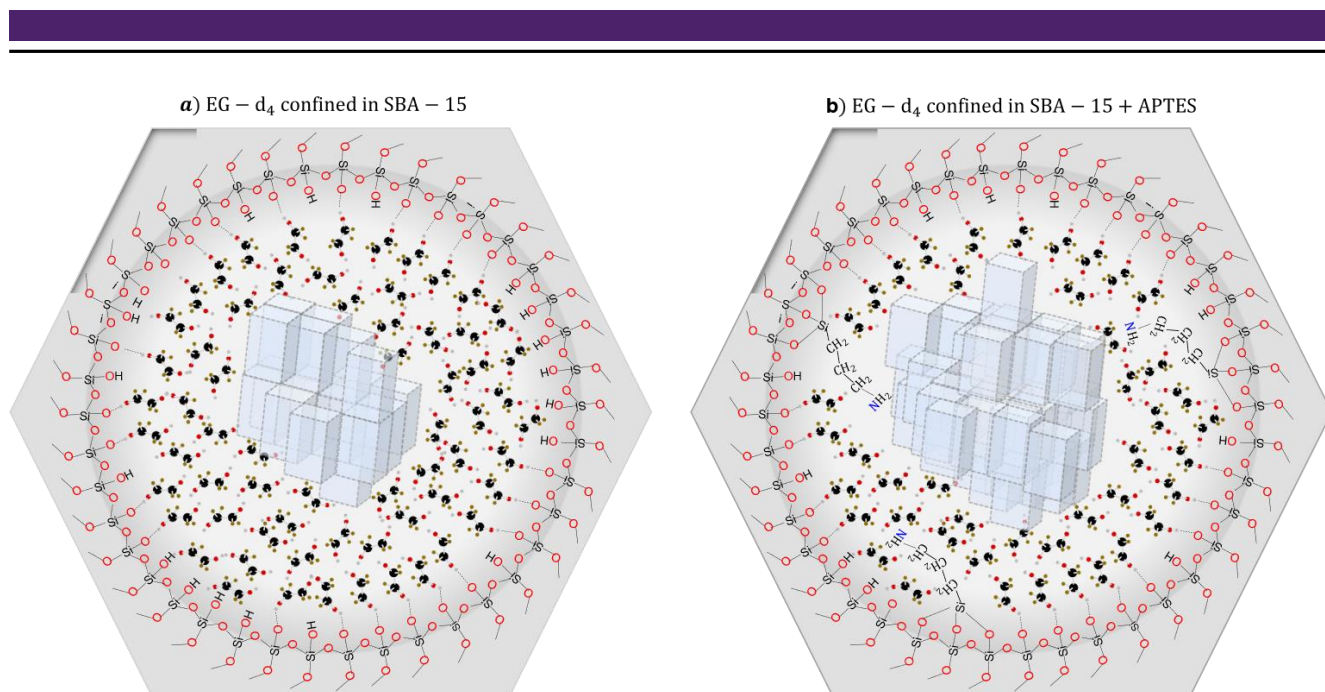


Figure 7.10 Schematic illustration of the arrangement of EG- d₄ molecules inside the pores of: a) pure SBA- 15 and b) APTES functionalized SBA- 15. This picture includes the formation of crystal-like structures of EG- d₄ in the middle of the pores as well as amorphous structures of EG- d₄ close to the pore wall. Picture taken from ref.^[164].

Interestingly, we observe a gradual increase in the intensity of the Lorentzian line-shape component in Figures 7.4-7.6 as the temperature rises, rather than discrete increments one might expect with the presence of two distinct endothermic peaks in the heating curves. This observation implies that the intrinsic isotropic movements of ethylene glycol persist, even for some molecules in a solid state within the pore. One plausible explanation is that the freezing and melting processes are highly dynamic at the molecular level. A molecule undergoing free tumbling may lose sufficient kinetic energy to a neighboring molecule, causing it to cease tumbling, while the neighboring molecule begins tumbling freely. With increasing temperature, the frequency of intermolecular energy transfer may also rise, involving a growing number of molecules. This results in a gradual decrease in the Pake pattern in the ssNMR spectra, while the contribution of the Lorentzian line increases. It's worth noting that the temperatures at which the Lorentzian line dominates the ssNMR spectra align well with the temperatures at which the Endo₂ peak is observed in the corresponding heating curves. This alignment suggests that at these temperatures, molecules continue to tumble freely, requiring an increase in free energy. Such a motional process would be inherently random, with varying correlation times for molecules remaining in a state of free tumbling.^[159]

Rössler et al^[174] introduced a method for determining the distribution of activation energies for guest molecules in polymer systems, which was later adapted by some researchers for molecules in porous systems.^[77,168,175-177] The dynamics of confined molecules, in this case, partially deuterated ethylene glycol, are categorized into two groups: one exhibiting fast jump dynamics (similar to a liquid) and the other exhibiting slow jump dynamics (similar to a solid). This model excludes any intermediate jump mechanism. Equation 7.1 represents the

temperature dependence of what Rössler referred to as the “relative intensity of the fast-jumping component,” denoted as $C_A(T)$. For clarity, we will refer $C_A(T)$ as the “mole fraction” of the fast-jumping component.

$$C_A(T) = \int_0^T \frac{1}{\sqrt{2\pi\Delta T^2}} \exp\left(-\frac{(T-T_0)^2}{2\Delta T^2}\right) dT = \frac{1}{2} \operatorname{erf}\left(\frac{1}{\sqrt{2\Delta T}}(T - T_0)\right) + \frac{1}{2} \operatorname{erf}\left(\frac{1}{\sqrt{2\Delta T}}T_0\right) \quad (7.1)$$

where $\operatorname{erf}(x)$ is the Gaussian error function, which is close to 0 at low temperatures and close to 1 at high temperatures, T_0 is the melting point as the center of gravity, and ΔT is the width of the distribution.

From eq. 7.1, the distribution of activation energies $g(E)$ in temperature units is obtained by eq. 7.2 as follows.

$$g(E) = \frac{d}{dT} C_A = \frac{1}{\sqrt{2\pi\Delta T}} \exp\left(-\frac{(T-T_0)^2}{2\Delta T^2}\right) \quad (7.2)$$

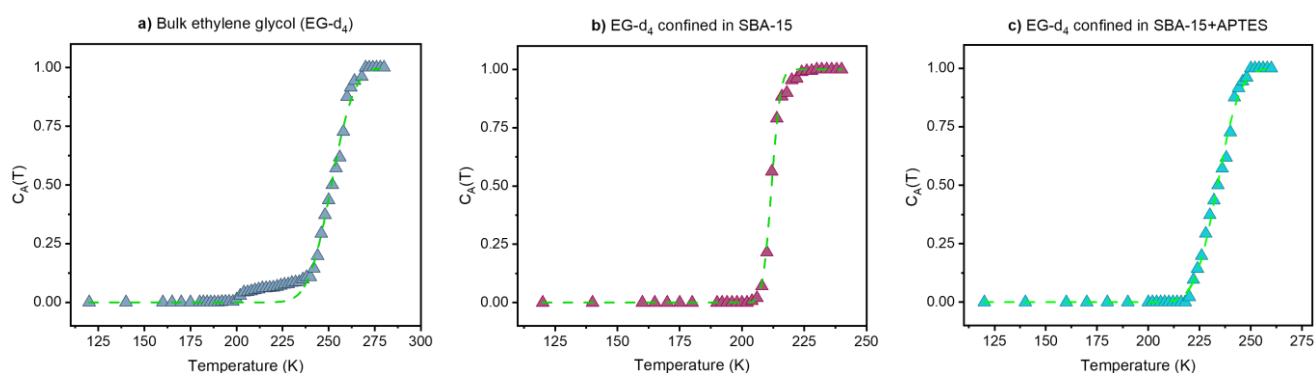


Figure 7.11. Mole fraction of the fast-moving component in the samples as a function of temperature, including the fitting with eq. 7.2. a) EG- d_4 in the bulk phase (sample 1), b) EG- d_4 confined in SBA- 15 (sample 2), and c) EG- d_4 confined in SBA- 15+APTES (sample 3). Figure adapted from reference^[164]

Figure 7.11 displays the experimental C_A values plotted against temperature T (represented as triangles), compared to the $C_A(T)$ values derived from eq. 7.2 (indicated by the green dashed line) for the three examined samples. In Figure 7.11a, it is evident that the model does not adequately fit the situation of EG- d_4 in the bulk phase (sample 1). This discrepancy is noticeable within the temperature range of 200 to 240 K, where deviations from the experimental data are observed. These deviations are attributed to the initiation of dynamics in a portion of molecules within this temperature range, a phenomenon not considered in the fitting model.

Conversely, for EG- d_4 in a confined environment (samples 2 and 3) as shown in Figures 7.11b and c, the two-phase model employed effectively describes the experimental findings. This observation suggests that the NMR spectra capture two distinct types of molecular motions: fast motions, similar to those in a liquid-like state, attributed to molecules primarily located in close proximity to the pore wall, and slower-frequency motions, induced by molecules situated in the central region of the pore, displaying solid-like behavior. As the temperature rises, the number of molecules contributing to the Lorentzian component (liquid-like) gradually increases until all of them have passed over into a melted state.

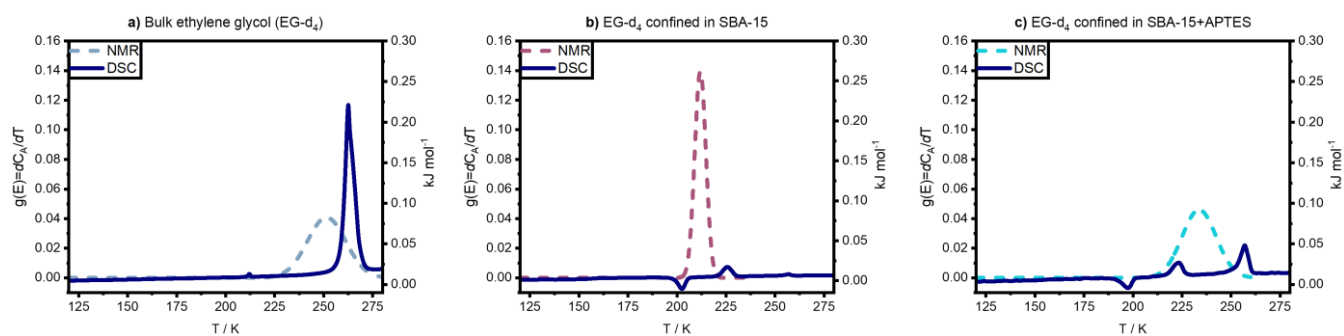


Figure 7.12. Comparison of activation energy distributions obtained from the NMR spectra caused by isotropic motions, and DSC curves encoding translational motions of EG- d_4 as a function of temperature for a) EG- d_4 in the bulk phase (sample **1**), b) EG- d_4 confined in SBA-15 (sample **2**), and c) EG- d_4 confined in SBA-15+APTES (sample **3**). Note: The distributions of activation energies (dashed lines) were calculated with eq. 7.2. The DSC curves (solid lines) were recorded at 5 K/min.

Figure 7.12 presents a comparison between the activation energy distributions that encode isotropic motions in guest molecules and the DSC curves that capture translational motions of EG- d_4 during the heating process for the three studied systems. In the case of EG- d_4 in the bulk (Figure 7.12a), the energy distribution, denoted $g(E)$, exhibits a maximum at 252 K, which is 11 K lower than the phase transition temperature recorded in the DSC curve at 263 K. For EG- d_4 confined within SBA-15 (Figure 7.12b), the activation energy distribution reaches its maximum at 212 K, which is 14 K lower than the first melting event at 226 K and 45 K lower than the second melting event at 257 K. Finally, for EG- d_4 confined in SBA-15+APTES (Figure 7.12c), the maximum of the activation energy distribution occurs at 234 K, which is 11 K higher than the first melting event at 223 K and 23 K lower than the second melting event at 257 K.

Comparing the activation energy distributions $g(E)$ for EG- d_4 in the bulk (sample **1**) and EG- d_4 confined in SBA-15+APTES (sample **3**), we find that they exhibit similar widths with a ΔT of approximately 30 K. However, there is a noticeable difference in their center of gravity, with sample **1** being approximately 18 K higher than for sample **3**. On the other hand, the distribution for EG- d_4 in SBA-15 (sample **2**) is notably narrower when compared to the activation energy distributions for samples **1** and **3**.

The phase transitions observed in the DSC curves primarily reflect changes in the translational motions of EG- d_4 . For the confined samples, multiple phase transitions occur during the heating process. Interestingly, the NMR results indicate that the isotropic motions are not significantly affected during these phase transitions. The narrower activation energy distribution in sample **2** can be explained by the substantial amount of EG- d_4 distributed in close proximity to the pore wall. This results in a high number of hydrogen bonds formed between the guest molecules and the immobile hydroxyl groups of the pore walls, causing EG- d_4 molecules to exhibit a glass-like behavior, including faster dynamics as the temperature increases, in comparison to samples **1** and **3**. The amount of EG- d_4 near the pore surface is significantly lower for sample **3**, where a substantial portion of

the surface hydroxyl groups is blocked with the ethoxy groups of APTES, and other parts may be inaccessible due to blocking by the APTES alkyl chain.

7.4 Conclusions and Summary

This chapter reported the results of how the presence of APTES groups on the pore walls of SBA-15 impacts the dynamics of deuterated ethylene glycol (EG- d_4). Three systems were compared: EG- d_4 confined in APTES-functionalized SBA-15 (sample **3**), EG- d_4 confined in pure SBA-15 (sample **2**), and EG- d_4 in its bulk phase (sample **1**). Differential scanning calorimetry (DSC) analysis revealed significant differences in physical properties such as melting, crystallization, and glass formation among the three systems.

Within the confinement of the pores, molecules experience distinct interactions, including those near the pore wall, in the pore center, and in an intermediate region. Hydrogen bonds formed between silanol groups on the pore walls and EG- d_4 strongly influence the alignment of EG- d_4 molecules, preventing them from forming ordered crystalline structures. This influence diminishes as more EG- d_4 molecules form hydrogen bonds with each other. The presence of APTES groups reduces the formation of hydrogen bonds between EG- d_4 molecules and the pore wall, leading to an increased number of EG- d_4 molecules in the pore center, exhibiting dynamics similar to bulk EG- d_4 . In contrast, EG- d_4 molecules in pure SBA-15, due to these hydrogen bonds, exhibit dominating glass transitions.

Through line shape analysis of ^2H solid-state NMR spectra at varying temperatures, two components were identified at temperatures corresponding to phase transitions: Lorentzian lines indicative of a liquid-like phase and a Pake pattern representative of a solid-like phase. Using the two-phase model proposed by Rössler et al.^[174], the distribution of activation energies for the three systems was calculated. Similar broad distributions of activation energies were observed for EG- d_4 in APTES-modified SBA-15 and EG- d_4 in the bulk phase, indicating similarities in dynamics. Conversely, EG- d_4 confined in pure SBA-15 exhibited a narrower activation energy distribution, highlighting the substantial influence of $\text{O}\cdots\text{HO}$ hydrogen bond formation between EG- d_4 and OH groups on the surface of SBA-15 on EG- d_4 dynamics.

In summary, the insights gained from studying EG- d_4 interactions with APTES-decorated SBA-15 have significance for understanding confinement effects in drug delivery systems and of heterogeneously catalyzed reactions in green solvents. Furthermore, these findings can serve as an experimental database for molecular dynamics simulations of confined EG- d_4 .

8 DNP Investigation of Novel Biradicals for Application in Polarization Transfer in Biological Systems

In this chapter, only the segment related to the results of ssNMR with DNP, which is part of the findings reported in the references^[177] and ^[144], is presented. The synthesis of radicals, their structural characterization, quantum chemical calculations, EPR studies, and tests for radical reduction resistance under biological conditions were conducted by a collaborative group led by Professor Bagryanskaya.

8.1 Introduction

Dynamic nuclear polarization (DNP) has emerged a powerful method to enhance the sensitivity of solid-state NMR spectroscopy, particularly in the analysis of biological systems.^[36,152,178–182] This technique relies on transferring polarization from highly polarized unpaired electron spins in polarizing agents (PAs) to nuclear spins within samples, by microwave irradiation.^[152] The obtainable enhancement is linked among others to the relaxation times of both electron and nuclear spins, where longer relaxation times typically correlates with higher enhancements.^[42] A variety of PAs have been employed, including nitroxides, trityls, biradicals, and transition metal complexes. Nitroxide biradicals have exhibited remarkable DNP performance due to the cross-effect polarization transfer mechanism.^[44,56]

Extensive research on nitroxide biradicals has been conducted in high magnetic fields, leading to structural modifications aimed at optimizing electron-electron interactions and electronic relaxation times. A noteworthy modification involves substituting geminal-dimethyl groups adjacent to the nitroxide moiety with spiro cyclohexyl derived groups. This alteration extends the spin echo dephasing time of the electron spin, thereby enhancing DNP performance at lower temperatures. This modification has successfully been applied to manufacture the highly efficient biradicals of the TEKPOL and AMUPol series.^[32,141,142]

Recent advancements have introduced novel rigid linkers for biradicals through intramolecular [2+2]-cycloaddition of ferrocene-1,10-diyl bis(carbodiimide) derivatives. Pyrroline nitroxide was selected as the spin-bearing component due to its chemical stability and well-established understanding of its electronic and molecular structure.^[183,184]

In this study, two groups of radicals are examined. The first group comprises radicals featuring spiro cyclohexane-substituted nitroxides (Figure 8.1 a and b), offering an alternative to the tetramethyl-substituted derivatives. The second group consists of radicals with a structural framework based on five-membered-ring nitroxides and tetraethyl substituents (Figure 8.1 c and d) which we will refer as spiro-substituted nitroxide radicals.

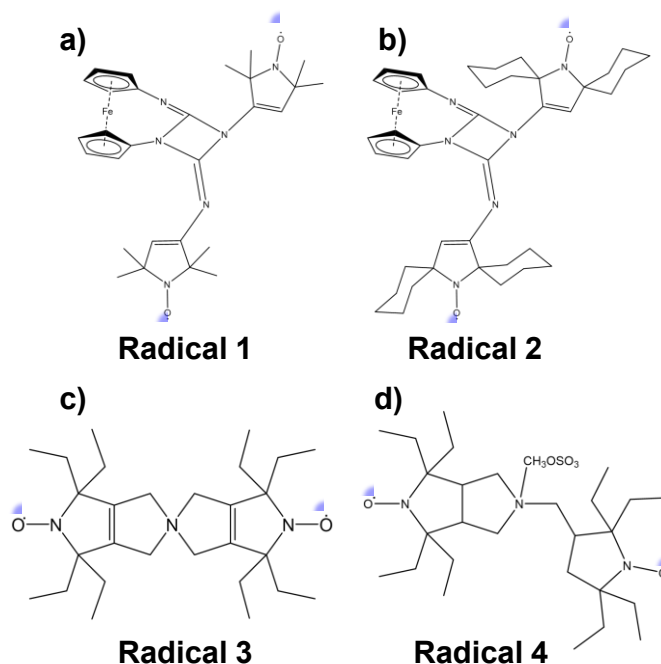


Figure 8.1. Chemical structures of the radicals reported in this chapter, a) and b) belong to spiro cyclohexane-substituted nitroxides radicals, c) and d) spiro-substituted nitroxide radicals.

As mentioned before spiro cyclohexane derived substituents are known for their prolonged electron spin relaxation. Furthermore, they are robust in reducing environments while ring-nitroxides and tetraethyl substituents are known to provide additional stability to the structure.^[141] Comparisons between biradicals featuring methyl and spiro cyclohexane substituents at specific nitroxide positions unveiled the impact of these substitutions, affecting not only the strength of exchange interactions but also the reactivity of the 1,3-diazetidone linker. The latter factor can influence the distance between nitroxide components, thereby altering spin-spin interactions.^[42]

To summarize, this study aims to investigate the interplay between biradical structure and DNP performance.

8.2 Results

8.2.1 EPR Results

The subsequent EPR results were conducted by our collaborators in the group led by Bagryanskaya and are more extensively discussed in references ^[160] and ^[144]. A brief summary is provided below to facilitate a more in-depth explanation of the results obtained through ss-NMR with DNP.

In order to characterize the local structures of the radicals, continuous-wave (CW) EPR experiments with a X-band (9.4 GHz, 0.35 T) spectrometer were performed. The resulting spectra were fitted using the EasySpin.^[185] software package. The EPR spectra and more information about the fitting procedure are presented in appendix,

section 10.5. The resulting exchange coupling parameters (J) of the fits are summarized in table 8.1 for the four radicals.

Table 8.1. Calculated exchange coupling parameter (J), corresponding to the best fit of the EPR for the four different radicals at 290 K. Radicals **1** and **2** were dissolved in toluene, for **3** and **4** a phosphate-buffered saline solution was used.

Radical	Energy interaction parameter (J_0), MHz	
1	85	
2	$J_1 = 109$ (49%)	$J_2 = 0$ (0%)
3	206	
4	0 (Distribution)	

8.2.2 DNP Results

Figures 8.2 and 8.3 display the ^1H MAS and $^1\text{H} \rightarrow ^{13}\text{C}$ CPMAS spectra for both sets of biradicals, spiro cyclohexane-substituted nitroxide radicals (**1** and **2**), as well as spiro-substituted nitroxide radicals (**3** and **4**). In all the spectra presented in both Figures, the signal originating from the silicon plug at approximately 0 ppm is marked with a # symbol.

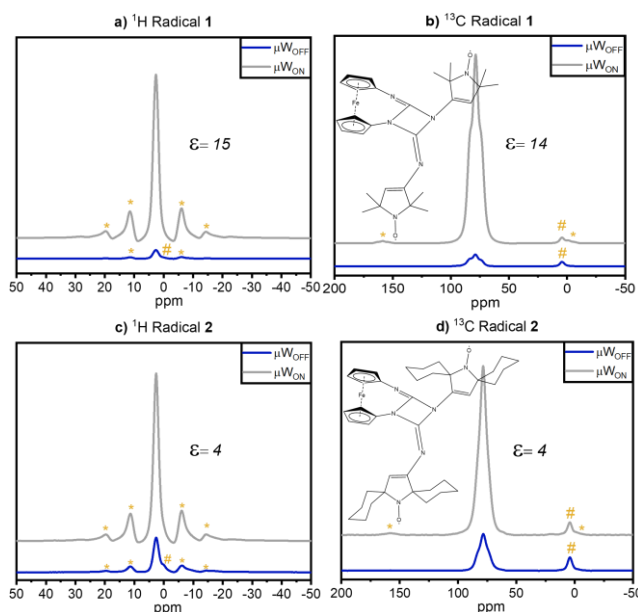


Figure 8.2. ^1H MAS and $^1\text{H} \rightarrow ^{13}\text{C}$ CPMAS spectra of a 15 mM solution of biradicals: **1** (a and b) and **2** (c and d) in TCE. Measurements were performed at nominally 115 K in the presence (μW_{ON}) and absence (μW_{OFF}) of microwave irradiation. The # indicates the signal from the silicon plug near 0 ppm. Signals marked with asterisks are spinning sidebands.

In the proton spectra depicted in Figure 8.2a and c, the signal at 6.6 ppm corresponds to the two equivalent protons within the frozen matrix (TCE). Simultaneously, in the ^{13}C spectra (Figure 8.2b and d), the predominant signal results from the overlap of the two carbons also present in the matrix. Regarding the enhancement, biradical **1** exhibits an enhancement of 14 for ^1H and 15 for ^{13}C , while polarization agent **2** only achieves an enhancement of 4 for both nuclei.

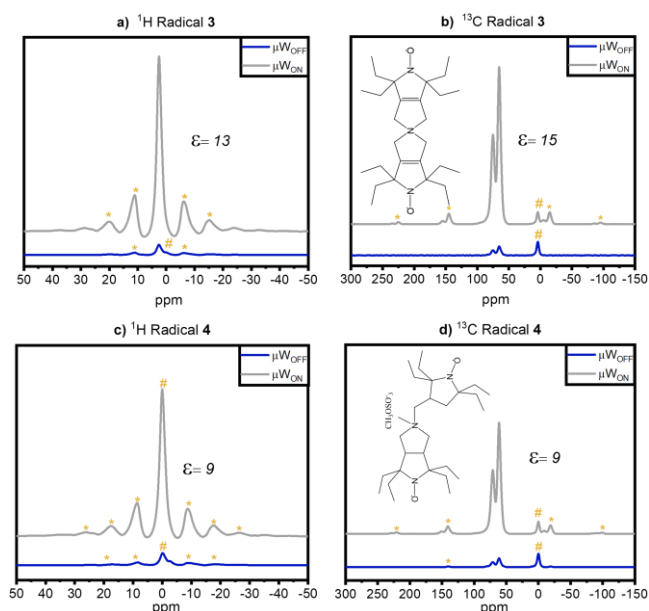


Figure 8.3. ^1H MAS and $^1\text{H} \rightarrow ^{13}\text{C}$ CPMAS spectra of a 15 mM solution of spiro-substituted nitroxide radicals: **3** (a and b) and **4** (c and d) in 60 %v/v of glycerol- d_8 , 30%v/v D_2O and 10 %v/v H_2O . Measurements were performed at nominally 115 K in the presence (μW_{ON}) and absence (μW_{OFF}) of microwave irradiation. The # indicates the signal from the silicon plug near 0 ppm. Signals marked with asterisks are spinning sidebands.

In Figure 8.3a and c, the ^1H MAS spectra show the presence of a peak at 6.2 ppm for the frozen radical solutions of **3** and **4**. This peak is attributed to the isotropic signal originating from water within the frozen matrix (glycerol- $d_8/\text{D}_2\text{O}/\text{H}_2\text{O}$). Radical **3** reaches an enhancement factor of 13, while radical **4** shows an enhancement factor of 9 in ^1H MAS NMR. In the $^1\text{H} \rightarrow ^{13}\text{C}$ CPMAS spectra (Figure 8.3b and d), the signals at 60.7 and 70.5 ppm correspond to the aliphatic carbons of glycerol, which is a component of the matrix. Radical **3** reaches an enhancement factor of 15, while radical **4** has an enhancement factor of 9.

These similar enhancement factors observed in the $^1\text{H} \rightarrow ^{13}\text{C}$ CPMAS and their corresponding ^1H MAS spectra for the four frozen radical solutions, provide clear evidence of a uniform distribution of the radicals within the frozen solutions.

8.3 Discussion

8.3.1 Enhancements in ^1H MAS and $^1\text{H}\rightarrow^{13}\text{C}$ CP MAS experiments

The results presented in Table 8.1 were obtained by Asanbaeva et al.^[144,160] The EPR spectra of each radical was fitted to obtain the exchange coupling energy (J) using the EasySpin software 5.2.28.^[185] For radicals **1** and **2**, these results were corroborated by the outcomes from quantum-mechanical calculations using the ORCA 4.2.1 software suite,^[186] all this performed by the group of Bagryanskaya.

The findings for radical **1** revealed the existence of four structural conformers in equilibrium, each demonstrating approximately the same exchange interaction energy (85 MHz). Consequently, a single value of the exchange coupling parameter (J) is reported. In the case of radical **2**, similar to radical **1**, quantum-mechanical calculations revealed the existence of four conformers. However, unlike the first radical, these four structures could be classified into two sets. The first set comprised two structures with similar interaction energies, which were higher than the energies observed for the other pair with similarly low energy values. Due to the comparable energies of the conformers within each pair, only two J values are reported: $J\approx 200$ MHz and $J\approx 0$ MHz for radical **2**.

For radicals **3** and **4** no quantum-mechanical calculations were reported to corroborate the results of the EPR fittings. For the radical **4** the reported value of $J=0$ indicates the existence of multiple conformers, which would lead to a broad distribution of exchange coupling values. This distribution would have its center at 0 and a standard deviation $\sigma = 120$ MHz.^[144]

In terms of their efficacy as polarization agents (PAs) in Dynamic Nuclear Polarization (DNP) experiments, the observed enhancement differences between radical **1** and **2** can be attributed to the presence of a substantial fraction (approximately 50%) of a conformer of the biradical **2** with $J = 0$ MHz. The presence of this conformer diminishes the DNP effect compared to radical **1**, for which an enhancement value of 14 is achieved, whereas radical **2** only attained an enhancement value of 4. It is important to emphasize that the value of J significantly influences the DNP effect. In the case of radicals **1** and **2**, J is influenced not solely by conformational changes but also by the specific chemical properties of 1,3-azetidines.^[187,188] These properties are known to trigger ring cleavage reactions when interacting with nucleophiles, leading to the formation of new biradicals characterized by larger distances between the radical centers and very low J values.^[141,189]

For the second set of radicals the smaller enhancement factor of 9 achieved for the radical **4**, compared to the value of ~ 14 obtained for the radical **3**, is attributed to the presence of conformers with different J values in the matrix as the calculations discussed before have shown.

Another factor that influences the enhancement is the build-up time (T_B). T_B is the time the nuclear spins need to reach their maximum polarization level as a result of a polarization transfer. In Figure 8.4 build-up curves for the two sets of radicals are shown. Mono-exponential functions (eq. 10.1) were used to fit the data points for all the samples. The resulting fitting parameters are shown in table 10.3 in the appendix.

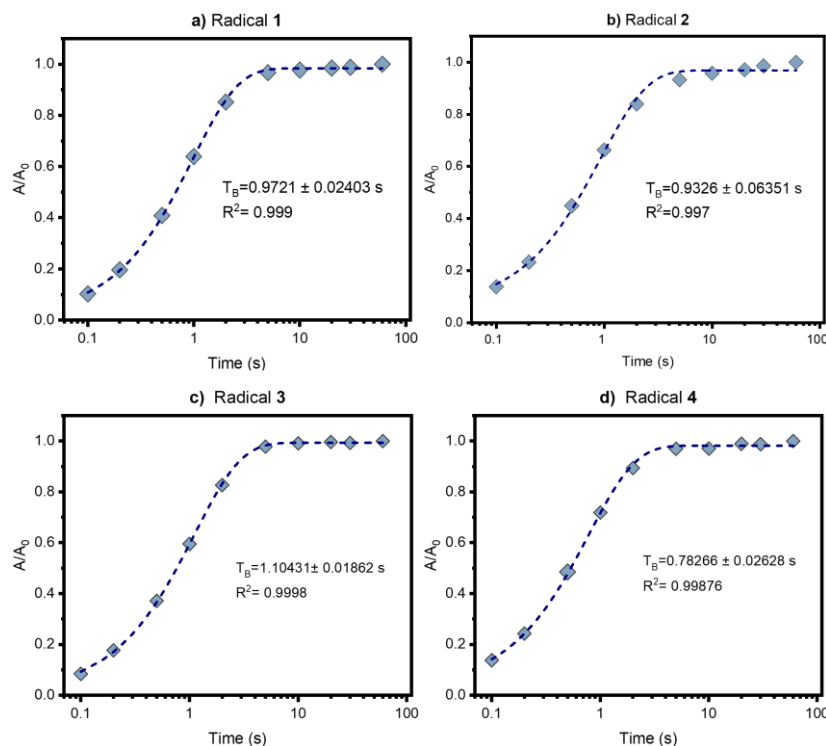


Figure 8.4. ^1H build-up curves obtained for a) radical **1**, b) radical **2** c) radical **3** and, d) radical **4**, at nominal 115 K with microwave radiation (μW_{ON}). The data were fitted to a mono-exponential function.

For radicals **1**, **2**, and **3**, the build-up time (T_B) was approximately 1 s, with a slightly shorter calculated time for radical **4** (0.78 s). In the cases of radicals **2** and **4**, the mono-exponential function does not accurately capture some points on the graph. This discrepancy could be attributed to the presence of conformers in these samples. Additionally, radicals **2** and **4** require less time to acquire electron polarization compared to the other two radicals, aligning with their lower enhancement.

8.3.2 Direct vs. Indirect Polarization in ^{13}C MAS

To explore the polarization transfer mechanism for the novel radicals, experiments aimed at obtaining direct ^{13}C MAS spectra from the frozen solutions of the four radicals were performed. The polarization transfer in such experiments is strongly influenced by the local dynamics within the vicinity of each radical.^[140,190–194] The outcomes presented in Figures 8.5-8.6 were obtained employing a build-up time of 300 s under two conditions: with and without microwave irradiation.

In Figures 8.5 and 8.6, for all frozen radical solutions measured without microwave irradiation (μW_{OFF}), the indirect polarization route, starting from electrons (e^-) and passing through ^1H before proceeding via cross-relaxation to ^{13}C , exhibits minimal impact across all the analytes. This observation is not very surprising because the transfer of polarization via cross-relaxation in solid-state systems is constrained and is typically observable only through DNP enhancement.^[195]

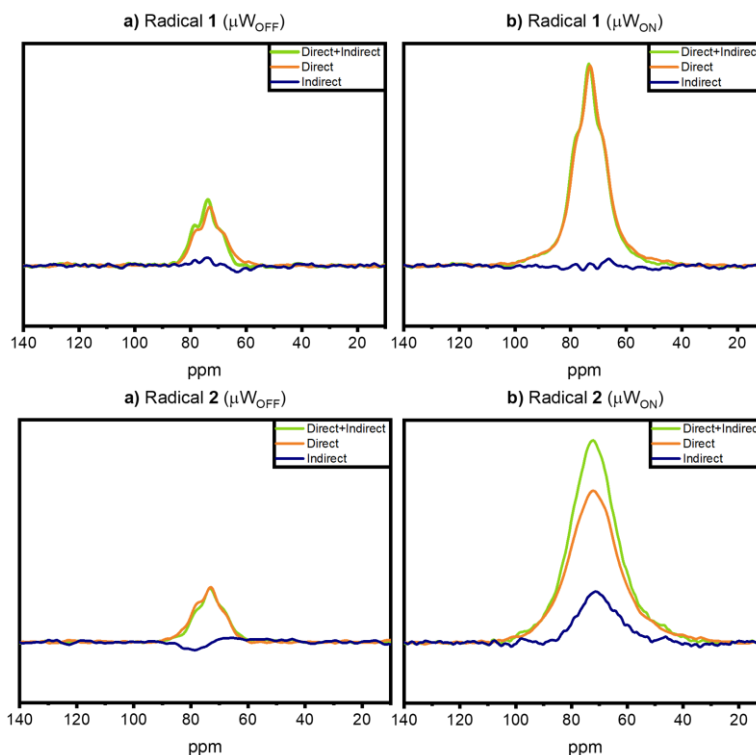


Figure 8.5. ^{13}C MAS spectra obtained at a build-up time of 300 s for biradical **1** (a) without microwave irradiation (μW_{OFF}), (b) with microwave irradiation (μW_{ON}), and for radical **2** (c) without microwave irradiation (μW_{OFF}), and (d) with microwave irradiation (μW_{ON}). Spectra were recorded at nominal 115 K. Note: The ^{13}C MAS spectra showing the direct and indirect pathway were recorded with a saturation recovery sequence in the ^{13}C channel described in the section 5.8. The spectra depicting only the direct pathway were recorded with a saturation recovery sequence in the ^{13}C channel where during the build-up time, rotor-synchronized 180° pulses were applied to the ^1H channel.

For biradical **1**, the spectra with microwave irradiation (Figure 8.5b) reveal a noticeable presence of signals stemming from the indirect pathway. In contrast, biradical **2** (Figure 8.5d) does not exhibit the indirect pathway. This can be explained by the presence of methyl side groups in biradical **1**, thus initiating cross relaxation. Conversely, for biradical **2** (Figure 8.3d), the absence of the indirect pathway is likely due to the more rigid structure of this radical, which includes spiro substituents, as also previously observed in other similarly structured radicals.^[190]

Comparing the signal enhancements from the direct pathway for both radicals, a factor of 6 is observed for radical **1**, while a factor of 2 is observed for radical **2**, with a build-up time of 300 seconds.

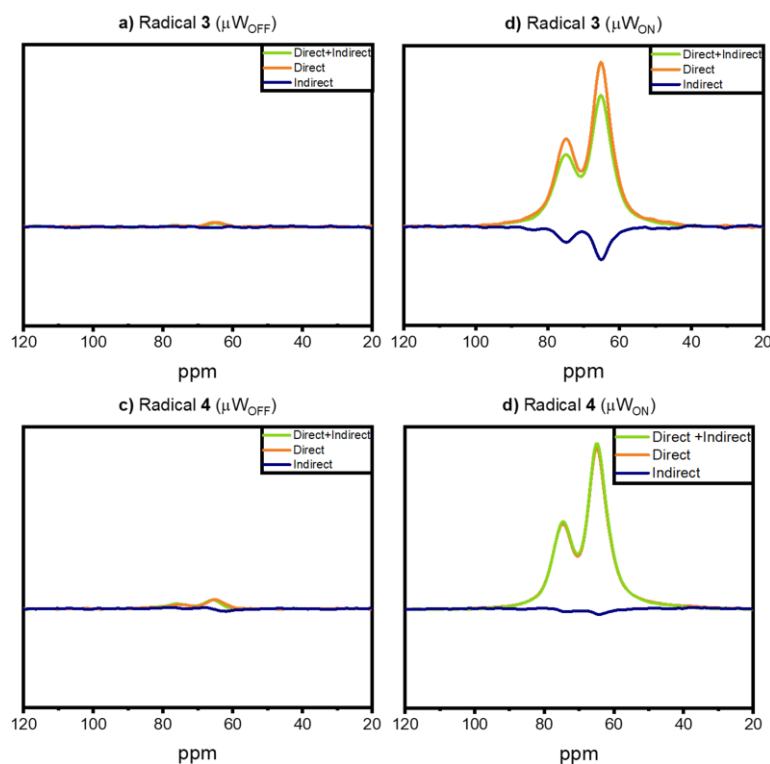


Figure 8.6. ^{13}C MAS spectra obtained at a build-up time of 300 s for the biradical **3** (a) without microwave irradiation (μW_{OFF}), (b) with microwave irradiation (μW_{ON}), and for biradical **4** (c) without microwave irradiation (μW_{OFF}), and (d) with microwave irradiation (μW_{ON}). Spectra were recorded at nominal 115 K. Note: The ^{13}C MAS spectra showing the direct and indirect pathway were recorded with a saturation recovery sequence in the ^{13}C channel described in the section 5.8. The spectra depicting only the direct pathway were recorded with a saturation recovery sequence in the ^{13}C channel where during the build-up time, rotor-synchronized 180° pulses were applied to the ^1H channel.

In the case of spiro-substituted nitroxide radicals (**3** and **4**), the signal attributed to the indirect polarization pathway (Figure 8.6b) is clearly visible for radical **3**, while for radical **4** (Figure 8.6d), there is no significant signal observed. This discrepancy suggests that local motions within the frozen solution of radical **3** are more pronounced compared to radical **4**. These distinctions are likely attributed to the structural differences between these radicals, which strongly influence the dynamics of solvent molecules in close vicinity to the radicals.^[190] Apart from the indirect pathway observed in frozen solutions for both radicals, the signals arising from the direct polarization route with microwave radiation (μW_{ON}) are clearly responsible for the signal enhancement in both polarization agents. The results shown in Figure 8.6 reveal similar enhancements for both radicals in terms of direct polarization transfer, an enhancement factor of 12 for radical **3** is achieved, while biradical **4** achieves an enhancement of 11 under these experimental conditions.

It should be noted that the DNP enhancements observed for both spiro-substituted nitroxide radicals are lower compared to similar substituted biradicals presented by Stevanato,^[196] who reported values ranging from 23 to 330. The origin of this lower enhancement is likely associated with electron spin relaxation times.^[142] It is well known that longer electron spin relaxation times (T_{1e} and T_{2e}) facilitates the saturation of the EPR

transitions.^[55,197] This phenomenon plays a significant role in enhancing DNP at lower sample temperatures since electron relaxation rates decrease substantially with decreasing temperature.^[198,199] To explore this possibility, electron spin relaxation measurements for radicals **3** and **4** were performed by our collaborators at 9.7 T. They obtained values of approximately 1 μ s (T_{2e}) and around 0.3 ms (T_{1e}) for both radicals, measured at concentrations of 0.1 mM at 80 K. These values are notably shorter, at least half, compared to those reported in the literature for spiro substituted PAs.^[42,142,196] Additionally, it is important to note that the DNP experiments in this work were performed at significantly higher biradical concentrations of 15 mM, where even shorter T_{2e} and T_{1e} values are expected.

Another critical factor that influences the achieved DNP efficiency is the shielding of the radical center from solvents by the tetraethyl substituents. Kubicki et al.^[42] observed that biradicals containing tetraethyl groups can attain the optimum saturation factor (T_{1e}, T_{2e}), yet the DNP enhancement remains relatively low. This observation they attributed to radical shielding. The X-ray structural analysis of the tetraethyl nitroxides **3** and **4** reported in references^[200,201] illustrates this "shielding" effect, which results from the tetraethyl substituents forming a dense shell positioned approximately 3 Å away from the nitroxide moiety.

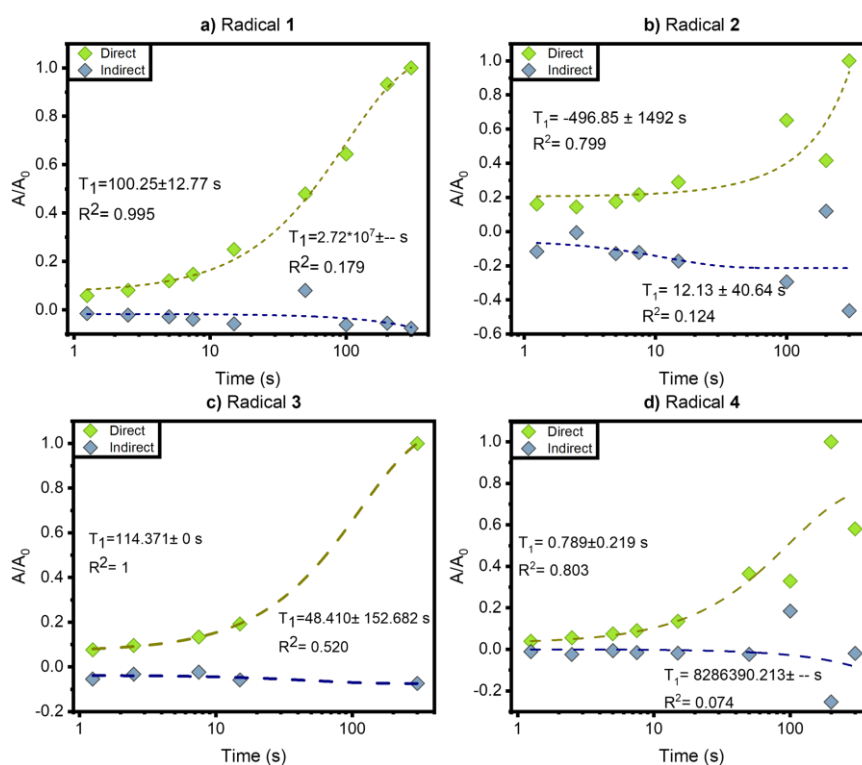


Figure 8.6. ^{13}C build-up curves for the direct and indirect paths obtained for a) radical **1**, b) radical **2**, c) radical **3** and d) radical **4**, at nominal 115 K in the presence of microwave irradiation (μW_{ON}). The data was fitted to a mono-exponential function.

Build-up curves for the signals generated by the direct ($e^- \rightarrow ^{13}\text{C}$) and the indirect ($e^- \rightarrow ^1\text{H} \rightarrow ^{13}\text{C}$) polarization transfer are shown in Figure 8.6 for the frozen solutions of the four radicals. Mono-exponential functions (eq 10.2) were used to fit the data points for all the samples. The resulting fitting parameters are shown in table 10.4 in the appendix.

In Figure 8.8b and d, it's evident that the mono-exponential fitting for radicals **2** and **4** does not accurately capture the data points. This discrepancy is likely attributed to the presence of different conformers in the solution of both radicals. It's crucial to note that, for these two radicals, the time required for the ^{13}C spins to reach their maximum energy level after the polarization transfer is smaller, as is their enhancement compared to radicals **1** and **3**.

The data from the indirect polarization pathway does not precisely conform to the mono-exponential fitting, emphasizing that these values should be considered indicative rather than exact calculations.

8.4 Conclusions and Summary

Two sets of biradicals were investigated as potential candidates for Polarizing Agents in Dynamic Nuclear Polarization experiments. The first set comprises two spiro cyclohexane-substituted nitroxide radicals (**1** and **2**), while the second set consists of two spiro-substituted nitroxide radicals (**3** and **4**).

Although the spiro cyclohexane-substituted nitroxide radicals exhibited a DNP enhancement, the values were not exceptionally high ($\epsilon \approx 14$ for radical **1** and $\epsilon = 4$ for radical **2**). This outcome may be attributed to suboptimal spin exchange interactions influenced by the flexible linkers. In the case of radical **2**, the lower enhancement can be ascribed to the presence of a high percentage of conformers with $J \approx 0$ MHz. Additionally, rapid electron spin relaxation within the tetraethyl environment contributes to this modest enhancement.

In the second set of radicals, it was observed that replacing methyl groups with spiro cycles near the N-O fragment resulted in the presence of conformers with J values close to zero, especially for radical **4**. Consequently, the DNP enhancement decreases in proportion to the increased contribution of zero exchange interactions, yielding enhancement values of $\epsilon \approx 14$ for radical **3** and $\epsilon = 9$ for radical **4**.

Although not previously mentioned, our collaborators tested the resistance to reduction of radicals **3** and **4** using ascorbate in buffer at pH 7.4. These tests demonstrated that both radicals exhibit high stability under these conditions, making them suitable for use in biological applications.

9 Summary

The first part of this thesis focuses on understanding Ethylene Glycol (EG) dynamics within Santa Barbara Amorphous materials (SBA- 15) and the impact of introducing the 3-aminopropyltriethoxysilane (APTES) group to the pore walls. APTES is commonly used for mesoporous material modification, and EG is chosen for its versatility and eco-friendliness as a solvent.

The experiments include Differential Scanning Calorimetry (DSC) and ^2H solid-state Nuclear Magnetic Resonance (ssNMR) to assess EG dynamics at varying temperatures. The ssNMR analyzes local structural features of partially deuterated ethylene glycol (EG- d_4), providing insights into shielding and quadrupolar interactions. Experiments have been conducted in 3 different systems: pure EG- d_4 (sample **1**), EG- d_4 in pure SBA- 15 (sample **2**), and EG- d_4 in SBA- 15 modified with APTES (sample **3**).

In the second part of the thesis new polarization agents to improve ssNMR sensitivity by DNP, where polarization is transferred from unpaired electrons to nuclei of interest, are investigated. Stable biradicals based on five-membered nitroxide rings and tetraethyl substituents have been used as model systems for the study, which evaluates the efficiency of these biradicals in enhancing NMR signals during DNP experiments and investigates the role of their structure on polarization transfer.

The main results of this work related to the research questions stated in Chapter 1 are summarized as follows:

Why do the dynamics of EG- d_4 confined inside SBA- 15 modified with APTES differ from the one confined in pure SBA- 15 and in the bulk?

In confinement, EG- d_4 molecules exhibit distinct dynamics that can be explained in terms of interactions, namely (i) in the vicinity of the pore wall (fast motions), (ii) in the pore center (slow motions), and (iii) in an intermediate region between them. When confined, EG- d_4 molecules near the pore walls interact with the -OH groups of the silica materials through hydrogen bonds. These interactions prevent EG- d_4 from adopting the same arrangement and therefore potential energy, as in the bulk phase, leading to a reduction in the melting temperature from 264 K in the bulk to 230 K in confinement. This effect becomes less pronounced closer to the pore center.

When the silica is decorated with the APTES groups, the number of OH groups interacting with the confined molecules decreases due to steric hindrance. Furthermore, the aliphatic chains in the APTES molecule interact with the OH groups of the material, limiting the number of hydrogen bonds between EG- d_4 and the material. The reduction in the number of these interactions allows a larger number of ethylene glycol molecules to arrange themselves similarly to the molecules in the bulk in the pore center. Although the effects of confinement forces still persist, they are only visibly manifested in a moderate decrease in the melting temperature, which is around 260 K compared to 264 K in the bulk.

What insights can be gleaned about the dynamics of EG- d₄ in various environments from deuterium ss-NMR parameters?

The line shape simulations of both static and MAS spectra in the three systems reveal two distinct characteristics: (i) a prominent Pake pattern at lower temperatures, indicative of a solid-like phase, and (ii) a pronounced Lorentzian line at higher temperatures, suggesting a liquid-like phase. The transition from a Pake pattern-dominant spectrum to a Lorentzian line-dominant spectrum varies among the samples, occurring within temperature ranges of 200 K to 270 K for sample **1**, 200 K to 230 K for sample **2**, and 226 K to 260 K for sample **3**.

Crucially, there are no significant changes in the shape of the Pake pattern and the Lorentzian line for the three samples, where only their intensities undergo alterations. The similarity in the shape of the Pake pattern and in their calculated quadrupolar coupling constants for the three samples suggests that the electric field gradient experienced by the ²H nuclei is comparable in the solid phase of all three samples.

For the confined samples, as the temperature, and thus the energy in the system, increases, the solid and liquid phases coexist in equilibrium until the rise in temperature only allows the existence of the liquid phase.

How does the dynamics of EG-d₄ evolve as a function of temperature under different environments?

The three systems exhibit an average value of $C_Q \approx 168$ kHz at low temperatures when only the solid phase is present. This value is typical for a rigid or slowly moving - CD bond, indicating that EG- d₄ undergoes slow or no motions in this temperature range independent from the environment.

As the temperature increases, molecules undergo isotropic motions. However, in confined samples, the observed pattern reveals a gradual increase in the liquid phase compared to the solid phase with rising temperature, indicating that some molecules experience isotropic motions even within the solid phase. A plausible explanation for this phenomenon is that freezing and melting processes are not a first phase transitions anymore, as in the bulk phase. Instead, due to randomly distribution of potentials, molecules may rotate freely without leaving their place in the arrangement. In a state of free tumbling, a molecule may transfer its kinetic energy to an adjacent molecule, causing it to cease tumbling, while the previously stationary molecule resumes free tumbling. As the temperature continues to rise, the frequency of intermolecular energy transfer is likely to increase, involving an expanding number of molecules in this process. This motional process is inherently random, characterized by varying correlation times during which molecules transition into a state of free tumbling.

Can the new radicals be used as polarization agents?

Two sets of biradicals were investigated. The first set comprised spiro cyclohexane-substituted nitroxide radicals (radicals **1** and **2**), while the second set consisted of spiro-substituted nitroxide radicals (radicals **3** and **4**).

The first set of radicals demonstrated enhancements of 14 for radical **1** and 4 for radical **2**. In the second set, radical **3** exhibited an enhancement value of 14, and radical **4** showed a value of 9. Moreover, the second set of radicals can be utilized in biological samples due to their structure remaining stable at pH 7.4.

Which polarization transfer mechanism, direct or indirect, is more favorable for the radicals in ^{13}C MAS experiments?

For all radicals, it was consistently observed that the direct pathway ($e^- \rightarrow ^{13}\text{C}$) is the more favored route for polarization transfer. In the case of the first set of radicals, this behavior aligns with findings in other radicals with a similar structure. However, in radical **1**, the presence of the methyl group in the structure allows for a small portion of the polarization to follow the indirect pathway ($e^- \rightarrow ^1\text{H} \rightarrow ^{13}\text{C}$), as this group facilitates cross relaxation.

In the case of the second set of radicals (**3** and **4**), it is noteworthy that they achieved similar enhancements, albeit lower when compared to the spiro-substituted biradicals of a similar nature. This difference is attributed to the remarkably short electron spin relaxation times observed in the radicals examined in this study.

One potential explanation for these shorter relaxation times for the second set, is radical shielding. This effect arises from the presence of tetraethyl substituents forming a dense shell located approximately 3 Å away from the nitroxide moiety.

10 Appendix

10.1 Adsorption-Desorption Measurements

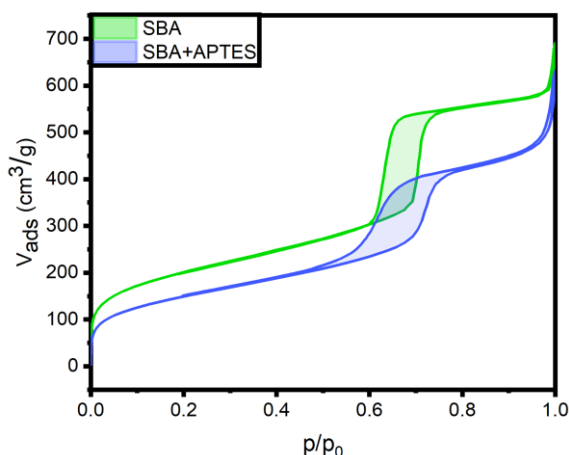


Figure 10.1. Nitrogen adsorption-desorption isotherms of the pure SBA- 15 and the SBA- 15 functionalized with APTES.

All adsorption-desorption measurements display a type IV isotherm (Figure 10.1), characteristic for mesoporous materials with open pores.^[155] The symmetrical hysteresis in the 0.5-0.75 p/p_0 range indicates a narrow pore size distribution.

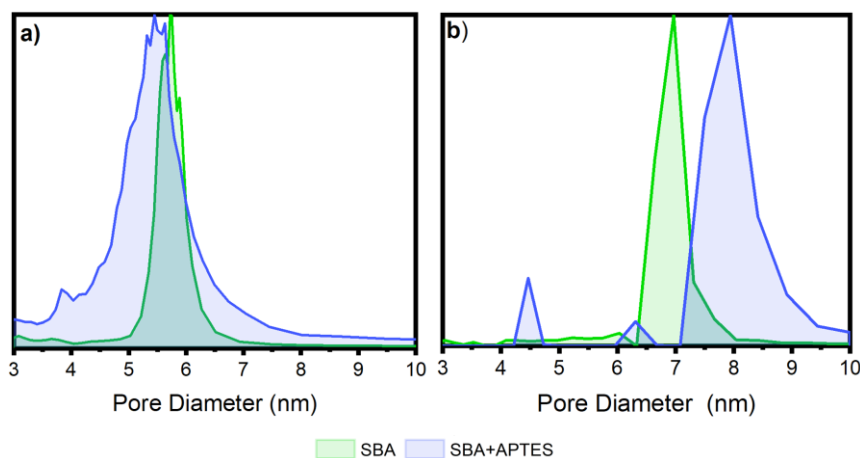


Figure 10.2. a) Pore size distributions derived from the BJH model for both pure SBA- 15 and APTES-functionalized SBA- 15. b) Pore size distributions calculated by non-local density functional theory (NLDFT) with cylindrical silica pores as the model, for both pure SBA- 15 and APTES-functionalized SBA- 15.

10.2 NMR Temperature Calibration

Temperature calibration for MAS experiments was carried out using a KBr (99.97%) sample from Sigma-Aldrich. A saturation recovery sequence was applied with a pulse length of 3.5 μs for both the 100 pulses in the saturation train and the detection pulse. The pulse spacing within the saturation train was set at 1 ms. A vclist containing build-up times ranging from 1 ms to 8 s was used. Spectra were recorded with 16 scans for each temperature reading obtained from the auxiliary sensor ($T_{\text{aux sensor}}$), with a repetition time of 0.1 s. The obtained

T_1 time for each T_{aux} sensor was determined by monoexponential fitting. To calculate the actual temperature in the sample (T_{sample}), the T_1 time obtained in each experiment was utilized to solve eq. 10.1 proposed by Thurber & Tycko.^[157]

$$T_1 = 0.0145 + \frac{5330}{T_{sample}^2} + \frac{(1.42 \cdot 10^7)}{T_{sample}^4} + \frac{(2.48 \cdot 10^9) \cdot s}{T_{sample}^6} \quad (10.1)$$

were, T_1 represents the spin-lattice relaxation time from each experiment in seconds, and T_{sample} stands for the true temperature in the sample in Kelvin. The values of T_{sample} were then plotted against $T_{aux\ sensor}$, as depicted in Figure 10.3.

For static experiments, the temperature readout obtained from a thermocouple located near the sample ($T_{aux\ sensor}$) was used as the sample temperature.

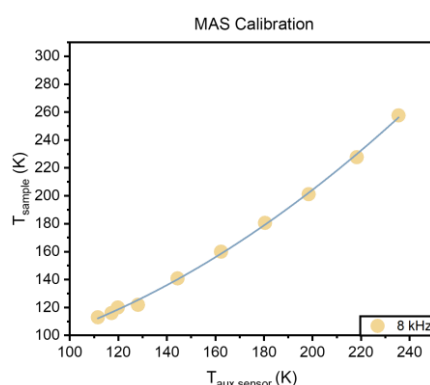


Figure 10.3 Calibration data, fitted using the polynomial fit according to eq. 10.2 for a MAS rate of 8 kHz.

The plotted data were fitted using the polynomial fit function:

$$T_{sample} = B_2 T_{aux\ sensor}^2 + B_1 T_{aux\ sensor} + C. \quad (10.2)$$

Fit parameters according to eq. 10.2 for MAS are reported in Table 10.1.

Table 10.1. Parameters of the polynomial fit in the temperature calibration under MAS and static conditions, respectively.

MAS 8kHz	
B_1	-0.01858 ± 0.15725
B_2 (1/K)	$0.0034 \pm 4.59736 \cdot 10^{-4}$
C (K)	71.87794 ± 12.70854
R^2	0.99883

10.3 Hysteresis effects in the ssNMR spectra

To confirm that the method of gradually increasing the temperature until the analyte reached a liquid state did not affect the results, the analytes were first brought to a liquid state inside the equipment and then cooled down to specific temperatures. A 20-minute waiting period was allowed for the sample to reach equilibrium before measurements were taken.

The spectra for both procedures, involving ethylene glycol in bulk, are presented in Figure 10.4. It is evident from the Figure that there are no significant variations in the line shape of the spectra between the two methodologies.

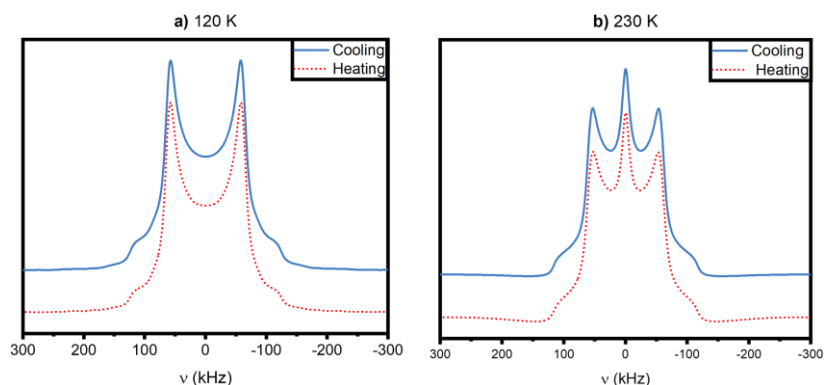


Figure 10.4. ^2H ss NMR spectra of partially deuterated ethylene glycol (EG- d_4) in the bulk (sample 1) measured at (a) 120 K and (b) 230 K, respectively. The spectra depicted in blue were measured using the cooling protocol (decreasing the temperature of the sample to the set point), the spectra depicted as red dots were measured using the heating protocol (increasing the temperature of the sample to the set point). Spectra were then acquired 20 minutes after the set point was reached to ensure thermal equilibrium.

10.4 Supplementary NMR Spectroscopic Data

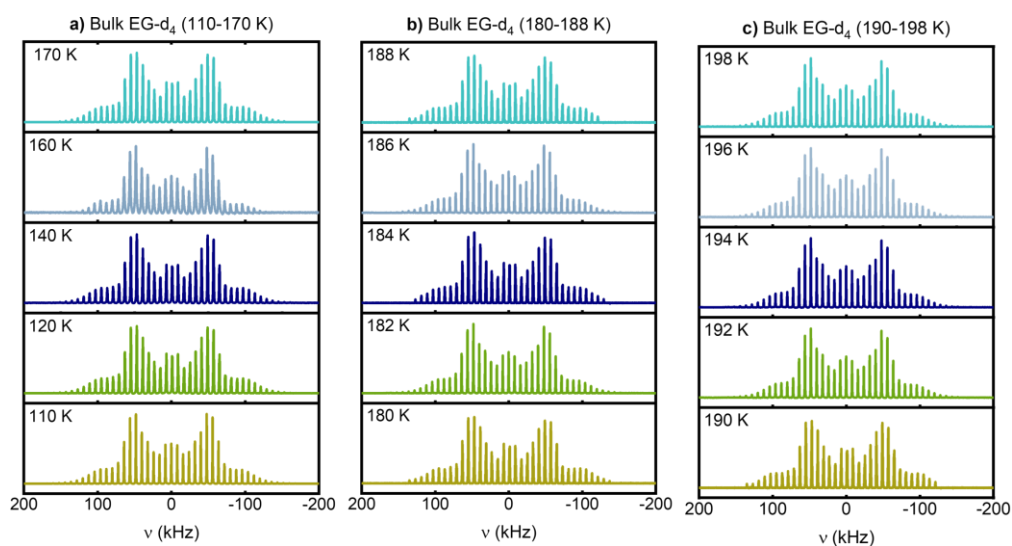


Figure 10.5. MAS ^2H ssNMR spectra obtained in the temperature range between 110 and 198 K for EG- d_4 in the bulk phase (sample 1).

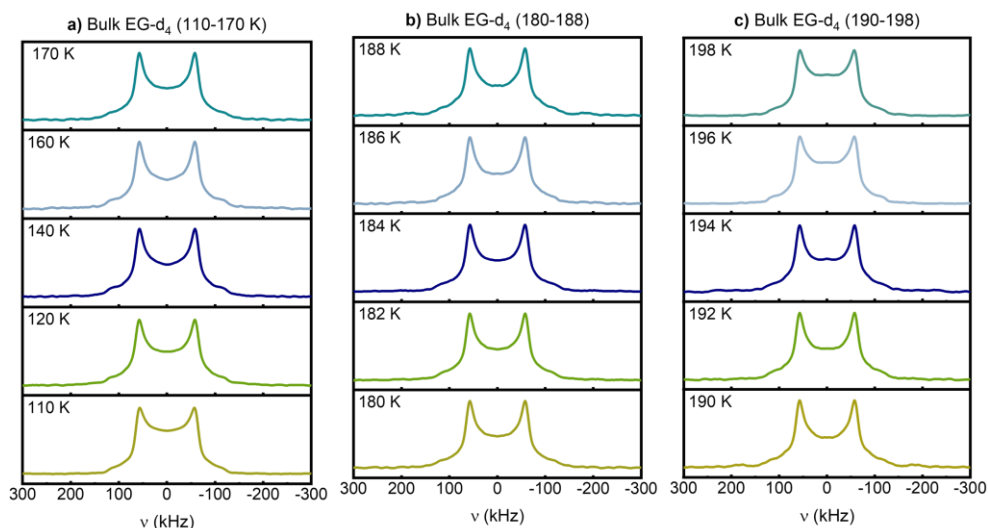


Figure 10.6. Static ^2H ssNMR spectra obtained in the temperature range between 110 and 198 K for EG- d_4 in the bulk phase (sample 1).

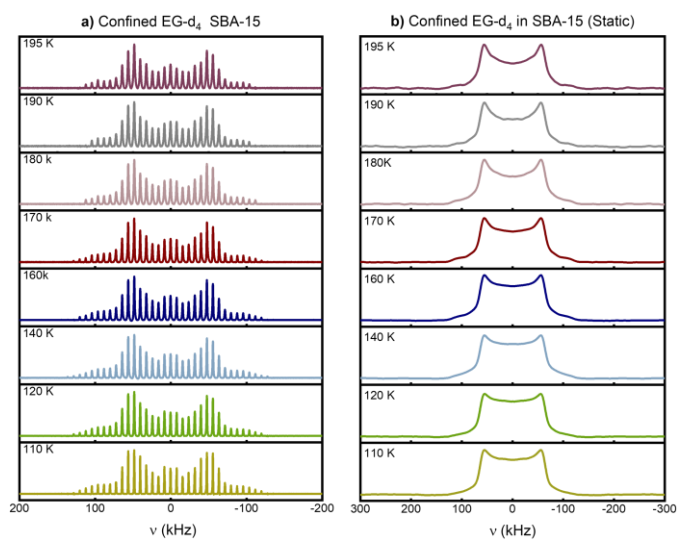


Figure 10.7. ^2H ssNMR spectra obtained in the temperature range between 110 and 195 K for EG- d_4 confined in pure SBA-15 (sample 2), a) MAS spectra b) static spectra.

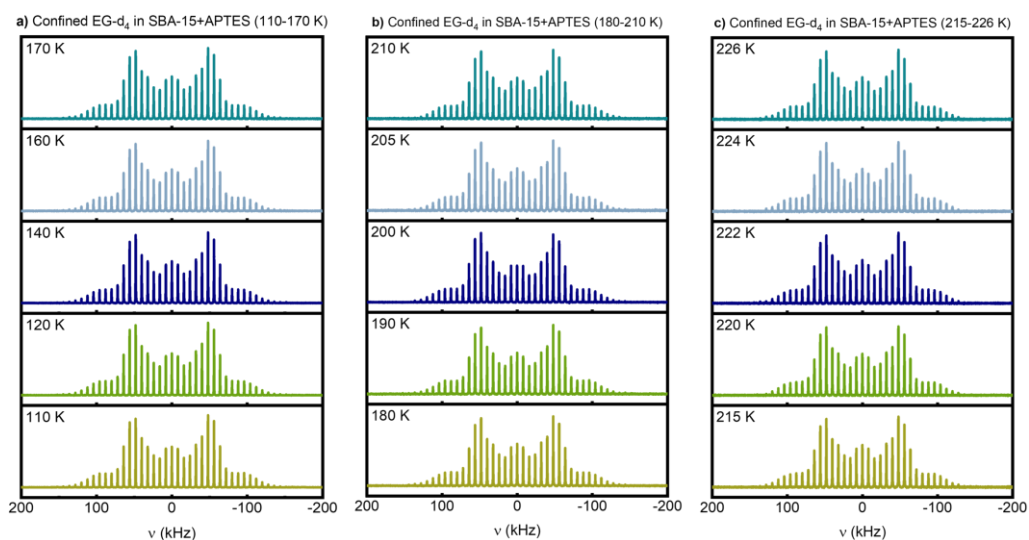


Figure 10.8. MAS ^2H ssNMR spectra obtained in the temperature range between 110 and 226 K for EG- d_4 confined in SBA-15+ APTES (sample **3**), before detectable shifts in the spectral line shape can be observed.

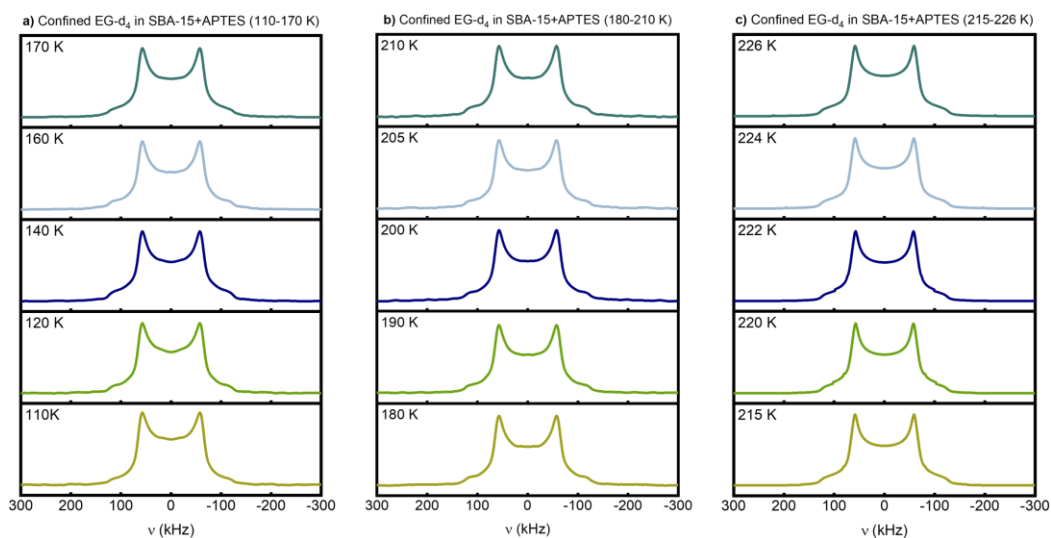


Figure 10.9. Static ^2H ssNMR spectra obtained in the temperature range between 110 and 226 K for EG- d_4 confined in SBA-15+ APTES (sample **3**), before detectable shifts in the spectral line shape can be observed.

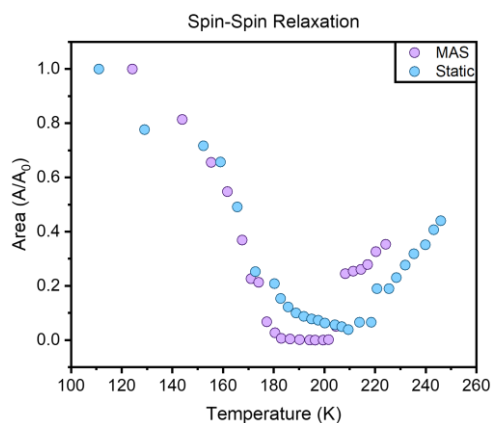
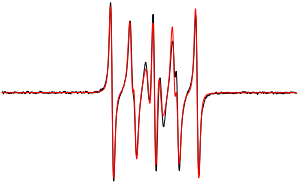
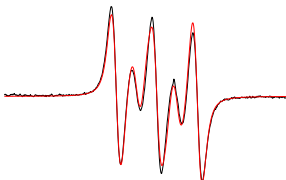

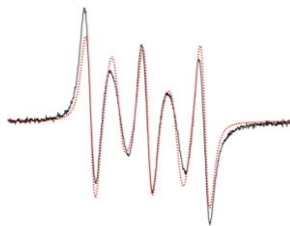


Figure 10.10. Comparison of the areas attributed to the slow motional component in MAS and Static ^2H ssNMR spectra. These spectra were acquired over a temperature range between 110 to 250 K for EG- d_4 confined within SBA-15 (sample **2**).

10.5 Supplementary EPR Data

The following data was furnished by the Bagryanskaya leadership group, which conducted the comprehensive analysis leading to these findings. A concise summary is outlined in this context, while more exhaustive details can be found in references ^[160] and ^[144].

Table 10.2 X-band EPR spectra at 290 K and their calculated parameters: superposition of the hyperfine coupling to ¹⁴N ($A_{N \text{ iso}}$), exchange coupling. Radicals **1** and **2** were dissolved in toluene, for **3** and **4** a phosphate-buffered saline solution was used.^[144,160]

Radical	EPR spectrum	Parameters of the simulations
1		$J_0 = 85 \text{ MHz}$ $\sigma(J) = 69 \text{ MHz}$ $A_N = 1.44 \text{ mT}$
2		$J_1 = 0 \text{ MHz (51\%)}$ $J_2 = 109 \text{ MHz (49\%)}$ $J_0 = 13 \text{ MHz}$ $\sigma(J) = 45 \text{ MHz}$ $A_N = 1.44 \text{ mT}$
3		$J = 206 \pm 2 \text{ MHz}$ $A_{N \text{ iso}} = 43.7 \pm 0.2 \text{ MHz}$
4		$J = 0$ $\sigma(J) = 120 \text{ MHz}$ $J \text{ distribution}$ $A_{N1 \text{ iso}} = 44.0 \pm 0.2 \text{ MHz}$ $A_{N2 \text{ iso}} = 43.2 \pm 0.2 \text{ MHz}$

The liquid EPR spectra presented in table 10.2 were analyzed using the *EasySpin* software package ²⁰ by our collaborators.

10.6 Fitting Parameters for Build-up Times

$$A_z = A_0 + B * e^{(-t/T_B)} \quad (10.3)$$

Table 10.3 Fitting parameters of equation 10.3 for each radical for ¹H built up times.

Radical	A ₀ (au)	B	T _B (s)
1	0.984±0.005	-0.971±0.009	0.972±0.024
2	0.969±0.010	-0.913±0.023	0.932±0.059
3	0.993±0.003	-0.986±0.006	1.104±0.017
4	0.789±0.219	-0.759±0.211	98.802±79.362

$$A_z = A_0 + B * e^{(-t/T_1)} \quad (10.4)$$

Table 10.4 Fitting parameters of equation 10.4 for each radical for ¹³C built up times. * The error for these values could not be determined due to the substantial variability observed among the data points.

Radical	Direct			Indirect		
	A ₀ (au)	B	T ₁ (s)	A ₀ (au)	B	T ₁ (s)
1	1.050 ±0.041	-0.977 ±0.04	100.25 ±11.65	-4974.93 +*	4974.91 ±*	2.72*10 ⁷ ±*
2	-0.676 ±3.5	0.88 ±3.47	-496.8 ±1492	0.213 ±0.112	0.163 ±0.220	12.128 ±40.64
3	1.073	-1.003	114.371	-0.074 ±0.020	0.037 ±0.026	48.410 ±152.682
4	0.789 ±0.219	-0.759 ±0.211	98.802 ±79.362	-2323.381 ±*	2323.382 ±*	8286390.213 ±*

10.7 TopSpin Pulse Programs

10.7.1 Saturation Recovery experiment (satrect1)

```

;satrect1
;
;TS 3/ 08.09.2011
;
;
;
;saturation recovery T1 experiment
;written by STE, 28.11.2002

```



```

;pulse program is for 2D acquisition
;establish suitable vd list
;uses mc syntax, so that it can be used in 1D mode for set-up of
;saturation pulse train
;
;Avance II+ version
;parameters:
;p11 : X power level
;p12 : =0W, not used
;p112 : power level for H 90 and standard proton decoupling
;p113 : e.g. used in spinal64_13
;p1 : X 90 degree pulse
;d1 : recycle delay
;d20 : delay in saturation pulse train
;l20 : number of pulses in saturation pulse train, 0 if undesired
;vdlst : list containing tau delays
;pcpd2 : pulse length in decoupling sequence
;FnMode : QF
;
;
;$CLASS=Solids
;$DIM=pseudo 2D
;$TYPE=direct excitation
;$SUBTYPE=T1/T2
;$COMMENT=saturation recovery T1 experiment
"acqt0=-p1/2"
1 ze
2 10m
#ifdef dec
d1 do:f2 ;recycle delay, decoupler off in go-loop
#else
d1
#endif /* dec */
#include <aq_prot.incl>
;allows max. 50 msec acquisition time, supervisor
;may change to max. 1s at less than 5 % duty cycle
;and reduced decoupling field
3 d20
(p1 p11 ph4):f1
lo to 3 times l20
vd ;recovery delay
(p1 p11 ph1):f1
#ifdef dec
1u cpds2:f2
#endif /* dec */
go=2 ph31
#ifdef dec
1m do:f2
#endif /* dec */
10m mc #0 to 2 F1QF(ivd)
HaltAcqu, 1m
exit

ph1= 0 0 2 2 1 1 3 3
ph4= 0
ph31= 0 0 2 2 1 1 3 3

;sid: $

```

10.7.2 One Pulse experiment (onepulse)

```

;onepulse (Topspin 3.0)
;
;TS 3/ 03.06.2011
;
;

```

```

; checked by sewe 03.06.2011
;
;
;Avance III version
;parameters:
;p11 : power level for excitation pulse
;p1 : excitation pulse length
;d1 : recycle delay
;acqt0 is used to backpredict the t=0 fid point
;
;
;
;$CLASS=Solids
;$DIM=1D
;$TYPE=direct excitation
;$SUBTYPE=simple 1D
;$COMMENT=single pulse excitation, acquisition without decoupling
"acqt0=-p1/2"
1 ze
2 d1
(p1 p11 ph1):f1
go=2 ph31
wr #0
exit
ph1= 0 2 1 3
ph31=0 2 1 3
;$Id: onepulse,v 1.2.18.3 2012/10/09 09:20:43 ber Exp $

```

10.7.3 Modified Solid Echo experiment (solidecho)

```

;solidecho (Topspin 2.0)
;
;TS 3/ 03.06.2011
;
;
; checked by sewe 03.06.2011
;
;
;
;90-90 solid echo sequence for wide line observation
;
;set d6 to 5-100usec depending on dead time
;set d7 shorter than d6 by 3usec plus 10 dw to make
;sure the evolution of the echo is observed, then left shift
;FID prior to ft to get smallest possible 1st order phase correction
;set receiver phase either with phcor0 or with HPCU receiver phase
;to get maximum signal in ADC channel A and almost no signal in channel B
;for minimum 0 order phase correction (no signal in channel B is only
;possible if O1 exactly in center and spectrum perfectly symmetric).
;phase cycle will cancel deadtime partially, but not perfectly
;
;parameters:
;p11 : X power level for 90
;p1 : X 90 degree pulse
;d1 : recycle delay
;d6 : echo delay
;d7 : =0, or no longer than d6-de
;ns : = 8*n
;
;
;
;$CLASS=Solids
;$DIM=1D
;$TYPE=direct excitation
;$SUBTYPE=simple 1D
;$COMMENT=90-90 solid echo sequence for wide line observation
;cnst11 : to adjust t=0 for acquisition, if digmod = baseopt
"acqt0=0"
1 ze

```

```

2 d1
(p1 p1 ph1):f1
d6
(p1 ph2):f1
d7
go=2 ph31
wr #0
exit
ph0=0
ph1= 0 3 2 1 0 3 2 1
ph2= 3 2 1 0 1 0 3 2
ph31= 3 2 1 0 3 2 1 0
;Sid: $

```

10.7.4 Modified Rotor-Synchronized Solid Echo Experiment (solidecho_synch_he)

```

;solidecho (Topspin 2.0)
;
;TS 3/ 03.06.2011
;
;
; checked by sewe 03.06.2011
;
;
;90-90 solid echo sequence for wide line observation
;
;set d6 to 5-100usec depending on dead time
;set d7 shorter than d6 by 3usec plus 10 dw to make
;sure the evolution of the echo is observed, then left shift
;FID prior to fit to get smallest possible 1st order phase correction
;set receiver phase either with phcor0 or with HPCU receiver phase
;to get maximum signal in ADC channel A and almost no signal in channel B
;for minimum 0 order phase correction (no signal in channel B is only
;possible if O1 exactly in center and spectrum perfectly symmetric).
;phase cycle will cancel deadtime partially, but not perfectly
;
;
;parameters:
;p11 : X power level for 90
;p1 : X 90 degree pulse
;d1 : recycle delay
;d6 : echo delay
;d7 : =0, or no longer than d6-de
;ns : = 8*n
;
;
;$CLASS=Solids
;$DIM=1D
;$TYPE=direct excitation
;$SUBTYPE=simple 1D
;$COMMENT=90-90 solid echo sequence for wide line observation

;cnst11 : to adjust t=0 for acquisition, if digmod = baseopt
"acqt0=0"
"d6=((1s*11)/cnst31)-(p1/2)-(p1/2)"
"d7=d6-de"

1 ze
2 d1
(p1 p1 ph1):f1
d6
(p2 ph2):f1
d7
go=2 ph31
wr #0
exit

```

```

ph0=0
ph1= 0 3 2 1 0 3 2 1
ph2= 3 2 1 0 1 0 3 2
ph31= 3 2 1 0 3 2 1 0
;Sid: $

```

10.7.5 Modified Background Suppression Experiment (zgbs_torsten)

```

;zgbs
;avance-version (12/01/11)
;1D sequence for suppression of background signals
;using composite pulse
;
;D.G. Cory & W.M. Ritchey, J. Magn. Reson. 80, 128-132 (1988)
;
;CLASS=HighRes
;DIM=1D
;TYPE=
;SUBTYPE=
;COMMENT=
#include <Avance.incl>
"acqt0=-p1/2"
"p2=p1*2"
1 ze
2 30m
3 d20
(p1 p11 ph4):f1
lo to 3 times l20
d1
(p1 ph1):f1
0.1u
(p2 ph2):f1
0.1u
(p2 ph3):f1
go=2 ph31
30m mc #0 to 2 F0(zd)
exit
ph1=0 0 0 0 1 1 1 1 2 2 2 2 3 3 3 3
ph2=0 1 2 3
ph3=0 0 0 0 2 2 2 2 3 3 3 3 1 1 1 1
ph4= 0
ph31=0 2 0 2 1 3 1 3
;d20 : delay in saturation pulse train
;l20 : number of pulses in saturation pulse train, 0 if undesired
;p11 : f1 channel - power level for pulse (default)
;p1 : f1 channel - 90 degree high power pulse
;p2 : f1 channel - 180 degree high power pulse
;d1 : relaxation delay; 1-5 * T1
;ns: 16 * n, total number of scans: NS * TD0
;Id: zgbs,v 1.3.8.1 2012/01/31 17:56:41 ber Exp $

```

10.7.6 Modified Crosspolarization Experiment (cp)

```

;cp
;
;TS3 / 03.06.2011
;

```

```

;basic cp experiment
;written by HF 1.3.2001
;changed by JOS 05/06/03
;comments added by STE 4.4.2006 and HF 16.06.2010
;checked by SEWE 03.06.2011
;
;Avance III version
;parameters:
;p3 : proton 90 at power level PLW12
;p15 : contact time at PLW1(f1) and SPW0(f2)
;p11 : X power level during contact
;p12 : =0W, not used
;p12 : decoupling power level (if not PLW13)
;p13 : special decoupling power level
;sp0 : proton power level during contact
;cnst21 : on resonance, usually = 0
;cpdprg2 : e.g. cw, spinal64 (at PLW12)
;d1 : recycle delay
;pcpd2 : pulse length in decoupling sequence (e.g. 180deg)
;spnam0 : use e.g. ramp.100 or ramp90100.100 for variable amplitude CP
;zgoptns : -Dfslg, -Dlacq, -Dlcp15, or blank
;
;
;$CLASS=Solids
;$DIM=1D
;$TYPE=cross polarisation
;$SUBTYPE=simple 1D
;$COMMENT=basic cp experiment, arbitrary contact and decoupling schemes
prosol relations=<solids_cp>

#include <Avancesolids.incl>

#ifdef fslg
#include <lcalc.incl>
;cnst20 : RF field achieved at p13
;cnst21 : on resonance, usually = 0
;cnst22 : positive LG offset
;cnst23 : negative LG offset
;cnst24 : additional LG-offset
#endif /* fslg */
"acqt0=0" ;defines t=0 for baseopt
1 ze

2 d1 do:f2
#ifdef lcp15
#include <p15_prot.incl>
;make sure p15 does not exceed 10 msec
;let supervisor change this pulseprogram if
;more is needed

#endif
#ifdef lacq
;disable protection file for long acquisition change decoupling power !!! or you risk probe
damage
;if you set the label lacq (ZGOPTNS -Dlacq), the protection is disabled

#include <aq_prot.incl>
;allows max. 50 msec acquisition time, supervisor
;may change to max. 1s at less than 5 % duty cycle
;and reduced decoupling field

#endif

```

```

1u fq=cnst21:f2
(p3 pl12 ph1):f2
(p15 pl1 ph2):f1 (p15:sp0 ph10):f2
1u cpds2:f2          ;pl12 is used here with tppm, spinal, pl13 with cwlg, cwlg
go=2 ph31
1m do:f2
wr #0
HaltAcqu, 1m
exit

```

```

ph0= 0
ph1= 1 3
ph2= 0 0 2 2 1 1 3 3
ph10= 0
ph31= 0 2 2 0 1 3 3 1

```

```

;sid: $

```

10.7.7 Modified ¹³C Saturation Recovery Experiment to select Direct/Indirect Polarization Transfer Pathways (satrec_spindif_gen_torsten)

```

;satrec_spindiffusion_Torsten
;acquisition on X with hp proton decoupling
;d1: recycle delay, make sure it is long enough for short vd delays
;d6 : Built Up time during which Pi pulses on 1H are performed (calculated) ca 0.5s
;d7: Built Up time of X-Magnetization
;cnst31 : =MAS spin rate (or =1e6 for static)
;l5: pi pulses during built up with spacing of d6
;d10 : delay between Pi pulses (50 ms or 0.5 s)
;"p30=p31-0.4u"
"d6=(d10/((1s)/cnst31))*((1s)/cnst31)-p4"
"d7=((d10+p4)*15)"

1 ze          ;set RCU to replace mode
2 d1 do:f2    ;recycle delay
3 (p6 pl6 ph6^):f1
  d4
lo to 3 times l4
4 (p4 pl4 ph4^):f2
  d6
lo to 4 times l5
  (p1 pl1 ph1):f1          ;transmitter pulse on F1 with power level pl1
  1u pl12:f2
  1u cpds2:f2          ;use cpdprg2 cw or tppm at power pl12
  go=2 ph31          ;make sure the adc is finished, turn decoupling off
  1m do:f2
; d20
  10m mc #0 to 2 F1QF(ivd)
; wr #0          ;save data in current data set
exit
ph0= 0          ;constant phase for acquisition
ph1= 0 1 2 3    ;simple pulse phase list
ph4= 0 2
ph6= 0 1
ph31=0 1 2 3    ;signal routing corresponds to pulse phase list

```

11 List of Symbols, Abbreviations and Units

11.1 List of Symbols and Abbreviations

μ	Magnetic Momentum
μW_{off}	Spectra Measured without Microwave Irradiation
μW_{on}	Spectra Measured with Microwave Irradiation
APTES	3-Aminopropyl triethoxysilane
AMUPol	[15-{{(7-oxyl-3,11-dioxa-7-azadispiro[5.1.5.3]hexadec-15-yl)carbamoyl}}[2-(2,5,8,11-tetraoxatridecan-13-ylamino)]-[3,11-dioxa-7-azadispiro(5.1.5.3)hexadec-7-yl]oxidanyl developed by Aix-Marseille-University
BET	Brunauer-Emmett-Teller
BJH	Barrett-Joyner-Halenda method
B_0	External Magnetic Field
B_1	Oscillating Magnetic Field
B_{loc}	Local magnetic field
bTbK	bis-TEMPO-bis-ketal
CE	Cross Effect
CT	Central Transition
C_Q	Quadrupolar Coupling Constant
CP	Cross Polarization
CSA	Chemical Shift Anisotropy
CW	Continuous Wave
γ	Gyromagnetic Ratio
DFT	Density Functional Theory
DNP	Dynamic Nuclear Polarization
DSC	Differential Scanning Calorimetry
DQ	Double Quantum
ΔE	Energy Difference
EG	Ethylene Glycol
EG- d_4	Partially Deuterated EG
δ	Chemical Shift Tensor
δ_{iso}	Isotropic Chemical shift
ϵ	Enhancement
E	Energy

<i>e</i>	Electron
e.g.	Exempli gratia: Latin for “for example”
EFG	Electric Field Gradient
Endo	Endothermic Peak
EPR	Electron Paramagnetic Resonance
Exo	Exothermic Peak
Eq.	Equation
equiv.	Amount of a substance that reacts with (or is equivalent to) an arbitrary amount (typically one mole) of another substance in a given chemical reaction.
FID	Free Induction Decay
FT	Fourier Transformation
H	Hamiltonian
<i>h</i>	Plank Constant: $h = 6,6256 \cdot 10^{-34}$ JS; ($\hbar = h/2\pi$)
I	Spin Quantum Number
k_B	Boltzmann Constant: $k_B = 1,380648 \cdot 10^{-23}$ JK ⁻¹
LSA	Line Shape Analysis
m	Magnetic Quantum Number
M	Magnetization
MAS	Magic Angle Spinning
MCM	Mobil Composite of Matter
η_Q	Asymmetry parameter
NMR	Nuclear Magnetic Resonance
NS	Number of Scans
OE	Overhauser Effect
PAS	Principal Axis System
PHIP	Para-Hydrogen-Induced Polarization
ppm	Parts per Million
PTFE	Polytetrafluoroethylene
Q	Nuclear Quadrupole Moment
RF	Radio Frequency
RT	Room Temperature
SABRE	Signal Amplification By Reversible Exchange
SE	Solid Effect
SBA-15	Santa Barbara Amorphous Material 15

SBA-15+APTES	Santa Barbara Amorphous Material 15 modified with APTEs
SLR	Spin Lattice relaxometry
S/N	Signal-to-Noise Ratio
SSB	Spinning Sidebands
STE	Simulated-echo
ssNMR	Solid State Nuclear Magnetic Resonance
R_D	Thermal Resistance
σ	Shielding Factor
σ_{iso}	Shielding
t	Time
T	Temperature
TEOS	Tetraethoxysilane
T_c	Crystallization Temperature
T_g	Glass Transition Temperature
T_1	Longitudinal Relaxation
T_2	Transversal Relaxation
TCE	1,1,2,2-Tetrachloroethane
TEKPol	TCE soluble biradical developed by Aix-Marseille-University
TEMPO	2,2,6,6-tetramethylpiperidine-1-oxyl
TM	Thermal Mixing
TOTAPOL	1-(TEMPO-4-oxy)-3-(TEMPO-4-amino)-propan-2-ol
ω_0	Larmor Frequency
ω_e	Electron Larmor Frequency
ZQ	Zero Quantum

11.2 List of Units

a.u.	Arbitrary Units
(v/v)	Volume per Volume
°C	Degree Celsius
μl	Microliter
Å	Angstrom
cm	Centimeter
g	Gram
h	Hour

K	Kelvin
kHz	Kilo Hertz
l	Liter
M	Molarity, mol/l
m	Meter
mg	Milligram
min	Minute
ml	Milliliter
mM	Milimolar
mm	Millimeter
mol	Mole ($6.022 \cdot 10^{23}$ particles in one mol of a substance)
nm	Nanometer
ps	Picosecond
s	Second
V	Volt

12 Bibliography

- [1] R. A. Soni, M. A. Rizwan, S. Singh, *Nanotechnol. Environ. Eng.* **2022**, 7, 661.
- [2] V. C. Thipe, A. R. Karikachery, P. Çakılıkaya, U. Farooq, H. H. Genedy, N. Kaeokhamloed, D.-H. Phan, R. Rezwan, G. Tezcan, E. Roger, K. V. Katti, *J. Drug Deliv. Sci. Technol.* **2022**, 70, 103256.
- [3] J. A. S. Costa, C. M. Paranhos, *Mitigation of silica-rich wastes: An alternative to the synthesis eco-friendly silica-based mesoporous materials* **2020**.
- [4] M. Moritz, M. Geszke-Moritz, *Materials science & engineering. C, Materials for biological applications* **2015**, 49, 114.
- [5] U. Ciesla, F. Schüth, *Microporous Mesoporous Mater.* **1999**, 27, 131.
- [6] L. Calvillo, V. Celorrio, R. Moliner, P. L. Cabot, I. Esparbé, M. J. Lázaro, *Microporous Mesoporous Mater.* **2008**, 116, 292.
- [7] T. Amitay-Rosen, S. Vega, *Phys. Chem. Chem. Phys.* **2010**, 12, 6763.
- [8] L. Wang, W. Ding, Y. Sun, *Materials Research Bulletin* **2016**, 83, 230.
- [9] Y. Li, J. Shi, *Adv. Mater.* **2014**, 26, 3176.
- [10] H. Weiss, H.-W. Cheng, J. Mars, H. Li, C. Merola, F. U. Renner, V. Honkimäki, M. Valtiner, M. Mezger, *Langmuir* **2019**, 35, 16679.
- [11] C. Alba-Simionesco, G. Dosseh, E. Dumont, B. Frick, B. Geil, D. Morineau, V. Teboul, Y. Xia, *Eur. Phys. J. E* **2003**, 12, 19.
- [12] M. Vogel, *Eur. Phys. J. Spec. Top.* **2010**, 189, 47.
- [13] V. Mouarrawis, R. Plessius, J. I. van der Vlugt, J. N. H. Reek, *Front. Chem.* **2018**, 6, 623.
- [14] an Zou, S. C. Maroo, *Phys. Fluids* **2021**, 33, 42007.
- [15] M. Brodrecht, B. Kumari, A. S. S. L. Thankamony, H. Breitzke, T. Gutmann, G. Buntkowsky, *Chemistry (Weinheim an der Bergstrasse, Germany)* **2019**, 25, 5214.
- [16] S. Rodríguez-de-la-Peña, S. Gómez-Salazar, J. A. Gutiérrez-Ortega, J. Badillo-Camacho, A. A. Peregrina-Lucano, I. G. Shenderovich, R. Manríquez-González, *Ind. Eng. Chem. Res.* **2022**, 61, 4348.
- [17] J. A. Gutiérrez-Ortega, S. Gómez-Salazar, I. G. Shenderovich, R. Manríquez-González, *Materials Chemistry and Physics* **2020**, 239, 122037.
- [18] I. J. Bruce, T. Sen, *Langmuir* **2005**, 21, 7029.
- [19] I. A. Rahman, M. Jafarzadeh, C. S. Sipaut, *Ceram. Int.* **2009**, 35, 1883.
- [20] J. O. Otalvaro, M. Avena, M. Brigante, *J. Environ. Chem. Eng.* **2019**, 7, 103325.
- [21] H. Yue, Y. Zhao, X. Ma, J. Gong, *Chem. Soc. Rev.* **2012**, 41, 4218.
- [22] G. Buntkowsky, S. Döller, N. Haro-Mares, T. Gutmann, M. Hoffmann, *Z Phys Chem (N F)* **2022**, 236, 939.
- [23] A. Czaderna-Lekka, M. Kozanecki, M. Matusiak, S. Kadlubowski, *Polymer* **2021**, 212, 123247.

- [24] Y.-Q. Jiang, J. Li, Z.-W. Feng, G.-Q. Xu, X. Shi, Q.-J. Ding, W. Li, C.-H. Ma, B. Yu, *Adv. Synth. Catal.* **2020**, *362*, 2609.
- [25] Pooria Gill **2010**, *21*, 167.
- [26] S. D. Clas, C. R. Dalton, B. C. Hancock, *Pharm. sci. technol. today* **1999**, *2*, 311.
- [27] M. Ahmadi Khoshooei, F. Fazlollahi, Y. Maham, *J Therm Anal Calorim* **2019**, *138*, 3455.
- [28] Q. Zheng, Y. Zhang, M. Montazerian, O. Gulbiten, J. C. Mauro, E. D. Zanotto, Y. Yue, *Chem. Rev.* **2019**, *119*, 7848.
- [29] H. Saitô, *83*, 1.
- [30] S. C. Döller, M. Brodrecht, N. B. Haro Mares, H. Breitzke, T. Gutmann, M. Hoffmann, G. Buntkowsky, *J. Phys. Chem. C* **2021**, *125*, 25155.
- [31] J. Hassan, *Phys. B: Condens. Matter* **2012**, *407*, 179.
- [32] A. Krushelnitsky, D. Reichert, K. Saalwächter, *Acc. Chem. Res.* **2013**, *46*, 2028.
- [33] J. Eills, D. Budker, S. Cavagnero, E. Y. Chekmenev, S. J. Elliott, S. Jannin, A. Lesage, J. Matysik, T. Meersmann, T. Prisner, J. A. Reimer, H. Yang, I. V. Koptuyug, *Chem. Rev.* **2023**, *123*, 1417.
- [34] B. Plainchont, P. Berruyer, J.-N. Dumez, S. Jannin, P. Giraudeau, *Analytical chemistry* **2018**, *90*, 3639.
- [35] I. B. Moroz, M. Leskes, *Annu. Rev. Mater. Res.* **2022**, *52*, 25.
- [36] A. S. Lilly Thankamony, J. J. Wittmann, M. Kaushik, B. Corzilius, *Prog Nucl Magn Reson Spectrosc* **2017**, *102-103*, 120.
- [37] S. K. Jain, C.-J. Yu, C. B. Wilson, T. Tabassum, D. E. Freedman, S. Han, *Chem* **2021**, *7*, 421.
- [38] M. Kaushik, T. Bahrenberg, T. V. Can, M. A. Caporini, R. Silvers, J. Heiliger, A. A. Smith, H. Schwalbe, R. G. Griffin, B. Corzilius, *Physical chemistry chemical physics PCCP* **2016**, *18*, 27205.
- [39] Y. Rao, C. T. Palumbo, A. Venkatesh, M. Keener, G. Stevanato, A.-S. Chauvin, G. Menzildjian, S. Kuzin, M. Yulikov, G. Jeschke, A. Lesage, M. Mazzanti, L. Emsley, *The journal of physical chemistry. C, Nanomaterials and interfaces* **2022**, *126*, 11310.
- [40] Q. Z. Ni, E. Daviso, T. V. Can, E. Markhasin, S. K. Jawla, T. M. Swager, R. J. Temkin, J. Herzfeld, R. G. Griffin, *Accounts of chemical research* **2013**, *46*, 1933.
- [41] A. Zagdoun, G. Casano, O. Ouari, G. Lapadula, A. J. Rossini, M. Lelli, M. Baffert, D. Gajan, L. Veyre, W. E. Maas, M. Rosay, R. T. Weber, C. Thieuleux, C. Coperet, A. Lesage, P. Tordo, L. Emsley, *Journal of the American Chemical Society* **2012**, *134*, 2284.
- [42] D. J. Kubicki, G. Casano, M. Schwarzwälder, S. Abel, C. Sauvée, K. Ganesan, M. Yulikov, A. J. Rossini, G. Jeschke, C. Copéret, A. Lesage, P. Tordo, O. Ouari, L. Emsley, *Chem. Sci.* **2016**, *7*, 550.
- [43] Y. Matsuki, T. Maly, O. Ouari, H. Karoui, F. Le Moigne, E. Rizzato, S. Lyubenova, J. Herzfeld, T. Prisner, P. Tordo, R. G. Griffin, *Angewandte Chemie (International ed. in English)* **2009**, *48*, 4996.
- [44] T. Maly, G. T. Debelouchina, V. S. Bajaj, K.-N. Hu, C.-G. Joo, M. L. Mak-Jurkauskas, J. R. Sirigiri, P. C. A. van der Wel, J. Herzfeld, R. J. Temkin, R. G. Griffin, *J. Chem. Phys.* **2008**, *128*, 52211.

-
- [45] M. L. Mak-Jurkauskas, R. G. Griffin.
- [46] A. H. Linden, S. Lange, W. T. Franks, U. Akbey, E. Specker, B.-J. van Rossum, H. Oschkinat, *J. Am. Chem. Soc.* **2011**, *133*, 19266.
- [47] R. Yao, D. Beriashvili, W. Zhang, S. Li, A. Safeer, A. Gurinov, A. Rockenbauer, Y. Yang, Y. Song, M. Baldus, Y. Liu, *Chem. Sci.* **2022**, *13*, 14157.
- [48] M.-A. Geiger, A. P. Jagtap, M. Kaushik, H. Sun, D. Stöppler, S. T. Sigurdsson, B. Corzilius, H. Oschkinat, *Chemistry (Weinheim an der Bergstrasse, Germany)* **2018**, *24*, 13485.
- [49] A. P. Jagtap, M.-A. Geiger, D. Stöppler, M. Orwick-Rydmark, H. Oschkinat, S. T. Sigurdsson, *ChemComm.* **2016**, *52*, 7020.
- [50] A. Lund, G. Casano, G. Menzildjian, M. Kaushik, G. Stevanato, M. Yulikov, R. Jabbour, D. Wisser, M. Renom-Carrasco, C. Thieuleux, F. Bernada, H. Karoui, D. Siri, M. Rosay, I. V. Sergeev, D. Gajan, M. Lelli, L. Emsley, O. Ouari, A. Lesage, *Chem. Sci.* **2020**, *11*, 2810.
- [51] K. R. Thurber, T.-N. Le, V. Changcoco, D. J. R. Brook, *J. Magn. Reson.* **2018**, *289*, 122.
- [52] C. Sauvée, M. Rosay, G. Casano, F. Aussenac, R. T. Weber, O. Ouari, P. Tordo, *Angew. Chem. Int. Ed. Engl.* **2013**, *52*, 10858.
- [53] R. Harrabi, T. Halbritter, F. Aussenac, O. Dakhlaoui, J. van Tol, K. K. Damodaran, D. Lee, S. Paul, S. Hediger, F. Mentink-Vigier, S. T. Sigurdsson, G. de Paëpe, *Angew. Chem. Int. Ed. Engl.* **2022**, *61*, e202114103.
- [54] W.-C. Liao, T.-C. Ong, D. Gajan, F. Bernada, C. Sauvée, M. Yulikov, M. Pucino, R. Schowner, M. Schwarzwälder, M. R. Buchmeiser, G. Jeschke, P. Tordo, O. Ouari, A. Lesage, L. Emsley, C. Copéret, *Chem. Sci.* **2017**, *8*, 416.
- [55] K.-N. Hu, *Solid State Nucl Magn Reson* **2011**, *40*, 31.
- [56] A. J. Rossini, A. Zagdoun, M. Lelli, A. Lesage, C. Copéret, L. Emsley, *Acc. Chem. Res.* **2013**, *46*, 1942.
- [57] T. D. Bennett, F.-X. Coudert, S. L. James, A. I. Cooper, *Nat. Mater* **2021**, *20*, 1179.
- [58] B.-L. Su, C. Sanchez, X.-Y. Yang **2011**.
- [59] S. Patra, S. Suresh.
- [60] P. Makowski, X. Deschanel, A. Grandjean, D. Meyer, G. Toquer, F. Goettmann, *New J. Chem.* **2012**, *36*, 531.
- [61] Kevin Lukas **2009**, *14*, 807.
- [62] K. S. W. Sing, *Pure Appl. Chem.* **1985**, *57*, 603.
- [63] Zhao, Feng, Huo, Melosh, Fredrickson, Chmelka, Stucky, *Science* **1998**, *279*, 548.
- [64] F. Schüth, W. Schmidt, *Adv. Mater.* **2002**, *14*, 629.
- [65] S. Savic, K. Vojisavljevic, M. Počuča-Nešić, K. Zivojevic, M. Mladenovic, N. Knezevic, *Metall Mater Eng* **2018**, *24*.
- [66] T. Yanagisawa, T. Shimizu, K. Kuroda, C. Kato, *Bull. Chem. Soc. Jpn.* **1990**, *63*, 988.

- [67] J. S. Beck, J. C. Vartuli, W. J. Roth, M. E. Leonowicz, C. T. Kresge, K. D. Schmitt, C. T. W. Chu, D. H. Olson, E. W. Sheppard, S. B. McCullen, J. B. Higgins, J. L. Schlenker, *J. Am. Chem. Soc.* **1992**, *114*, 10834.
- [68] K. Nishiyabu.
- [69] L. Y. Jaramillo, W. Henao, M. Romero-Sáez, *J. Porous Mater.* **2020**, *27*, 1669.
- [70] A. Vinu, T. Mori, K. Ariga, *Sci Technol Adv Mater* **2006**, *7*, 753.
- [71] Z. AlOthman, *Materials* **2012**, *5*, 2874.
- [72] Y. Liu, J. Liao, L. Chang, W. Bao, *Fuel* **2022**, *311*, 122537.
- [73] M. Brodrecht, H. Breitzke, T. Gutmann, G. Buntkowsky, *Chemistry (Weinheim an der Bergstrasse, Germany)* **2018**, *24*, 17814.
- [74] A.-M. Putz, L. Almásy, A. Len, C. Ianăși, *Fuller. Nanotub. Carbon Nanostructures* **2019**, *27*, 323.
- [75] M. Brodrecht, B. Kumari, H. Breitzke, T. Gutmann, G. Buntkowsky, *Z Phys Chem (N F)* **2018**, *232*, 1127.
- [76] W. H. Thompson, *J. Chem. Phys.* **2018**, *149*, 170901.
- [77] E. Gedat, A. Schreiber, J. Albrecht, T. Emmler, I. Shenderovich, G. H. Findenegg, H.-H. Limbach, G. Buntkowsky, *J. Phys. Chem. B* **2002**, *106*, 1977.
- [78] G. Wang, A. N. Otuonye, E. A. Blair, K. Denton, Z. Tao, T. Asefa, *J. Solid State Chem.* **2009**, *182*, 1649.
- [79] A.S Maria Chong **2003**, *107*, 12650.
- [80] D. Brühwiler, *Nanoscale* **2010**, *2*, 887.
- [81] X. Zeng, G. Xu, Y. Gao, Y. An, *The journal of physical chemistry. B* **2011**, *115*, 450.
- [82] A. Kołodziejczak-Radzimska, J. Zdarta, T. Jesionowski, *Biotechnology progress* **2018**, *34*, 767.
- [83] M. C. Bourkaib, P. Gaudin, F. Vibert, Y. Guiavarc'h, S. Delaunay, X. Framboisier, C. Humeau, I. Chevalot, J.-L. Blin, *Microporous Mesoporous Mater.* **2021**, *323*, 111226.
- [84] Y. Wang, C. J. Hansen, C.-C. Wu, E. J. Robinette, A. M. Peterson, *RSC Adv.* **2021**, *11*, 31142.
- [85] D. Kowalczyk, S. Slomkowski, M. M. Chehimi, M. Delamar, *International Journal of Adhesion and Adhesives* **1996**, *16*, 227.
- [86] Y. Pu, K. Xuan, F. Wang, A. Li, N. Zhao, F. Xiao, *RSC advances* **2018**, *8*, 27216.
- [87] S. Jiang, D. Yu, X. Ji, L. An, B. Jiang, *Polymer* **2000**, *41*, 2041.
- [88] J.-P. Korb, S. Xu, J. Jonas, *J. Chem. Phys.* **1993**, *98*, 2411.
- [89] N. Koone, Y. Shao, T. W. Zerda, *J. Phys. Chem.* **1995**, *99*, 16976.
- [90] J. Zhang, G. Liu, J. Jonas, *J. Phys. Chem.* **1992**, *96*, 3478.
- [91] G. Buntkowsky, M. Vogel, *Molecules* **2020**, *25*.
- [92] J. J. Kasianowicz, M. S. Z. Kellermayer, D. W. Deamer, *Structure and dynamics of confined polymers: Proceedings of the NATO Advanced Research Workshop on biological, biophysical and theoretical aspects of polymer structure and transport, held in Bikal, Hungary, June 20-25, 1999 / edited by John J. Kasianowicz, Miklos S.Z. Kellermayer, David W. Deamer, Kluwer Academic, Dordrecht, London* **2002**.
- [93] M. P. Singh, R. K. Singh, S. Chandra, *Prog. Mater. Sci.* **2014**, *64*, 73.

- [94] M. Werner, N. Rothermel, H. Breitzke, T. Gutmann, G. Buntkowsky, *Isr. J. Chem.* **2014**, *54*, 60.
- [95] G. Buntkowsky, H. Breitzke, A. Adamczyk, F. Roelofs, T. Emmler, E. Gedat, B. Grünberg, Y. Xu, H.-H. Limbach, I. Shenderovich, A. Vyalikh, G. Findenegg, *Phys. Chem. Chem. Phys.* **2007**, *9*, 4843.
- [96] H. Qian, G. Song, L. Lv, Y. Cheng, L. Zhang, J. Chen, *J. Clean. Prod.* **2022**, *355*, 131764.
- [97] H. C. Fuller, *Ind. Eng. Chem. Res.* **1924**, *16*, 624.
- [98] Y.-Q. Zou, N. von Wolff, A. Anaby, Y. Xie, D. Milstein, *Nat. Catal* **2019**, *2*, 415.
- [99] C. Gao, G.-Y. Zhou, Y. Xu, T.-C. Hua, *Thermochim. Acta* **2005**, *435*, 38.
- [100] GlobalData **2021**, <https://www.statista.com/statistics/1067418/global-ethylene-glycol-production-capacity/>.
- [101] *Handbook of chemistry and physics: A ready reference book of chemical and physical data*, CRC Press, Boca Ratón, Florida **1979**.
- [102] D. Christen, L. H. Coudert, J. A. Larsson, D. Cremer, *J. Mol. Spectrosc.* **2001**, *205*, 185.
- [103] A. D. Fortes, E. Suard, *J. Chem. Phys.* **2011**, *135*, 234501.
- [104] G. Hohne, W. F. Hemminger, H. J. Flammersheim, *Differential scanning calorimetry*, Springer Berlin **2003**.
- [105] K Nijmeijer, *Differential Scanning Calorimetry*, https://assets.tue.nl/fileadmin/content/faculteiten/st/Onderzoek/Onderzoeksgroepen/Membrane_Materials_Processes/Facilities/DSC__PerkinElmer_PYRIS_Diamond_.pdf.
- [106] *Differential Scanning Calorimetry* **2019**, <https://pslc.ws/macrog/dsc.htm>.
- [107] G. Biroli, J. P. Garrahan, *J. Chem. Phys.* **2013**, *138*, 12A301.
- [108] C. Austen Angell **1996**, *1*, 578.
- [109] J. Keeler, *Understanding NMR spectroscopy*, Wiley, Oxford **2010**.
- [110] M. H. Levitt, *Spin dynamics: Basics of nuclear magnetic resonance / Malcolm H. Levitt*, Wiley; Chichester John Wiley [distributor], Hoboken, N.J. **2008**.
- [111] C. P. Slichter, *Principles of magnetic resonance*, Springer-Verlag, Berlin **1990 (1992 [printing])**.
- [112] C. A. Fyfe, *Solid state NMR for chemists*, C.F.C. Press, Guelph, Ont. **1983**.
- [113] M. J. Duer, *Solid-state NMR spectroscopy: Principles and applications / edited by Melinda J. Duer*, Blackwell Science, Oxford **2002**.
- [114] Xiaorong yYang, *Solid-State NMR Studies of the Guest Molecules in Urea Inclusion Compounds* **2007**.
- [115] K. Schmidt-Rohr, H. W. Spiess, *Multidimensional solid-state NMR and polymers*, Academic Press, London **1994**.
- [116] R. R. Ernst, G. Bodenhausen, A. Wokaun, *Principles of nuclear magnetic resonance in one and two dimensions*, Clarendon, Oxford **1987**.
- [117] M. Mehring, *Principles of high resolution NMR in solids*, Springer, Berlin, Heidelberg, New York **1983**.
- [118] Christopher Andrew O'Keefe, *Multinuclear Solid-State NMR Investigation of Structure, Dynamics, and Formation of Porous Materials*, Windsor, Ontario Canada **2018**.

- [119] I. P. GEROTHANASSIS, A. TROGANIS, V. EXARCHOU, K. BARBAROSSOU, *Chem. Educ. Res. Pract.* **2002**, *3*, 229.
- [120] P. L. Rinaldi, M. Monwar.
- [121] H. Friebolin, C. M. Thiele, *Ein- und zweidimensionale NMR-Spektroskopie: Eine Einführung / Horst Friebolin*, WILEY-VCH Verlag GmbH & Co. KGaA, Weinheim, Germany **2013**.
- [122] D. D. Laws, H.-M. L. Bitter, A. Jerschow, *Angew. Chem. Int. Ed. Engl.* **2002**, *41*, 3096.
- [123] M. Mehring, *Principles of High Resolution NMR in Solids*, Springer Berlin Heidelberg, Berlin, Heidelberg **1983**.
- [124] T. Polenova, R. Gupta, A. Goldbourn, *Analytical chemistry* **2015**, *87*, 5458.
- [125] T. Bräuniger, M. Jansen, *Z. anorg. allg. Chem.* **2013**, *639*, 857.
- [126] A. E. McDermott, T. Polenova, *Solid-state NMR studies of biopolymers*, Wiley, Oxford **2010**.
- [127] N. Ramsey, *Molecular beams*, Clarendon, Oxford **1956**.
- [128] *Encyclopedia of analytical chemistry*, John Wiley & Sons, Hoboken **2006**-.
- [129] M. Smith, *Prog Nucl Magn Reson Spectrosc* **1999**, *34*, 159.
- [130] S. E. Ashbrook, *Phys. Chem. Chem. Phys.* **2009**, *11*, 6892.
- [131] J. Dolinšek, M. Vilfan, S. Žumer, *Novel NMR and EPR techniques*, Springer, Berlin, London **2006**.
- [132] D. Burstein, *Concepts Magn. Reson.* **1996**, *8*, 269.
- [133] S. Schneider, C. Säckel, M. Brodrecht, H. Breitzke, G. Buntkowsky, M. Vogel, *The Journal of chemical physics* **2020**, *153*, 244501.
- [134] E. Steinrücken, T. Wissel, M. Brodrecht, H. Breitzke, J. Regentin, G. Buntkowsky, M. Vogel, *The Journal of chemical physics* **2021**, *154*, 114702.
- [135] M. Becher, A. Lichtinger, R. Minikejew, M. Vogel, E. A. Rössler, *International journal of molecular sciences* **2022**, *23*.
- [136] D. A. Barskiy, A. M. Coffey, P. Nikolaou, D. M. Mikhaylov, B. M. Goodson, R. T. Branca, G. J. Lu, M. G. Shapiro, V.-V. Telkki, V. V. Zhivonitko, I. V. Koptuyug, O. G. Salnikov, K. V. Kovtunov, V. I. Bukhtiyarov, M. S. Rosen, M. J. Barlow, S. Safavi, I. P. Hall, L. Schröder, E. Y. Chekmenev, *Chemistry (Weinheim an der Bergstrasse, Germany)* **2017**, *23*, 725.
- [137] R. G. Griffin, T. F. Prisner, *Phys. Chem. Chem. Phys.* **2010**, *12*, 5737.
- [138] M. Rosay, M. Blank, F. Engelke, *J. Magn. Reson.* **2016**, *264*, 88.
- [139] G. Menzildjian, J. Schlagnitweit, G. Casano, O. Ouari, D. Gajan, A. Lesage, *Chem. Sci.* **2023**, *14*, 6120.
- [140] M. M. Hoffmann, S. Bothe, T. Gutmann, F.-F. Hartmann, M. Reggelin, G. Buntkowsky, *J. Phys. Chem. C* **2017**, *121*, 2418.
- [141] F. Mentink-Vigier, I. Marin-Montesinos, A. P. Jagtap, T. Halbritter, J. van Tol, S. Hediger, D. Lee, S. T. Sigurdsson, G. de Paëpe, *J. Am. Chem. Soc.* **2018**, *140*, 11013.

- [142] A. Zagdoun, G. Casano, O. Ouari, M. Schwarzwälder, A. J. Rossini, F. Aussenac, M. Yulikov, G. Jeschke, C. Copéret, A. Lesage, P. Tordo, L. Emsley, *J. Am. Chem. Soc.* **2013**, *135*, 12790.
- [143] W. Zhai, A. Lucini Paioni, X. Cai, S. Narasimhan, J. Medeiros-Silva, W. Zhang, A. Rockenbauer, M. Weingarth, Y. Song, M. Baldus, Y. Liu, *J. Phys. Chem. B* **2020**, *124*, 9047.
- [144] N. B. Asanbaeva, S. A. Dobrynin, D. A. Morozov, N. Haro-Mares, T. Gutmann, G. Buntkowsky, E. G. Bagryanskaya, *Molecules* **2023**, *28*.
- [145] A. Radaelli, H. A. I. Yoshihara, H. Nonaka, S. Sando, J. H. Ardenkjaer-Larsen, R. Gruetter, A. Capozzi, *J. Phys. Chem. Lett.* **2020**, *11*, 6873.
- [146] S. R. Hartmann, E. L. Hahn, *Phys. Rev.* **1962**, *128*, 2042.
- [147] E. Stejskal, J. Schaefer, J. Waugh, *J. Magn. Reson.* **1977**, *28*, 105.
- [148] Sarah Bothe, *Studies on nonionic surfactants and investigation of novel polarization transfer mechanisms for Dynamic Nuclear Polarization NMR magic angle spinning experiments* **2019**.
- [149] K. H. HAUSSER, D. STEHLIK, *3*, 79.
- [150] Y. Hovav, A. Feintuch, S. Vega, *J. Magn. Reson.* **2012**, *214*, 29.
- [151] Y. Hovav, A. Feintuch, S. Vega, *Phys. Chem. Chem. Phys.* **2013**, *15*, 188.
- [152] B. Corzilius.
- [153] X. Wang, K. S. K. Lin, J. C. C. Chan, S. Cheng, *J. Phys. Chem. B* **2005**, *109*, 1763.
- [154] R. K. Zeidan, S.-J. Hwang, M. E. Davis, *Angew. Chem. Int. Ed. Engl.* **2006**, *45*, 6332.
- [155] M. Thommes, K. Kaneko, A. V. Neimark, J. P. Olivier, F. Rodriguez-Reinoso, J. Rouquerol, K. S. Sing, *Pure Appl. Chem.* **2015**, *87*, 1051.
- [156] M. Weigler, E. Winter, B. Kresse, M. Brodrecht, G. Buntkowsky, M. Vogel, *Phys. Chem. Chem. Phys.* **2020**, *22*, 13989.
- [157] K. R. Thurber, R. Tycko, *Measurement of sample temperatures under magic-angle spinning from the chemical shift and spin-lattice relaxation rate of ⁷⁹Br in KBr powder*, *J. Magn. Reson.*, *196*, 84.
- [158] D. Massiot, F. Fayon, M. Capron, I. King, S. Le Calvé, B. Alonso, J.-O. Durand, B. Bujoli, Z. Gan, G. Hoatson, *Magn. Reson. Chem.* **2002**, *40*, 70.
- [159] A. Vyalikh, T. Emmler, I. Shenderovich, Y. Zeng, G. H. Findenegg, G. Buntkowsky, *Phys. Chem. Chem. Phys.* **2007**, *9*, 2249.
- [160] N. B. Asanbaeva, L. Y. Gurskaya, Y. F. Polienko, T. V. Rybalova, M. S. Kazantsev, A. A. Dmitriev, N. P. Gritsan, N. Haro-Mares, T. Gutmann, G. Buntkowsky, E. V. Tretyakov, E. G. Bagryanskaya, *Molecules* **2022**, *27*.
- [161] D.G Cory & W.M Ritchey **1988**, *80*, 128.
- [162] G. Comellas, J. J. Lopez, A. J. Nieuwkoop, L. R. Lemkau, C. M. Rienstra, *J. Magn. Reson.* **2011**, *209*, 131.
- [163] B. M. Fung, A. K. Khitrin, K. Ermolaev, *J. Magn. Reson.* **2000**, *142*, 97.
- [164] N. B. Haro Mares, M. Brodrecht, T. Wissel, S. C. Döllner, L. Rösler, H. Breitzke, M. M. Hoffmann, T. Gutmann, G. Buntkowsky, *J. Phys. Chem. C* **2023**.

-
- [165] V. Crupi, S. Magazù, D. Majolino, P. Migliardo, M. Bellissent-Funel, *Phys. B: Condens. Matter* **2000**, 276-278, 417.
- [166] R. Narayan, U. Y. Nayak, A. M. Raichur, S. Garg, *Pharmaceutics* **2018**, 10.
- [167] M. Reuhl, M. Weigler, M. Brodrecht, G. Buntkowsky, M. Vogel, *J. Phys. Chem. C* **2020**, 124, 20998.
- [168] W. Masierak, T. Emmler, E. Gedat, A. Schreiber, G. H. Findenegg, G. Buntkowsky, *J. Phys. Chem. B* **2004**, 108, 18890.
- [169] S. Jayanthi, S. Kababya, A. Schmidt, S. Vega, *J. Phys. Chem. C* **2016**, 120, 2797.
- [170] M. M. Hoffmann, S. Bothe, T. Gutmann, G. Buntkowsky, *J. Phys. Chem. B* **2018**, 122, 4913.
- [171] G. H. Findenegg, S. Jähnert, D. Akcakayiran, A. Schreiber, *ChemPhysChem* **2008**, 9, 2651.
- [172] B. Jansen-Glaw, E. Rössler, M. Taupitz, H. M. Vieth, *J. Chem. Phys.* **1989**, 90, 6858.
- [173] A. L. Doadrio, J. M. Sánchez-Montero, J. C. Doadrio, A. J. Salinas, M. Vallet-Regí, *Microporous Mesoporous Mater.* **2014**, 195, 43.
- [174] E. Rössler, M. Taupitz, K. Börner, M. Schulz, H.-M. Vieth, *J. Chem. Phys.* **1990**, 92, 5847.
- [175] A. Vyalikh, T. Emmler, E. Gedat, I. Shenderovich, G. H. Findenegg, H.-H. Limbach, G. Buntkowsky, *Solid State Nucl Magn Reson* **2005**, 28, 117.
- [176] B. Grünberg, A. Grünberg, H.-H. Limbach, G. Buntkowsky, *Appl. Magn. Reson.* **2013**, 44, 189.
- [177] N. de Sousa Amadeu, B. Grünberg, J. Frydel, M. Werner, H.-H. Limbach, H. Breitzke, G. Buntkowsky, *Z Phys Chem (N F)* **2012**, 226, 1169.
- [178] T. Gutmann, P. B. Groszewicz, G. Buntkowsky, 97, 1.
- [179] A. G. M. Rankin, J. Trébosc, F. Pourpoint, J.-P. Amoureux, O. Lafon, *Solid State Nucl Magn Reson* **2019**, 101, 116.
- [180] W.-C. Liao, B. Ghaffari, C. P. Gordon, J. Xu, C. Copéret, *Curr. Opin. Colloid. Interface. Sci.* **2018**, 33, 63.
- [181] F. A. Perras, L.-L. Wang, J. S. Manzano, U. Chaudhary, N. N. Opembe, D. D. Johnson, I. I. Slowing, M. Pruski, *Curr. Opin. Colloid. Interface. Sci.* **2018**, 33, 9.
- [182] L. Zhao, A. C. Pinon, L. Emsley, A. J. Rossini, *Magn. Reson. Chem.* **2018**, 56, 583.
- [183] I. Bagryanskaya, M. Fedin, D. Gorbunov, N. Gritsan, L. Gurskaya, M. Kazantsev, Y. Polienko, D. Stass, E. Tretyakov, *Tetrahedron Lett.* **2017**, 58, 478.
- [184] B. C. Gilbert, D. M. Murphy, V. Chechik, Royal Society of Chemistry **2016**.
- [185] S. Stoll, A. Schweiger, *J. Magn. Reson.* **2006**, 178, 42.
- [186] F. Neese, *WIREs Comput Mol Sci* **2018**, 8.
- [187] G. S. Singh, *Advances in synthesis and chemistry of azetidines*, Academic Press, Amsterdam **2020**.
- [188] D. E. Davies, R. C. Storr, *Azetidines, Azetines and Azetes*.
- [189] E. J. Goethals, E. H. Schacht, Y. E. Bogaert, S. I. Ali, Y. Tezuka, *Polym. J.* **1980**, 12, 571.

-
- [190] S. Bothe, J. Nowag, V. Klimavičius, M. Hoffmann, T. I. Troitskaya, E. V. Amosov, V. M. Tormyshev, I. Kirilyuk, A. Taratayko, A. Kuzhelev, D. Parkhomenko, E. Bagryanskaya, T. Gutmann, G. Buntkowsky, *J. Phys. Chem. C* **2018**, *122*, 11422.
- [191] M. M. Hoffmann, S. Bothe, M. Brodrecht, V. Klimavicius, N. B. Haro-Mares, T. Gutmann, G. Buntkowsky, *J. Phys. Chem. C* **2020**, *124*, 5145.
- [192] H. Park, B. Uluca-Yazgi, S. Heumann, R. Schlögl, J. Granwehr, H. Heise, P. P. M. Schleker, *J. Magn. Reson.* **2020**, *312*, 106688.
- [193] V. Aladin, M. Vogel, R. Binder, I. Burghardt, B. Suess, B. Corzilius, *Angew. Chem. Int. Ed. Engl.* **2019**, *58*, 4863.
- [194] D. Daube, V. Aladin, J. Heiliger, J. J. Wittmann, D. Barthelmes, C. Bengs, H. Schwalbe, B. Corzilius, *J. Am. Chem. Soc.* **2016**, *138*, 16572.
- [195] J. L. White, J. F. Haw, *J. Am. Chem. Soc.* **1990**, *112*, 5896.
- [196] G. Stevanato, G. Casano, D. J. Kubicki, Y. Rao, L. Esteban Hofer, G. Menzildjian, H. Karoui, D. Siri, M. Cordova, M. Yulikov, G. Jeschke, M. Lelli, A. Lesage, O. Ouari, L. Emsley, *J. Am. Chem. Soc.* **2020**, *142*, 16587.
- [197] L. B. Casabianca, A. I. Shames, A. M. Panich, O. Shenderova, L. Frydman, *J. Phys. Chem. C* **2011**, *115*, 19041.
- [198] H. Sato, V. Kathirvelu, A. Fielding, J. P. Blinco, A. S. Micallef, S. E. Bottle, S. S. Eaton, G. R. Eaton, *Mol. Phys.* **2007**, *105*, 2137.
- [199] V. Kathirvelu, C. Smith, C. Parks, M. A. Mannan, Y. Miura, K. Takeshita, S. S. Eaton, G. R. Eaton, *ChemComm.* **2009**.
- [200] S. A. Dobrynin, Y. I. Glazachev, Y. V. Gatilov, E. I. Chernyak, G. E. Salnikov, I. A. Kirilyuk, *J. Org. Chem.* **2018**, *83*, 5392.
- [201] J. T. Paletta, M. Pink, B. Foley, S. Rajca, A. Rajca, *Org. Lett.* **2012**, *14*, 5322.

Erklärungen laut Promotionsordnung

§8 Abs. 1 lit. c PromO

Ich versichere hiermit, dass die elektronische Version meiner Dissertation mit der schriftlichen Version übereinstimmt und für die Durchführung des Promotionsverfahrens vorliegt.

§8 Abs. 1 lit. d PromO

Ich versichere hiermit, dass zu einem vorherigen Zeitpunkt noch keine Promotion versucht wurde und zu keinem früheren Zeitpunkt an einer in- oder ausländischen Hochschule eingereicht wurde.

In diesem Fall sind nähere Angaben über Zeitpunkt, Hochschule, Dissertationsthema und Ergebnis dieses Versuchs mitzuteilen.

§9 Abs. 1 PromO

Ich versichere hiermit, dass die vorliegende Dissertation selbstständig und nur unter Verwendung der angegebenen Quellen verfasst wurde.

§9 Abs. 2 PromO

Die Arbeit hat bisher noch nicht zu Prüfungszwecken gedient.

Darmstadt, 27 Mai 2024

Nadia Berenice Haro Mares